Department of Applied Physics

Designing exotic phases of matter with magnetic van der Waals materials

Guangze Chen

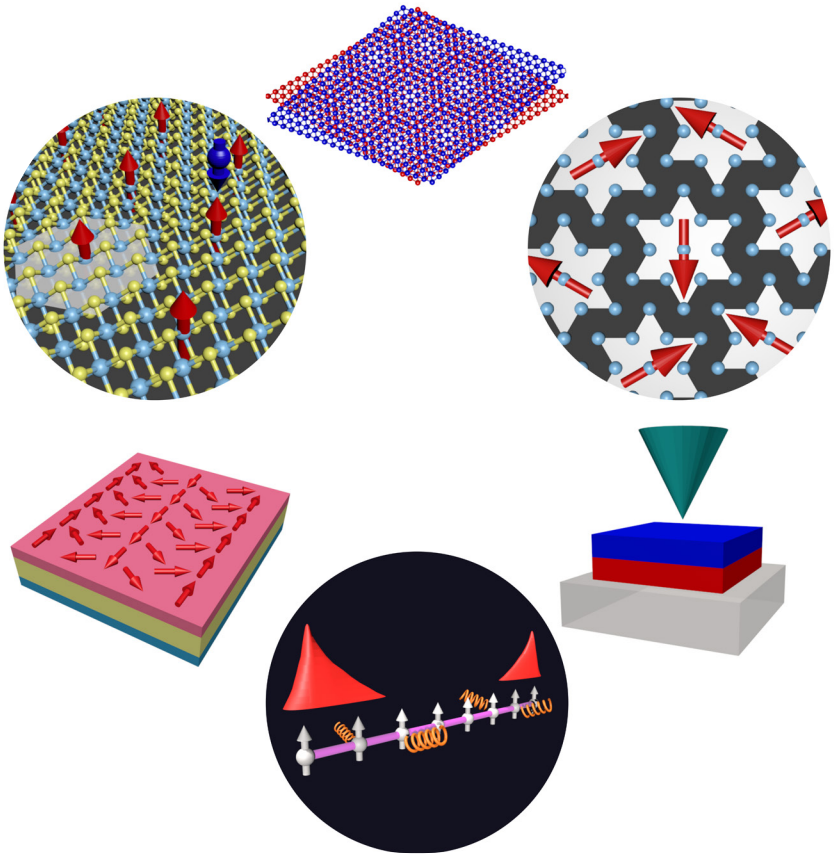

Aalto University

DOCTORAL THESES

Aalto University publication series
DOCTORAL THESES 84/2023

Designing exotic phases of matter with magnetic van der Waals materials

Guangze Chen

A doctoral thesis completed for the degree of Doctor of Science (Technology) to be defended, with the permission of the Aalto University School of Science, at a public examination held at the lecture hall V002 of the Business block on 26 June 2023 at 12:00.

Aalto University
School of Science
Department of Applied Physics
Correlated Quantum Materials (CQM) group

Supervising professors
Prof. Jose L. Lado
Aalto University
Finland

Preliminary examiners
Dr. Mark H. Fischer,
University of Zurich
Switzerland

Dr. Jose J. Baldovi,
ICMol, University of Valencia
Spain

Opponents
Prof. Nuno M. R. Peres
University of Minho
Portugal

Aalto University publication series
DOCTORAL THESES 84/2023

ISBN 978-952-64-1298-6 (printed)
ISBN 978-952-64-1299-3 (pdf)
ISSN 1799-4934 (printed)
ISSN 1799-4942 (pdf)
http://urn.fi/URN:ISBN:978-952-64-1299-3

Unigrafia Oy
Helsinki 2023

Finland

Publication orders (printed book):
guanzge.chen@aalto.fi

Printed matter
4041-0619

Aalto University

Abstract

Aalto University, P.O. Box 11000, FI-00076 Aalto www.aalto.fi

Author
Guangze Chen

Name of the doctoral thesis
Designing exotic phases of matter with magnetic van der Waals materials

Publisher School of Science

Unit Department of Applied Physics

Series Aalto University publication series DOCTORAL THESES 84/2023

Field of research Condensed matter theory

Manuscript submitted 7 March 2023 **Date of the defence** 26 June 2023

Permission for public defence granted (date) 12 May 2023 **Language** English

☐ **Monograph** ☒ **Article thesis** ☐ **Essay thesis**

Abstract

Magnetic van der Waals materials have recently emerged as a realization of quantum magnetism in two dimensions. They host a variety of phases including ferromagnets, anti-ferromagnets, helimagnets, and quantum spin liquids. The 2D nature of these materials makes them versatile platforms for quantum engineering. In this thesis, we explore via theoretical techniques how different quantum engineering methods allow to design and reveal exotic phases of matter in magnetic van der Waals materials. In particular, we will present three schemes. The first scheme focuses on external engineering on a 2D magnet to promote and identify the quantum spin liquid phase. The second scheme focuses on designing helical electronic states and heavy fermions via proximity to 2D magnets. The third scheme focuses on the utilization of the coupling of quantum magnets to the environment to design non-Hermitian many-body topological phases of matter. Our results put forward magnetic van der Waals materials as a versatile platform for engineering exotic phases of matter.

Keywords Magnetic van der Waals materials, quantum spin liquids, helical states, heavy-fermions, non-Hermitian physics

ISBN (printed) 978-952-64-1298-6 **ISBN (pdf)** 978-952-64-1299-3

ISSN (printed) 1799-4934 **ISSN (pdf)** 1799-4942

Location of publisher Helsinki **Location of printing** Helsinki **Year** 2023

Pages 220 **urn** http://urn.fi/URN:ISBN:978-952-64-1299-3

Preface

This thesis consists of results mainly carried out under the supervision of my dear supervisor Prof. Jose Lado at the Correlated Quantum Materials group at the Department of Applied Physics at Aalto University. Jose is a smart and enthusiastic researcher and a patient supervisor. He has provided me with original and innovative ideas together with hand-by-hand assistance in every detailed aspect of research such as programming, writing, physical understanding, philosophy of thinking, and so on. The detailed care from Jose has greatly improved me. I would like to sincerely thank Jose for these extensive helps.

Apart from the guidance from Jose, I benefit a lot from collaborations with other researchers. These include theoretical collaborations with Aline Ramires at Paul Scherrer Institute, Prof. Malte Rösner at Radboud University, Fei Song at Institute for Advanced Study at Tsinghua University, and Maryam Khosravian in my group. In addition, I benefit from experimental collaborations with the Atomic Scale Physics group at the Department of Applied Physics at Aalto University led by Prof. Peter Liljeroth, in particular with my dear friend Viliam Vaňo. I would like to acknowledge their help in my Ph.D. studies, with special thanks to Fei and Viliam.

Apart from that, I would also like to acknowledge Prof. Wei Chen at the Department of Physics at Nanjing University for academic collaborations and career plan instructions. In this line, I would like to acknowledge Prof. Linghao Yan, Prof. Peter Liljeroth, and Prof. Zhong Wang for helping with my career plan, with special thanks to Peter.

I would otherwise like to acknowledge all my colleagues at the Department of Applied Physics, Aalto University, especially the colleagues in Jose's and Peter's group. These include Maryam, Rouven Koch, Pascal Vecsei, Marcel Niedermeier (who helped me with Julia and Itensor programming), Doctor Adolfo (Otero Fumega) (knowledgeable helpful brother

who taught me a lot about magnetic van der Waals materials and making cakes), Faluke Aikebaier, Timo Hyart, Viliam (young and smart brother who helped me both in research and life), Kuhsar Amini, Markus Aapro, Liwei Jing, Abe Kipnis, Linghao (who taught me "C'est la vie"), González Hector the best (warm patient brother who taught me football and climbing and etc.). Remarkably, they are not only nice colleagues at work but also nice friends in life. In particular, Viliam, Kuhsar, and my Espanõl brothers Dr. Adolfo and Hector have provided plenty of help in my daily life and taught me daily life skills. I had plenty of fun with my colleagues in a variety of activities. In this line, I would also like to acknowledge Peter for the pool table and the Helium gas in his lab. I would also like to thank the administrative staff including Bernadette, Suvi, and Sitav, and the IT support staff including Ivan, who made everything simple for us.

To this end, I would like to thank my parents and my girlfriend, Heyi Yang, for their understanding of my decision to do a Ph.D. and their extensive support during my Ph.D. study.

I acknowledge the discussions with Fei Song, Viliam Vaňo, Dr. Adolfo, and Maryam Khosravian during the writing of my thesis.

Espoo, March 6, 2023,

Guangze Chen

Contents

List of Publications

This thesis consists of an overview and of the following publications.

I Guangze Chen, Jose L. Lado. Impurity-induced resonant spinon zero modes in Dirac quantum spin liquids. *Physical Review Research*, 2, 033466, September 2020.

II Guangze Chen, Jose L. Lado. Tunable moire spinons in magnetically encapsulated twisted van der Waals quantum spin liquids. *Physical Review Research*, 3, 033276, September 2021.

III Guangze Chen, Malte Rösner, Jose L. Lado. Controlling magnetic frustration in 1T-TaS_2 via Coulomb engineered long-range interactions. *Journal of Physics: Condensed Matter*, 34, 485805, October 2022.

IV Guangze Chen, Maryam Khosravian, Jose L. Lado, Aline Ramires. Designing spin-textured flat bands in twisted graphene multilayers via helimagnet encapsulation. *2D Materials*, 9, 024002, February 2022.

V Viliam Vaňo, Mohammad Amini, Somesh C. Ganguli, Guangze Chen, Jose L. Lado, Shawulienu Kezilebieke and Peter Liljeroth. Artificial heavy fermions in a van der Waals heterostructure. *Nature*, 599, 582–586, November 2021.

VI Guangze Chen, Fei Song, Jose L. Lado. Topological spin excitations in non-Hermitian spin chains with a generalized kernel polynomial algorithm. *Physical Review Letters*, 130, 100401, March 2023.

Apart from these publications, the author has contributed to the following works during his Ph.D. studies which are not included in the thesis:

- Xi-Rong Chen, Guangze Chen, Yue Zheng, Wei Chen, and D. Y. Xing. Conductance oscillation in surface junctions of Weyl semimetals. *Physical Review B*, 104, 205412, November 2021

- Pramod Kumar, Guangze Chen, and J. L. Lado. Kondo lattice mediated interactions in flat-band systems. *Physical Review Research*, 3, 043113, November 2021

- Viliam Vaňo, Somesh Chandra Ganguli, Mohammad Amini, Linghao Yan, Maryam Khosravian, Guangze Chen, Shawulienu Kezilebieke, Jose L. Lado, Peter Liljeroth. Evidence of nodal f-wave superconductivity in monolayer 1H-TaS_2 with hidden order fluctuations. *arXiv:2112.07316*, December 2021

- Netta Karjalainen, Zina Lippo, Guangze Chen, Rouven Koch, Adolfo O. Fumega, Jose L. Lado. Hamiltonian inference from dynamical excitations in spin quantum dots. *arXiv:2212.07893*, December 2022

In addition, the results shown in Sec.5.2.2 form the basis for one more paper to be submitted in the incoming months.

Author's Contribution

Publication I: "Impurity-induced resonant spinon zero modes in Dirac quantum spin liquids"

G.C. did the theoretical analysis under the supervision of J.L.L. G.C. and J.L.L. wrote the manuscript.

Publication II: "Tunable moire spinons in magnetically encapsulated twisted van der Waals quantum spin liquids"

G.C. did the theoretical analysis under the supervision of J.L.L. G.C. and J.L.L. wrote the manuscript.

Publication III: "Controlling magnetic frustration in 1T-TaS_2 via Coulomb engineered long-range interactions"

G.C. did the theoretical analysis under the supervision of M.R. and J.L.L. G.C., M.R. and J.L.L. wrote the manuscript.

Publication IV: "Designing spin-textured flat bands in twisted graphene multilayers via helimagnet encapsulation"

G.C. did the theoretical analysis with the assistance of M.K., under the supervision of J.L.L. and A.R. G.C., M.K., J.L.L. and A.R. wrote the manuscript.

Publication V: "Artificial heavy fermions in a van der Waals heterostructure"

V.V., J.L.L., S.K. and P.L. conceived the experiment, V.V., M.A., S.C.G. and S.K. carried out the sample growth and the low-temperature STM experiments. V.V. analyzed the STM data. G.C. and J.L.L. developed the theoretical model. V.V., J.L.L. and P.L. wrote the manuscript with input from all co-authors.

Publication VI: "Topological spin excitations in non-Hermitian spin chains with a generalized kernel polynomial algorithm"

G.C. developed the algorithm and performed the theoretical analysis with the idea from J.L.L. and theoretical support from F.S. G.C., F.S. and J.L.L. wrote the manuscript.

1. Introduction

With the rapidly developing quantum technology, we are able to manufacture nano-scale devices for faster processing. A particular highlight of this is the access to two-level quantum systems such as single magnetic atoms and Josephson junctions. This has allowed for the experimental realization of the remarkable idea of quantum computation [1], in which quantum two-level systems are utilized as qubits for fast computation.

Despite the rapid development of quantum computation, challenges remain to be addressed to unleash its potential power. One remarkable experimental challenge is that the inevitable coupling between the qubit and the environment results in the loss of the information stored in the qubit. This has limited the time scale of faithful quantum computation to nanoseconds and prevents the scaling up of quantum computation with more qubits while maintaining fidelity.

Interestingly, topological protection provides a solution to the above problem. Topological protection refers to the protection of the (ground) state against local perturbations (that can break any symmetries) due to the intrinsic topological order encoded in such a state. A topologically protected state exhibits strong stability against perturbations and thus preserves the stored information in such a state for a much longer time. Historically, the theory of intrinsic topological order [2] was inspired by the fractional quantum Hall effect (FQHE) [3], which was later explained by Laughlin with a many-body electronic wavefunction [4]. The key feature of the Laughlin wavefunction is it supports fractional excitations that cannot be excited alone locally, which is essentially related to the intrinsic topological order of this wavefunction. Quantum spin liquid states were then theoretically found to feature the same properties [5, 6]. Two more examples of intrinsic topological order were proposed later by Kitaev, the toric code model [7] and the Kitaev spin liquid [8].

Despite the theoretical development in quantum spin liquids, experimental realization and identification of the quantum spin liquid phases have been challenging. From the realization point of view, the emergence of quantum spin liquids requires fine-tuned spin exchanges in a magnetically frustrated regime. This makes quantum spin liquids hard to be found in natural compounds. From the detection point of view, a direct local probe of the fractional excitations in these phases is challenging on physical grounds, and one relies on indirect signatures which might be hindered by other signatures or be explained with alternative mechanisms. These challenges motivate us to find tunable platforms to realize quantum spin liquids, where we benefit from the tunability (i) to reach fine-tuned regimes and (ii) to eliminate potential other mechanisms hindering the signature of quantum spin liquids.

Van der Waals materials, which are layered materials with two-dimensional nature due to the weak inter-layer van der Waals coupling, have been demonstrated as a highly tunable platform. The manipulation of electronic properties in van der Waals materials is much easier than that for bulk materials owing to their two-dimensional nature. Paradigmatic examples include gating [9] and straining [10] of van der Waals materials. Thanks to the technological advancements that allow atomic-scale manipulation, single impurities [11] can be used to engineer properties of van der Waals materials. A recent and remarkable experimental advance is the stacking and twisting of graphene multi-layers [12, 13]. By controlling the relative twist angle between the graphene multi-layers, a variety of strongly-correlated electronic phases can be realized in the graphene multilayers. Together with other engineering methods such as gating, the twisted multilayer offers a highly tunable platform to study strongly-correlated phases of matter.

However, an essential ingredient for quantum spin liquids, quantum magnetism, has been missing in van der Waals materials for a long time until the recent discovery of magnetic van der Waals materials [14–17]. Essentially, magnetic van der Waals materials 1T-TaS_2, 1T-$TaSe_2$ and α-$RuCl_3$ are potential quantum spin liquid candidates [18–21]. The experimental discovery of magnetic van der Waals materials and their relationship with quantum spin liquids motivate us to investigate how they can be engineered for the realization and identification of quantum spin liquids, in particular with scanning tunneling microscopes (STM). This will be the main theme of chapter 2.

Interestingly, the versatility of magnetic van der Waals materials allows the utilization of them in engineering other exotic phases of matter. In particular, helical states, an essential ingredient for topological superconductivity, can be engineered with magnetism and spin-orbit coupling. Magnetism is also an essential component of heavy fermions, which is an exotic phase related to unconventional superconductivity. Exploring the versatility of magnetic van der Waals materials in designing these exotic phases of matter is of great interest. This will be the main theme of chapter 3.

Finally, magnetic systems, when exposed to the environment, provide a paradigmatic example of open quantum systems in the presence of many-body interactions. Understanding the dynamics of such open quantum many-body systems is of great theoretical and technological interest. One particular interest is to engineer the coupling to the environment in order to turn the coupling useful, such as to engineer a symmetry-protected many-body topological phase. This will be the main theme of chapter 4.

The rest of the thesis is organized as follows: in chapter 5, I will present two computational libraries I developed during my Ph.D. studies. In chapter 6, I summarize the methods used in this thesis. A summary of this thesis is given in chapter 7.

2. Quantum spin liquids with magnetic van der Waals materials

Quantum spin-liquids (QSL) are highly-entangled magnetic phases of matter usually featuring strong magnetic frustration and zero local magnetic order [22–26]. Strong magnetic frustration refers to a situation when the energies of all local spins can not be minimized simultaneously with any configuration of the spins. Magnetic frustration usually takes place due to lattice geometry, such as on a triangular or Kagome lattice. As a consequence of magnetic frustration, a large number of magnetic configurations have the same energy, and the ground state becomes a superposition of all these states due to quantum fluctuations. This is usually referred to as the "Resonating Valence Bond" (RVB) state, proposed by Anderson in 1973 [27]. The RVB state provides a way of understanding the high entanglement in quantum spin liquids: Due to the massive superposition of magnetic configurations in the ground state, magnetic moments from far apart are entangled with each other. As a consequence of this long-range entanglement, QSL can have non-local fractional excitations: they can only be excited in pairs by local physical operators. Associated with these fractional excitations there is usually emergent gauge degrees of freedom, which is another feature of QSL.

The fractional excitations are one reason we study QSL: not only for their fundamental interest, but also for their potential applications in topological quantum computing [28, 29]. Another interest in QSL is due to that doping a QSL is believed to give rise to unconventional superconductivity [27, 30].

Despite its fundamental and technological interest, the experimental identification of QSL has proven to be a remarkable challenge. In particular, directly identifying the features of QSL: (i) the non-local entanglement, (ii) the fractional excitations or (iii) the emergent gauge fields represent a big challenge. The characterization of QSL has thus mostly relied on indirect signatures such as the absence of sharp dispersion for spin excitations

through inelastic neutron scattering [31], or the violation of Curie-Weiss law for magnetic susceptibility at low temperature [32].

Another difficulty for QSL is the lack of natural compounds having QSL as the ground state. This is due to the crucial requirements for having a QSL. First of all, the material candidate for QSL should have a frustrated lattice structure, preferably a triangular, honeycomb or Kagome lattice. In addition to this, the material should fall into the fine-tuned parameter regime where QSL is the ground state, which is not highly probable.

The recently raised 2D magnetic materials such as TaS_2 [18, 33, 34], $TaSe_2$ [20] and $RuCl_3$ [35, 36] have been proposed as QSL candidates, which paves the way to overcome the difficulties in the study of QSL physics. Using STM on 2D magnetic materials, one can perform inelastic tunneling measurements in a much more versatile way than inelastic neutron scattering. In addition, the 2D nature of these materials enables versatile engineering of them, allowing to drive them toward the QSL phase.

In this chapter, we present our theoretical proposals for identifying QSL phases in 2D magnets and driving a 2D magnet toward the QSL phase. We give a brief introduction to the material of our interest, 1T-TaS_2, and the potential U(1) Dirac QSL phase in this material in Sec.2.1. We then show that by manipulating single magnetic impurities on a 2D QSL material, we can probe the QSL with scanning tunneling microscope, allowing a more versatile probe of QSL than conventional scattering experiments for 3D QSL candidates in Sec.2.2. We show that by stacking two 2D QSL with a relative twist angle, we can tune properties of fractional excitations, which also allows to probe QSL with STM in Sec.2.3. These pave the way to overcoming the challenge of experimentally identifying QSL. Finally, we show in Sec.2.4 that, by tuning the dielectric environment of a magnetic van der Waals material, we can tune it towards QSL. This paves the way towards solving the problem of the lack of QSL candidates.

2.1 1T-TaS_2 and U(1) Dirac QSL

The material we would like to focus on in this chapter is 1T-TaS_2 (Fig. 2.1(a)), which is a transition metal dichalcogenide (TMD) where the Ta atoms form a triangular lattice. 1T-TaS_2 hosts a charge-density-wave (CDW) instability leading to the formation of the Star-of-David (SOD) unit cell with 13 Ta atoms at low temperature (Fig. 2.1(b)) [18, 37–41]. The CDW as

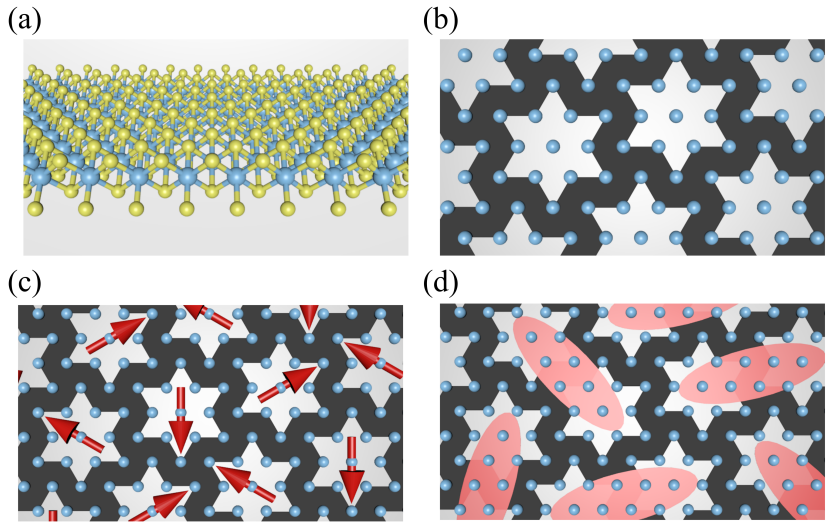

Figure 2.1. (a) Sketch of 1T-TaS_2, with a single layer of Ta atoms (blue) forming a triangular lattice, and two layers of Sulfur atoms (yellow). (b) Sketch of the star-of-David CDW in 1T-TaS_2, with 13 Ta atoms per Star-of-David. (c) Sketch of the potential spiral GS of 1T-TaS_2. (d) ketch of the potential QSL GS of 1T-TaS_2.

well as spin-orbit coupling (SOC) result in a half-filled narrow band at the Fermi energy, with a bandwidth of a few 10meV [42]. Together with sizable Coulomb interactions [43] this renders 1T-TaS_2 a correlated insulator rather than a simple metal. The electrons form local magnetic moments with $S = 1/2$ at each SOD, and interact via exchange and superexchange coupling (Fig. 2.1(a)).

Effectively, 1T-TaS_2 can be modeled with a Heisenberg model on the triangular lattice:

$$\mathcal{H} = \sum_{ij} J_{ij}^{\mu\nu} S_i^{\mu} S_j^{\nu} \tag{2.1}$$

where $J_{ij}^{\mu\nu}$ is the spin exchange between spin components μ, ν on site i, j. Since the spin-anisotropy in 1T-TaS_2 is weak, we can assume the spin exchanges to be isotropic, and Eq.(2.1) reduces to the Heisenberg model

$$\mathcal{H} = \sum_{ij} J_{ij} \mathbf{S}_i \cdot \mathbf{S}_j. \tag{2.2}$$

On the triangular lattice, the above model is known to give rise to a variety of phases in different parameter regimes, such as the spiral GS (Fig. 2.1(c)) and the U(1) Dirac QSL (Fig. 2.1(d)).

To illustrate the physics of U(1) Dirac QSL, we consider the following

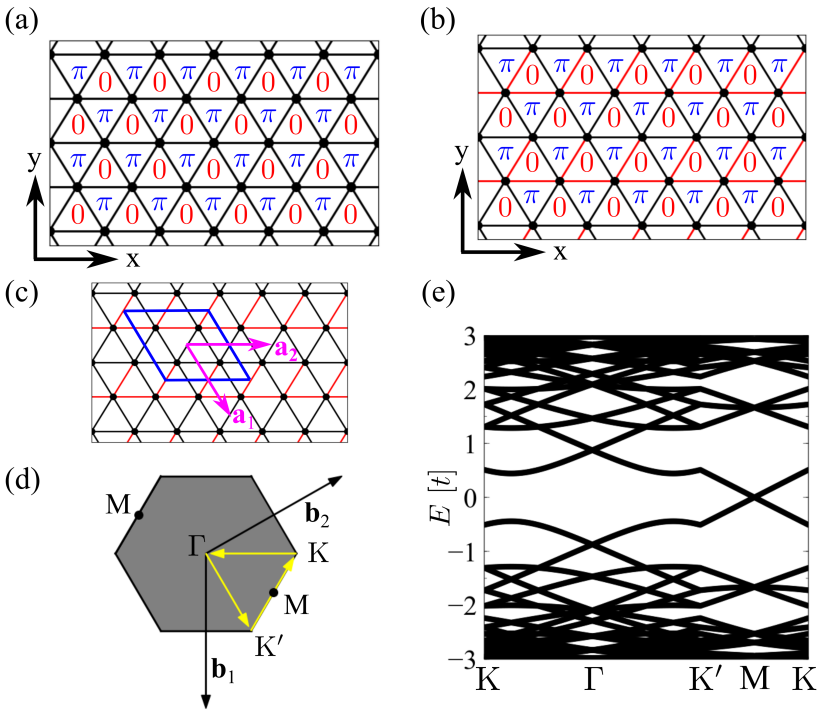

Figure 2.2. (a) Sketch of the π-flux model on the triangular lattice. (b) The hoppings in the π-flux model under a specific gauge choice. Black lines represent $t = 1$ and red lines represent $t = -1$. (c) The 2×2 unit-cell of the π-flux model (blue) and the unit-vectors (pink). (d) The Brillouin zone (grey) of the π-flux model corresponding to the choice of unit-cell in panel (c). High symmetry points are indicated. (e) The band structure of the π-flux model along the yellow path in panel (d).

parton transformation:

$$\mathbf{S}_i = \frac{1}{2} \sum_{\alpha,\beta} f^\dagger_{i,\alpha} \vec{\sigma}_{\alpha\beta} f_{i,\beta} \tag{2.3}$$

where α, β are spin degrees of freedom and $f, f^\dagger$ are fermionic operators satisfying $\sum_\alpha f^\dagger_{i,\alpha} f_{i,\alpha} = 1$. The fermionic partons are usually referred to as spinons, as they are fractional particles of half spin and zero charge. With the parton transformation, Eq.(2.2) becomes

$$H = \sum_{i,j} J_{ij} \left(\frac{1}{2} f^\dagger_{i,\alpha} f_{i,\beta} f^\dagger_{j,\beta} f_{j,\alpha} - \frac{1}{4} f^\dagger_{i,\alpha} f_{i,\alpha} f^\dagger_{j,\beta} f_{j,\beta} \right) \tag{2.4}$$

Under proper parameter regime, the ground state of the above Hamiltonian is given by a parton mean-field model with staggered 0 and π fluxes [44, 45](Fig. 2.2(a)):

$$H = t \sum_{\langle i,j \rangle} \chi_{ij} f^\dagger_i f_j. \tag{2.5}$$

We note that χ_{ij} is subject to a U(1) gauge degree of freedom: redefining $f_i \to e^{i\theta_i} f_i$. we have $\chi_{ij} \to \chi_{ij} + \theta_i - \theta_j$. The χ_{ij} under a specific gauge is illustrated in Fig. 2.2(b). The π-flux model Eq. (2.5) has translational symmetry, allowing us to use Bloch's theorem to compute its band structure. The 2×2 unit-cell for the π-flux model and the corresponding Brillouin zone are shown in Figs. 2.2(c) and (d). The band structure of the π-flux model under the gauge choice in Fig. 2.2(b) is shown in Fig. 2.2(e), highlighting the low-energy Dirac dispersion of the partons. The U(1) gauge degree of freedom together with the low-energy Dirac spinon dispersion explain the name "U(1) Dirac QSL".

We note that the full low-energy description of the U(1) Dirac QSL should involve both (i) Eq. (2.5) which describes the dispersion of the spinons due to coupling to the gauge field χ_{ij} and (ii) The action of the U(1) gauge field χ_{ij}, which describes the fluctuations of the gauge field χ_{ij}. However, solving the full problem represents a big challenge. We will thus neglect gauge fluctuations from now on and focus on how the low-energy Dirac dispersion of spinons can result in characteristic features of the U(1) Dirac QSL, in particular under specific engineering.

2.2 Impurity states in U(1) Dirac QSL

Impurity engineering has been recognized as a powerful technique to identify exotic electronic orders [46]. This includes the identification of unconventional superconductors with non-magnetic impurities, where the emergence of impurity-induced in-gap states is a well-known signature of unconventional superconductivity [47–50]. In contrast, conventional s-wave superconductors will only show in-gap states in the presence of magnetic impurities [51–54]. Another example is using impurities to image the Fermi surface of metals, by measuring Friedel oscillations with scanning probe techniques [55–57]. Another well-studied example is carbon vacancies [58–64] and hydrogen ad-atoms [65, 66] in graphene, that gives rise to a divergent density of states [59, 63] and magnetism [11, 60, 66].

Recently, the possibility of single atom manipulation has been explored with scanning probe techniques [67–83]. This motivates whether single atoms on top of 1T-TaS_2 can allow to detect the unique features of the potential U(1) Dirac QSL state.

2.2.1 Impurity states in graphene

Before we illustrate the identification of U(1) Dirac QSL with impurity engineering, let us first review the theory of graphene and how a divergent DOS appears at the Fermi energy in the presence of carbon vacancies or hydrogen adatoms.

Graphene is a 2D material with carbon atoms on a honeycomb lattice. The electronic model of graphene is simply a nearest-neighbour tight-binding model on the honeycomb lattice:

$$H = t \sum_{\langle i,j \rangle} (c_i^\dagger c_j + h.c.) \tag{2.6}$$

The 2nd nearest neighbour hopping in graphene is much smaller than the first ($t' \approx 0.1t$), thus we neglect it. The honeycomb lattice has the periodic structure of a triangular lattice with 2 sublattices. Using Bloch's theorem, we get the Bloch Hamiltonian of graphene:

$$H(\mathbf{k}) = \begin{pmatrix} & f^*(\mathbf{k}) \\ f(\mathbf{k}) & \end{pmatrix} \tag{2.7}$$

where $f(\mathbf{k}) = 1 + e^{i\mathbf{k}\mathbf{a_1}} + e^{i\mathbf{k}\mathbf{a_2}}$ with $\mathbf{a_{1,2}}$ being the lattice constants (Fig.2.3(a)). The band structure of graphene can thus be computed, showing the low-energy Dirac dispersion of graphene at K and K' points (Fig.2.3(b)).

The presence of a carbon vacancy or a Hydrogen adatom removes the free electron from one site, and effectively gives rise to a tight-binding model with a vacancy:

$$H = t \sum_{\langle i,j \rangle, i,j \notin \mathcal{K}} (c_i^\dagger c_j + h.c.) \tag{2.8}$$

where $\mathcal{K}$ is the site of the vacancy. To show the impurity effects, we consider a periodic array of impurities, with one impurity in a unit cell of size 4×4. In this case, the Bloch theorem still holds, and we can compute the band structure, where we observe the emergence of dispersionless modes at the Fermi energy (Fig.2.3(c)).

The difference between the spectrum of pristine graphene and defective graphene can be probed by STM, where the tunneling current is proportional to the density of states (DOS)

$$\rho(E) = \delta(E - H) = \sum_n \delta(E - E_n) \tag{2.9}$$

where E_n are the eigenvalues of H. For pristine graphene, the DOS is zero right at the Fermi level ($E = 0$), and grows linearly with E (Fig.2.3(d)).

This is in agreement with the low energy Dirac dispersion around the Fermi level. For defective graphene, the DOS exhibits a peak around the Fermi level, and does not show a significant change otherwise. The existence of the peak is consistent with the zero mode in Fig.2.3(c).

When we have a single vacant site in an infinitely large honeycomb lattice, the DOS can be computed with the embedding method introduced in Sec.6.1, where the peak at $E = 0$ still exists. We thus conclude that the zero mode induced by the carbon vacancy/hydrogen adatom and correspondingly the divergent DOS at Fermi level is a characteristic feature of the low energy Dirac dispersion of graphene. This motivated us to investigate whether impurities would allow to characterize the U(1) Dirac QSL state where the low-energy spinon dispersion is also Dirac.

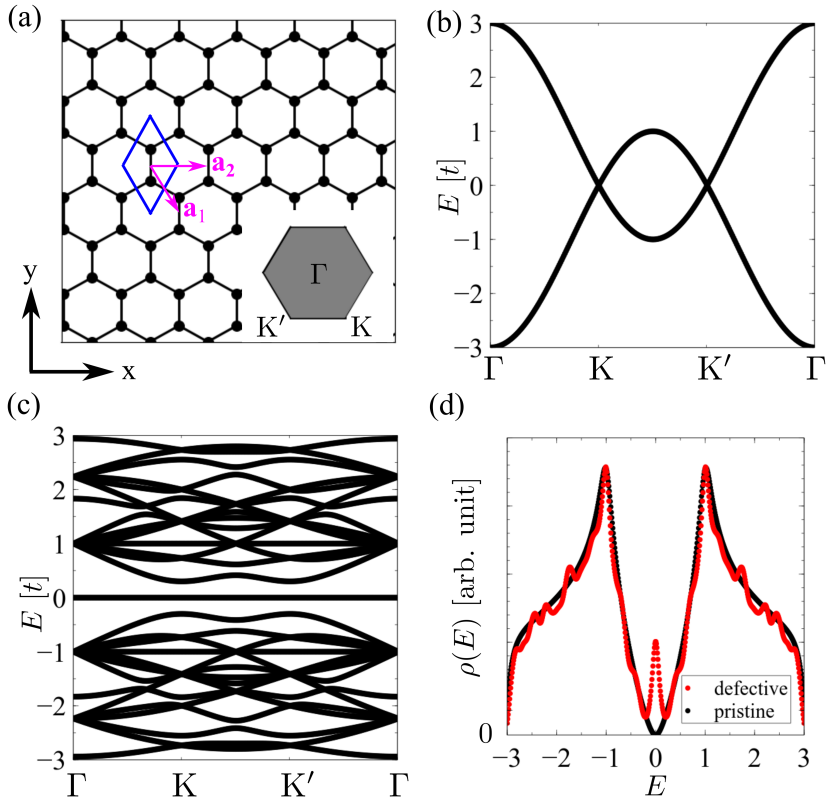

Figure 2.3. (a) Sketch of the tight-binding model Eq. (2.6) on the honeycomb lattice, with the unit-cell (blue) and unit-vectors (pink) indicated. The inset shows the first Brillouin zone and the high-symmetry points. (b) The band structure for graphene, computed with the Bloch Hamiltonian Eq. (2.7) along the path of high-symmetry points. (c) The band structure of graphene when there exists a vacant site in every 4×4 unit cell. (d) The density of states $\rho(E)$ for pristine and defective graphene, corresponding to panels (b) and (c), respectively.

2.2.2 Impurity states in Dirac QSL

We now consider the case of a magnetic impurity in the U(1) Dirac QSL[1]. We assume that the magnetic impurity couples locally to one spin:

$$\mathcal{H} = \mathcal{J} \sum_{k \in \mathcal{K}} \mathbf{s}_k \cdot \mathbf{S}_k + \sum_{ij} J_{ij} \mathbf{S}_i \mathbf{S}_j \tag{2.10}$$

where $\mathbf{s}_k$ are the spin operators for the different $S = 1/2$ ad-atoms considered, $\mathcal{K}$ denotes the sites that have an impurity ad-atom on top, and $\mathcal{J}$ is the antiferromagnetic exchange coupling between the magnetic ad-atom and the site below. Taking the limit of strongly coupled magnetic impurity $\mathcal{J} \gg J_{ij}^{\mu\nu}$, the different sites k will form a singlet state with the impurity on top, effectively removing the $S = 1/2$ from the quantum spin-liquids compound. As a result, the effective Hamiltonian in this limit is (Fig.2.4(a))

$$\mathcal{H} = \sum_{ij, i \notin \mathcal{K}, j \notin \mathcal{K}} J_{ij} \mathbf{S}_i \mathbf{S}_j, \tag{2.11}$$

an effective triangular model where the sites hosting a magnetic impurity above disappear from the low-energy Hamiltonian. Using an analogous parton transformation as before, we obtain that the effective model for the spinons becomes (Fig.2.4(b))

$$H = t \sum_{\langle i,j \rangle, i \notin \mathcal{K}, j \notin \mathcal{K}} \chi_{ij} f_i^\dagger f_j, \tag{2.12}$$

an effective $\pi-$flux model with impurities determined by the magnetic ad-atoms deposited.[2] We note that this equivalence holds only for $S = 1/2$ impurities, as higher S impurities would generate a free degree of freedom in each site even in the limit $\mathcal{J} \gg J_{ij}^{\mu\nu}$. We also note that given that the magnetic ad-atoms on top can be moved with a scanning tunnel microscope, [68–70, 72–83] this would allow to engineer models with an arbitrary number of vacancies in the effective spinon model.

Under the above approximations, we see that magnetic impurities on the Dirac QSL modify the spinon dispersion by effectively adding vacant sites to the mean-field spinon π-flux model. We illustrate below the change to the spinon dispersion for (i) a periodic array of impurities and (ii) a single impurity in an infinitely large system.

[1] Part of this and the next subsection are adapted from G. Chen and J. L. Lado, Phys. Rev. Research 2, 033466 (2020).

[2] We assume that the mean field spinon model does not have non-trivial reconstructions.

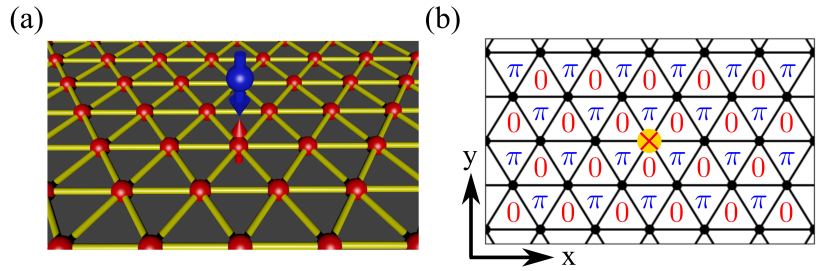

Figure 2.4. (a) Sketch of a magnetic impurity coupled to a $U(1)$ Dirac quantum spin-liquid. (b) The effective spinon mean-field model for (a).

When considering a periodic array of impurities in unit cells of size $n \times m$, the Bloch Hamiltonian can be used to compute the band structure and the density of states (DOS). Compared to the band structure of the pristine π-flux state, a flat band at zero energy arises for n even [Fig.2.5(b)], and a band with small dispersion near zero energy arises for n odd [Fig.2.5(c)]. In both cases, the DOS at zero frequency shows a dramatic increase [Fig.2.5(d)]. The dispersion in the odd n case stems from interference effects between different impurity-induced modes, which are absent in the even n case. The spatial distribution of the zero modes can be analyzed by looking at the local density of states (LDOS), defined as

$$\rho(\mathbf{r},\omega) = \mathrm{Im}\left(\langle \mathbf{r}|[\omega - H - i0^{+}]^{-1}|\mathbf{r}\rangle\right). \tag{2.13}$$

In particular, the LDOS at zero frequency $\rho(\mathbf{r},\omega=0)$ shows that the zero modes are localized around the impurities [Fig.2.5(e)], showing a pattern with local C_6 rotational symmetry. Interestingly, the zero modes are mainly localized through sites that are odd number of bonds straight away from the impurity. The above calculation relies on assuming a periodic pattern of impurities. Experimentally, the simplest scenario will be depositing a single impurity in an infinite large QSL. In the following we will deal with this idealized case, showing that the results are qualitatively similar to the periodic impurity pattern considered above.

We now move on to consider a single impurity coupled to the quantum spin-liquid. In the case of a single impurity in an infinite system, translational symmetry is broken and Bloch theorem does not apply. To deal with this inhomogeneous infinite problem, we compute exactly the spectral function close to the impurity using the Green's function embedding method in Sec.6.1. The DOS is found to be divergent at zero frequency for a defective unit cell [Fig.2.5(f)], indicating the existence of zero modes.

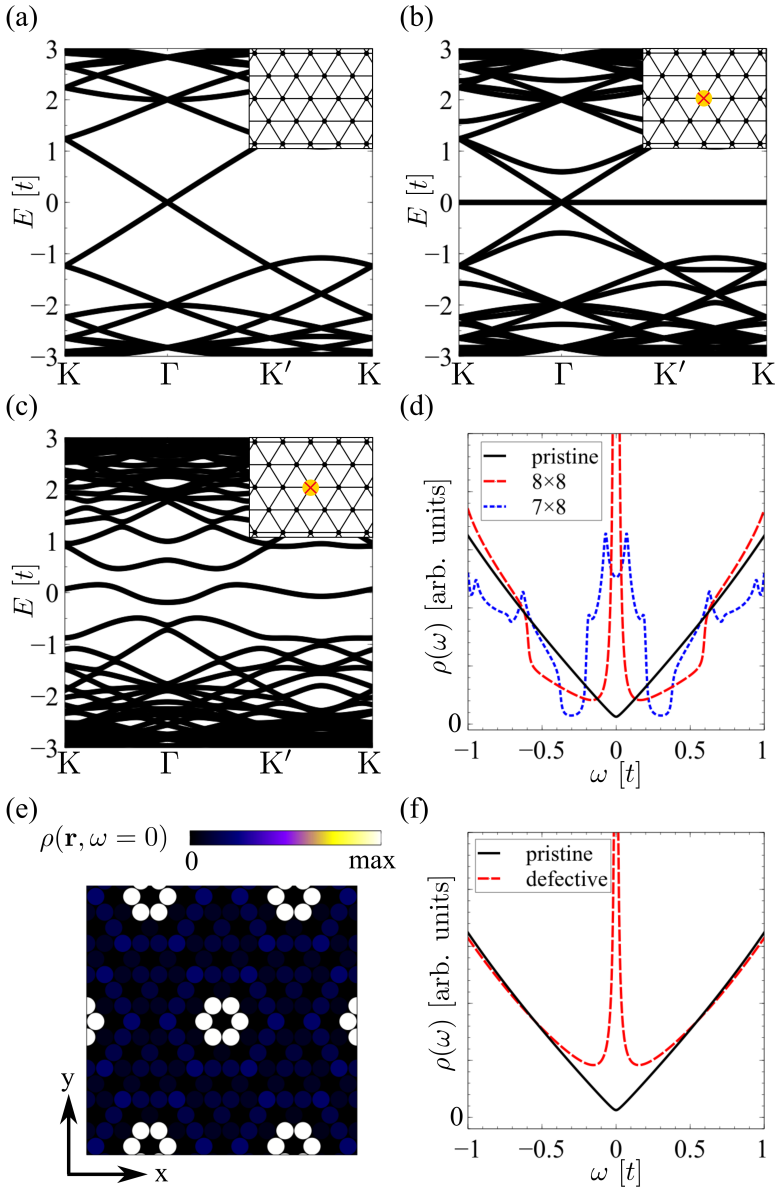

Figure 2.5. Spinon dispersion in pristine and defective π-flux Dirac QSL. Panel (a) shows the pristine spinon band structure of a π-flux QSL in an 8×8 unit cell. Panels (b) and (c) show the spinon band structure with a periodic array of impurities in an 8×8 and a 7×8 unit cell, respectively. The insets show the configurations of the impurity. Panel (d) shows the spinon DOS corresponding to the three cases (a-c). The divergent spinon DOS at zero frequency corresponding to case (b) indicates the existence of zero modes, in agreement with the band structure shown in (b). Panel (e) shows the spinon LDOS at zero frequency $\rho(\mathbf{r}, \omega = 0)$ for case (b). The zero modes are localized around the impurities, displaying a pattern with local C_6 rotational symmetry. Panel (f) shows the spinon DOS of the pristine QSL, and for a single impurity in an infinite QSL.

We note that when there are several impurities, different impurity-

induced modes will interfere with each other, resulting in dispersive spinon modes near the Fermi level. In this case, the DOS shows a less sharpened peak at Fermi level [84].

We have thus verified the existence of spinon zero modes when there is (i) a periodic array of impurities with one in an $n \times m$ unit cell with n even and (ii) a single impurity in an infinite system. The results resemble that for graphene [63] as we showed in the last section, highlighting that impurity in a system with low-energy Dirac dispersion gives rise to zero modes. However, the spinon zero modes in U(1) Dirac QSL have different nature than the electronic zero modes in graphene. Due to the fractional nature of spinons, we cannot directly probe spinon zero modes with STM. We address in the next section how indirect signatures in STM measurements indicate the existence of spinon zero modes.

2.2.3 Experimental detection of spinon zero modes

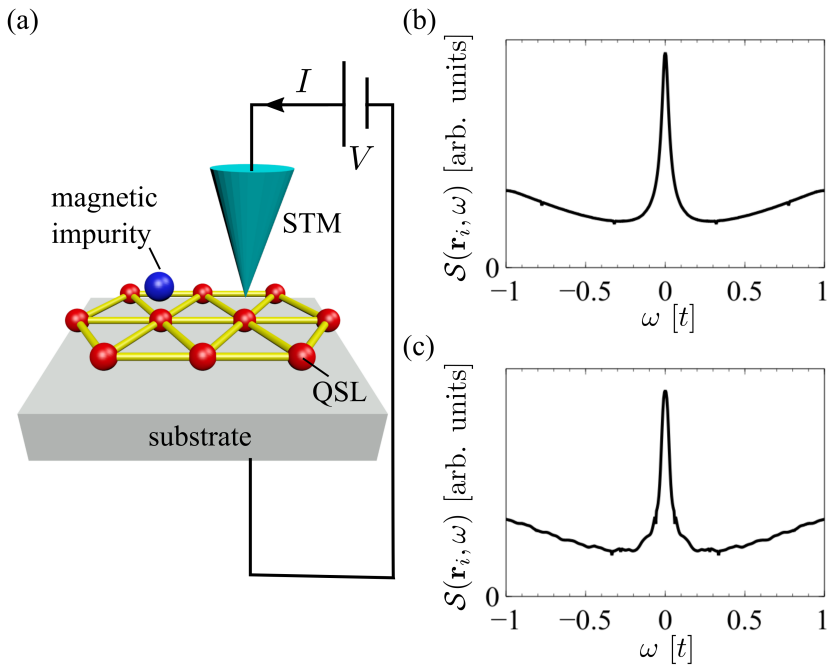

Figure 2.6. (a) Sketch of the experimental setup to measure the resonant Dirac spinons close to the impurity by means of inelastic spectroscopy or electrically driven paramagnetic resonance. Panels (b) and (c) show the local spin structure factor $\mathcal{S}(\mathbf{r}_i, \omega)$, computed on the site near the impurity, for (b) a single impurity in an infinite system and for (c) a single impurity in a large finite system (with 100×100 sites). It is observed that a zero bias peak appears, which is associated with the original divergent spinon density of states at zero frequency.

We now show how the spinon zero modes can be indirectly probed with

STM in the setup shown in Fig.2.6(a), allowing for experimental identification of U(1) Dirac QSL. STM can be utilized to measure the tunneling rate of an electron into the material through inelastic processes, with direct access to this quantity in d^2I/dV^2 [70, 80, 85, 86]. The tunneling rate Γ of an inelastic process exciting a quasiparticle is given by

$$\Gamma \sim \langle \mathrm{GS}|O\delta(\omega - \mathcal{H} + E_{\mathrm{GS}})O^\dagger|\mathrm{GS}\rangle \tag{2.14}$$

where $O^\dagger$ is the operator creating the excitation above the groundstate, $|\mathrm{GS}\rangle$ is the ground state of $\mathcal{H}$ and E_{GS} is the ground state energy. In the case of QSL, the excitations are magnons, which are composed of two spinons. Thus, the tunneling rate is given by the convolution of the spinon DOS to itself, giving rise to a peak at 0. We provide a quantitative analysis below. Due to the fact that the spin Hamiltonian $\mathcal{H}$ in Eq. (2.11) is spin-isotropic, the tunneling rate for exciting a local magnon is proportional to

$$\mathcal{S}(\mathbf{r}_i, \omega) = \langle \mathrm{GS}|S_i^+\delta(\omega - \mathcal{H} + E_{\mathrm{GS}})S_i^-|\mathrm{GS}\rangle \tag{2.15}$$

where $S_i^\pm = S_i^x \pm iS_i^y$. $\mathcal{S}(\mathbf{r}_i, \omega)$ is usually referred to as the (local) spin structure factor. As the magnon is composed of 2 spinons, the spin structure factor would be proportional to the density-density response function for spinons [84, 87]:

$$\mathcal{S}(\mathbf{r}_i, \omega) \sim \sum_{n,n'} \frac{f_n - f_{n'}}{\omega + \varepsilon_n - \varepsilon_{n'} + i\eta} \psi_n^*(\mathbf{r}_i)\psi_{n'}(\mathbf{r}_i)\psi_n(\mathbf{r}_i)\psi_{n'}^*(\mathbf{r}_i) \tag{2.16}$$

where $\psi_n(\mathbf{r}_i) = \langle \mathbf{r}_i|\psi_n\rangle$ is the n-th spinon eigenstate with energy ε_n, and f_n is the Fermi-Dirac distribution for spinons. Using the LDOS for spinons defined in Eq. (2.13), we can rewrite Eq. (2.16) as

$$\mathcal{S}(\mathbf{r}_i, \omega) \sim \int \mathrm{d}\omega_1 \mathrm{d}\omega_2 \frac{\rho(\mathbf{r}_i, \omega_1)\rho(\mathbf{r}_i, \omega_2)}{\omega + \omega_1 - \omega_2 + i\eta} \left(f(\omega_1) - f(\omega_2)\right). \tag{2.17}$$

The local spin structure factor is computed for the site near the impurity [Fig.2.6(b)], where the LDOS is computed using the embedding method introduced in Sec.6.1. Alternatively, we also show the spin structure factor computed for a finite island with 10000 sites [Fig.2.6(c)] using the kernel polynomial method (KPM) introduced in Sec.6.2. In both instances, a peak at zero frequency is observed, which is associated with the divergent density of states of the spinon excitations. In an STM experiment, this would infer a peak in differential conductance at zero bias.

We see that the zero bias peak in the STM measurement near the impurity can be a hint for the existence of spinon zero modes and the U(1) Dirac

QSL. Interestingly, zero bias peaks in inelastic spectroscopy in the presence of magnetic impurity are usually associated with the Kondo physics. In this line, our results put forward a different mechanism for the explanation of the zero bias peaks.

2.2.4 Summary

We showed that individual magnetic $S = 1/2$ impurities coupled to a U(1) Dirac QSL results in zero bias peaks in inelastic spectroscopy with STM. This stems from the emergence of spinon zero modes due to the low-energy Dirac dispersion of the spinons. This impurity-induced zero bias peak provides a potential identification of U(1) Dirac QSL.

2.3 Twisted Dirac QSL

Stacking van der Waals heterostructures yields electronic structures sensitive to the relative twisting between different layers. [88,89]. A remarkable example is twisted bilayer graphene, where the emergence of flat bands at magic twist angles has led to a variety of unconventional many-body states [12, 13, 90–92]. Interestingly, twist engineering generically provides a highly-tunable platform [93–95] for correlated phases and topologically nontrivial electronic structures [96–101]. The versatility offered by stacked van der Waals heterostructures motivates us to search for analogous phenomena in van der Waals magnets [102–104]. In particular, we are interested in novel spinon phenomena in a twisted U(1) Dirac QSL system that allows for the detection of spinons and the identification of the U(1) Dirac QSL.

2.3.1 Twisted bilayer graphene

Twisted bilayer graphene (TBG) has been realized as a highly-tunable system hosting a rich amount of strongly correlated electronic phases. The tunability refers to the high sensitivity of the electronic band structure of the bilayer graphene to the relative twist angle between the two graphene layers as well as to external tuning such as an electronic bias. The fact that it is a versatile platform for strongly correlated physics is due to the emergence of flat electronic bands at certain twist angles, usually referred to as the magic angles. We illustrate the above points by showing the band structure of TBG at the non-interacting level.

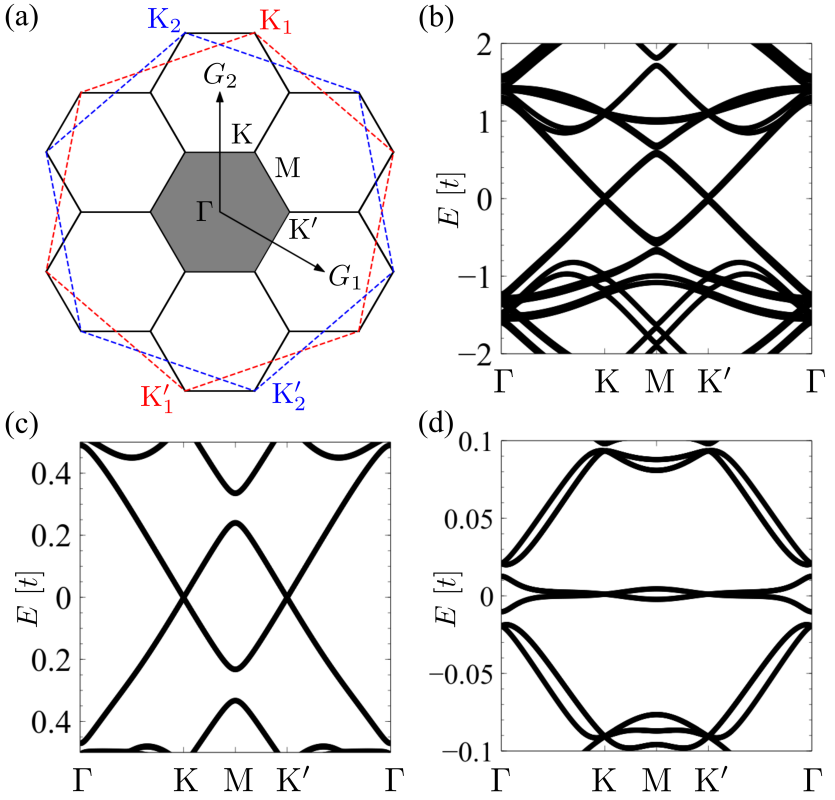

Figure 2.7. (a) The Brillouin zone of twisted bilayer graphene at twist angle $\theta = 21.79°$ (grey region) with high-symmetry points indicated. The Brillouin zone of the two graphene layers are indicated with red and blue hexagons where the K and K′ valleys are also indicated. The reciprocal vectors G_1 and G_2 for twisted bilayer graphene are also shown. (b)-(d) Electronic band structure of twisted bilayer graphene at twist angle (b) $\theta = 21.79°$, (c) $\theta = 9.43°$ and (d) $\theta = 1.89°$.

The bilayer graphene can be modeled as:

$$H = \sum_{l,\langle i,j\rangle} t c^{\dagger}_{i,l} c_{j,l} + \sum_{i,j} t_{\perp,ij} (c^{\dagger}_{i,1} c_{j,2} + h.c.) \tag{2.18}$$

where $l = 1, 2$ is the layer index. The first term of Eq. (2.18) describes the intra-layer hopping of graphene and the 2nd term describes the inter-layer coupling between the two graphene layers. As the inter-layer coupling is given by the van der Waals force, it is much smaller than the intra-layer coupling. The inter-layer coupling between site i on layer 1 and site j on layer 2 depends on the overlap of the wannier orbitals, that depends on the inter-layer distance d and the distance r_{ij} between sites i and j. Precise modeling of this would require ab initio computations. Interestingly, the low-energy spectrum of TBG exhibits universal features independent of the details of the functional form of inter-layer coupling. In the following,

we choose [88, 105]

$$t_{\perp,ij} = t_{\perp,0}\frac{d^2}{r_{ij}^2}e^{-\lambda(r_{ij}-d)} \tag{2.19}$$

where $t_{\perp,0}$ is the inter-layer coupling between two sites with the same horizontal position, and λ is a parameter that determines the decay of the inter-layer hopping. For computational convenience we choose $t_{\perp,0} = 0.3t$ and $\lambda = 10a^{-1}$ where a is the lattice constant of graphene. We note that a re-scaling relation [106–108] would allow to relate our result to other values of $t_{\perp,0}$. Finally, as a reference, the hopping constants for graphene are $t \approx 3$ eV and $t_\perp^0 \approx 500$ meV [109].

We start with a large twist angle $\theta = 21.79°$, at which the first Brillouin zone of the TBG is shown in Fig.2.7(a). The band structure shown in Fig.2.7(b) highlights that (i) the Dirac cones are not significantly splitted, (ii) there are some band splittings at M and Γ point, which flattens the low-energy bands and (iii) particle-hole symmetry is broken, but approximate particle-hole symmetry holds at low-energy. These features persist at smaller twist angles as shown in Figs.2.7(c,d). In particular, the low-energy bands get significantly flattened at smaller twisted angles and becomes almost flat at the twist angle $\theta = 1.89°$. The flattening of the low-energy bands can be understood as a consequence of the inter-layer coupling, that induces the splitting of the bands.

We have thus seen the sensitive dependence of the low-energy band structure of twisted bilayer graphene to the twist angle, and that flat band emerges at certain magic twist angles. One way of interpreting this is the inter-layer coupling results in a splitting between the bands from the two layers. We note that there exist other instructive interpretations for the low-energy band structure of TBG. For instance, TBG can be understood as a moire potential on single-layer graphene due to the relative twist. At the low-energy level, this moire potential is a non-Abelian gauge potential coupled to the Dirac electrons in single-layer graphene, which also exhibits flat bands at certain twist angles [110].

Finally, we would like to note that the low-energy bands in TBG have emergent valley conservation. The low-energy bands at K_1 will only hybridize with that at K_2, and not with $K'_{1,2}$ due to the distance in the Brillouin zone (Fig.2.7(a)). Similarly, the bands at K'_1 only hybridize with K'_2. Thus, the hybridized low-energy bands in TBG belong to either the valley K_1+K_2 or the valley K'_1+K'_2. The valley operator allows for the characterization of the valley expectation of a certain state [94, 111–114].

The low-energy bands in TBG exhibit a valley degeneracy. Together with the spin degeneracy, this provides the emergent SU(4) symmetry of the low-energy bands of TBG.

2.3.2 Twisted U(1) Dirac QSL

We investigate the spinon band structure of twisted U(1) Dirac QSL in this section[3]. Due to the similarity between the spinon dispersion in U(1) Dirac QSL and the electronic dispersion in graphene, we would expect that (i) the low-energy Dirac spinon dispersion is protected at small twist angles, (ii) spinon flat bands arise at certain twist angles. We show below that (i) no longer holds due to the different symmetry of the twisted π-flux model.

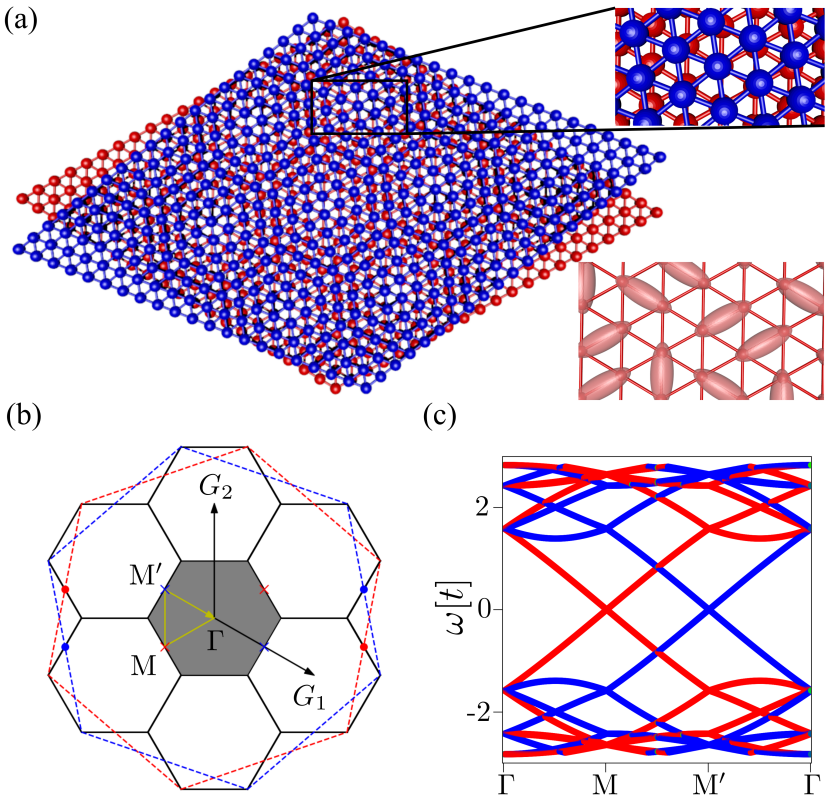

Figure 2.8. (a) Sketch of a twisted bilayer Dirac QSL on a triangular lattice. (b) The Moire Brillouin zone for twisted QSL. The dashed red and blue hexagons represent the Brillouin zone for the bottom and top layers. The red/blue circles (crosses) denote the location of the Dirac points in the original (folded) Brillouin zone (grey area). (c) Spinon band structure of the twisted Dirac QSL in the decoupled limit for $\theta = 22^\circ$, showing the two sets of decoupled bands in the top (blue) and bottom (red) layers.

[3]Part of this and the next subsection are adapted from G. Chen and J. L. Lado, Phys. Rev. Research 3, 033276 (2021).

We start with the Heisenberg model for the $U(1)$ Dirac QSL Eq. (2.2), and consider a twisted bilayer of such QSL as sketched in Fig.2.8(a).The Heisenberg Hamiltonian for the twisted bilayer takes the form

$$\mathcal{H} = \sum_{l,i,j} J^{\mu\nu}_{\parallel,ij} S^{\mu}_{i,l} S^{\nu}_{j,l} + \sum_{i,j} J^{\mu\nu}_{\perp,ij} S^{\mu}_{i,1} S^{\nu}_{j,2}, \tag{2.20}$$

where l labels the two layers, and $J^{\mu\nu}_{\parallel,ij}$ and $J^{\mu\nu}_{\perp,ij}$ denote intra- and inter-layer spin exchange, respectively. In the regime $J^{\mu\nu}_{\parallel,ij} \gg J^{\mu\nu}_{\perp,ij}$, the ground state of the system will consist of two coupled $U(1)$ QSL states. Therefore, we take as the mean-field solution for each layer the spinon π-flux model, with an effective inter-layer spinon coupling from inter-layer spin exchange:

$$H = t \sum_{l,\langle i,j\rangle} \chi_{l,ij} f^{\dagger}_{i,l} f_{j,l} + \sum_{i,j} t_{\perp,ij} (f^{\dagger}_{i,1} f_{j,2} + h.c.), \tag{2.21}$$

where $t, \chi_{l,ij}$ and $t_{\perp,ij}$ are mean-field parameters that can be derived analogously from a mean-field replacement in Eq. (2.20). The mean-field parameter $t_{\perp,ij}$ will depend on the relative distance between sites i and j, inherited from the parent Heisenberg coupling $J^{\mu\nu}_{\perp,ij}$ in Eq. (2.20). Similar to the computation of electronic band structure in TBG, we take the functional form for the inter-layer coupling as [105] $t_{\perp,ij} = t_{\perp,0} \frac{d^2}{r_{ij}^2} e^{-\lambda(r_{ij}-d)}$, where d is the inter-layer distance, r_{ij} is the distance between sites i and j, λ is the parameter that controls the decay of the inter-layer coupling, and $t_{\perp,0}$ is the largest possible inter-layer coupling realized at $r_{ij} = d$. In the following we take $t_{\perp,0} = 0.36t$, $\lambda = 10/a$, and $d = a$, where a is the lattice constant of the triangular lattice. From the computational point of view, we will use the twist scaling relation for computational convenience [106, 115]. Similar to TBG, the low-energy bands in twisted π-flux model Eq. (2.21) also exhibits emergent valley conservation, and we compute the valley expectation $\langle \mathcal{V}_z \rangle = \pm 1$ with the valley operator for the twisted π-flux model.

The π-flux hoppings $\chi_{l,ij}$ are subject to a $U(1)$ degree of freedom for each layer, respectively. However, the gauge difference between the two layers determines the relative position of Dirac cones of the two layers in reciprocal space [116]. As a result, the momentum difference between Dirac cones of the two layers, Δk, can be either large or small. When $|\Delta \mathbf{k}| \gg |1/\mathbf{R}|$, where $\mathbf{R}$ is the periodicity of $t_{\perp,ij}$ in real space, the Dirac cones are almost decoupled. In such case, the impact of $t_{\perp,ij}$ is small on low energy physics, keeping the two layers effectively decoupled. In

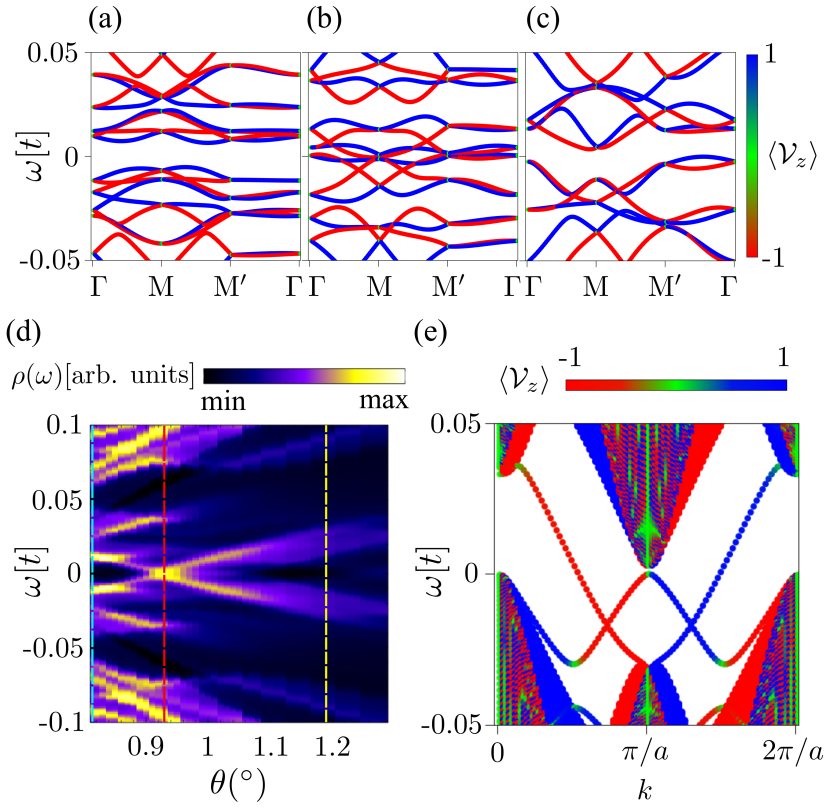

Figure 2.9. (a-c) Spinon band structure of twisted Dirac QSL for different twisting angles $\theta = 0.81^\circ, 0.93^\circ, 1.20^\circ$ (dashed lines in panel (d)), respectively. (d) Spinon DOS $\rho(\omega)$ for twisted Dirac QSL near the first magic angle $\theta = 0.93^\circ$. (e) Spinon band structure of a twisted QSL nanoribbon at $\theta = 3.5^\circ$.

contrast, when $|\Delta \mathbf{k}| \ll |1/\mathbf{R}|$, $t_{\perp,ij}$ leads to significant coupling between the Dirac cones of different layers. From the energetic point of view, this gauge configuration couples the two layers and therefore will lower the many-body energy through spinon hybridization. With this gauge choice, the Moire Brillouin zone is shown in Fig.2.8(b), with two Dirac cones at time-reversal invariant momenta M and M′. The spinon dispersion in the decoupled limit for twisting angle $\theta \approx 22^\circ$ is shown in Fig.2.8(c), where the two spinon Dirac cones of the two decoupled layers are observed.

Let us now move on to the case in which the two QSL are coupled through the inter-layer exchange coupling. In this situation, we find that the inter-layer coupling leads to a gap opening in the Dirac cones of the bilayer QSL upon twisting. This gap opening stemming from the twist is similar to the case of twisted double bilayer graphene [96] (Fig.2.9(a-c)), and stems from the broken $C_{2z}T$ symmetry [117,118] of the effective model.

Besides the gap opening, we also observe the emergence of spinon flat bands at a specific fine-tuned twisting angle $\theta/(t_\perp/t) \approx 2.6°$, which for $t_\perp = 0.36t$ appears at $\theta = 0.93°$ (Fig.2.9(d)), similar to other twisted Dirac materials [88, 89].

Interestingly, the emergence of a gap opening driven by the twist has been shown to give rise to topological states in van der Waals heterostructures based on graphene [119–121]. In particular, we find that the gap opening in the bilayer QSL has an associated valley Chern number of 2, giving rise to two counterpropagating channels at each edge with opposite valley polarization [122–126]. The previous phenomenology can be explicitly demonstrated by computing the spinon band structure of a twisted QSL nanoribbon at twisting angle $\theta = 3.5°$ (Fig.2.9(e)). In particular, it is clearly seen the emergence of in-gap valley-polarized topological edge modes, associated with the topological valley Hall quantum spin-liquid state. We note that the topological edge modes are protected by the approximate valley charge conservation, and therefore perturbations giving rise to strong inter-valley scattering can lead to inter-valley mixing between topological spinon edge states [113, 114, 125, 127, 128].

We see that similar to TBG, the twisted bilayer π-flux model exhibits band structure sensitive to the twist angle and flat bands at certain twist angles. It also exhibits different behaviour than TBG. In particular, the Dirac cones split at small twisting angles, opening a topologically non-trivial gap. This is due to the broken $C_{2z}T$ symmetry of the model under the specific gauge choice. We shall see in the next section how the spinon dispersion in this moire structure allows a characterization of U(1) Dirac QSL by means of magnetic encapsulation.

2.3.3 Tunability of spinon dispersion with magnetic encapsulation

One of the remarkable features of TBG is its sensitivity to external electric bias that allows for electric tunability of electronic structure in TBG [95]. We show here that in a similar manner, a magnetic tunability exists for the spinon dispersion in twisted U(1) Dirac QSL[4].

From the material science point of view, in the following we will consider that the QSL bilayer is sandwiched between two ferromagnetic insulators, for which both $CrBr_3$ [130, 131] and $CrCl_3$ would be suitable candidates. The top and bottom ferromagnets are expected to be antiferromagnet-

[4]This section is adapted from Ref. [129] with some modifications

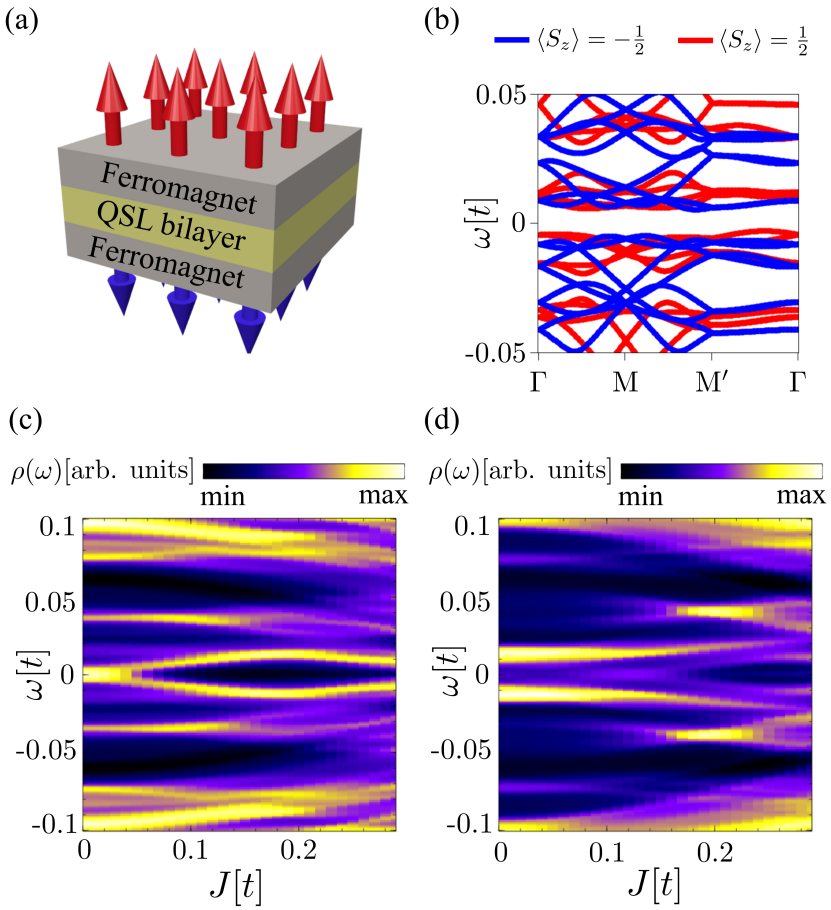

Figure 2.10. (a) Sketch of the twisted bilayer Dirac QSL encapsulated by ferromagnets. (b) Spinon band structure for the twisted Dirac QSL at $\theta = 0.93°$ and inter-layer spinon bias $J = 0.1t$. (c,d) Spinon DOS for the twisted bilayer Dirac QSL at (c) $\theta = 0.93°$ and (d) $\theta = 1.05°$ with different inter-layer spinon bias J.

ically aligned through a superexchange mechanism [132], as shown in Fig. 2.10(a). To study the impact on the QSL state, we now integrate out the degrees of freedom of the ferromagnet, and consider their impact on the QSL Hamiltonian. The magnetic encapsulation yields an exchange proximity term in the Hamiltonian of the QSL bilayer, analogous to the exchange terms proposed for other van der Waals materials proximized to ferromagnets [94, 133–136]

$$\mathcal{H}' = \mathcal{H} + \sum_{i,\mu} \mathcal{J}_\perp S^\mu_{i,1} \mathcal{M}^\mu_1 + \sum_{i,\mu} \mathcal{J}_\perp S^\mu_{i,2} \mathcal{M}^\mu_2, \tag{2.22}$$

where $\mathcal{J}_\perp$ denotes the exchange interaction between spin in the QSL $S^\mu_{i,l}$ and the magnetic moment of the ferromagnets $\mathcal{M}^\mu_l$, with $l = 1, 2$ labeling the two different magnets and QSL layers. We consider sufficiently small

$\mathcal{J}_\perp$ that does not lead to many-body reconstruction. In such case, the mean-field solution of Eq. (2.21) remains, and the effect of the ferromagnets can be projected onto the spinon mean-field Hamiltonian as

$$H' = H + \frac{1}{2}\sum_{i,\mu,l,s,s'} \mathcal{J}_\perp \sigma^\mu_{s,s'} \mathcal{M}^\mu_l f^\dagger_{i,s,l} f_{i,s',l}. \tag{2.23}$$

In the case of the antiferromagnetic alignment as depicted in Fig. 2.10(a), the magnetic encapsulation creates an effective spin-dependent inter-layer spinon bias $J = \mathcal{J}_\perp(\mathcal{M}^z_1 - \mathcal{M}^z_2)$ on the twisted Dirac QSL [94, 112, 133]. The effective inter-layer spinon bias J induced by proximity exchange fields has a dramatic impact on the low energy spinon band structure of the twisted Dirac QSL. Due to the broken mirror symmetry of the twisted QSL[5], the exchange bias causes spin-splitting in the spinon band structure in reciprocal space (Fig.2.10(b)). At the flat band twisting angle, the gap at Fermi level drastically increases with J (Fig.2.10(c)). When the twisting angle is not the flat one, the spinon DOS gets substantially modified at larger exchange couplings (Fig.2.10(d)).

The modification of the spinon DOS allows for the identification of the U(1) Dirac QSL with STM, in the same spirit as Sec.2.2.3. We now consider a similar setup, in which the magnetically encapsulated QSL bilayer is explored by means of vertical transport with STM as shown in Fig. 2.11(a). To reveal the impact of the magnetic encapsulation, we now consider the change of the signal with respect to an in-plane magnetic field B, that is used to control the direction of magnetism in the magnets. The magnetic field will tune the angle between the magnetization of the two magnets from π to $\pi - \alpha(B)$, and modifies spinon DOS in the QSL bilayer due to proximity effect. For twisting angle $\theta = 0.93^\circ$, and effective exchange bias $J = 0.1t$, the spinon DOS under different $\alpha(B)$ is shown in Fig. 2.11(b). The modified spinon DOS exhibits peaks at different frequencies than the original one. Taking the specific case of antiferromagnetic alignment $\alpha = 0$, it is seen that the spin structure factor has peak structures, inherited from the peaks in the spinon DOS (Fig.2.11(c)). Due to the modification of the spinon DOS with the field, an analogous effect is expected in the differential conductivity, which is proportional to the spin structure factor Eq. (2.17). For this sake, we now compute the change in the spin structure factor as a function of the magnetic field, defined as $\Delta\mathcal{S}(\omega, \alpha) = \mathcal{S}(\omega, \alpha) - \mathcal{S}(\omega, 0)$, and

[5]The mirror symmetry $M_x(M_y)$ is present if the system is invariant when mirrored by x (y) plane and then exchanging the top and bottom layers.

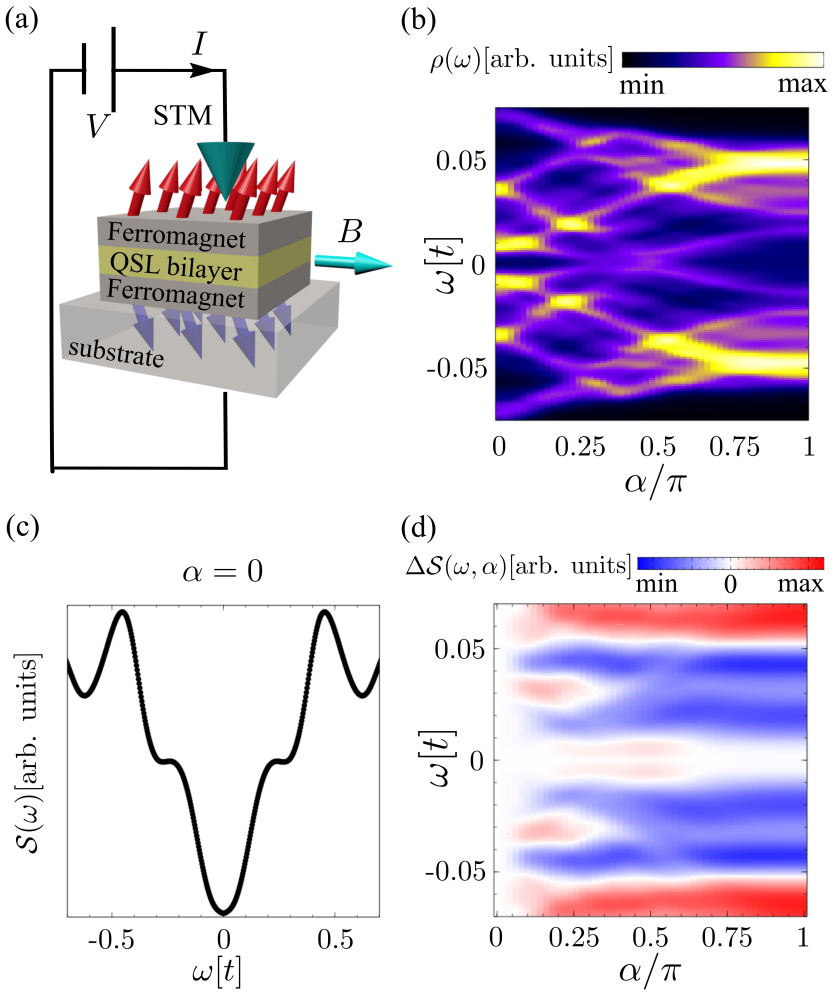

Figure 2.11. (a) Sketch of the experimental setup for probing QSL via inelastic spectroscopy. (b) Spinon DOS of twisted QSL at $\theta = 0.93^\circ$ and $J = 0.1t$ under different $\alpha(B)$. (c) Spin structure factor $\mathcal{S}(\omega)$ with $\alpha = 0$. (d) Change in spin structure factor $\Delta\mathcal{S}(\omega, \alpha)$ for different α.

shown in Fig. 2.11(d). In particular, we see in Fig. 2.11(d) the existence of deeps and peaks in d^2I/dV^2, manifesting from the dramatic change of spinon DOS with the magnetic field of Fig. 2.11(b).

Finally, we comment on specific quantitative aspects of our proposal relevant to experiments. First, we have considered exchange couplings between the two monolayer QSL on the order of $J_\perp \approx 0.3 J_{||}$. The specific prediction of such exchange coupling should be performed via first principle methods for the specific materials considered [137, 138], and could ultimately be controlled with pressure [139, 140]. For our phenomenology, a change in the exchange coupling just drifts the physics towards bigger or smaller angles, yet without qualitatively changing the overall behav-

ior [141]. Second, when exchange proximity is considered, the exchange proximity must be smaller than the intra-layer exchange to not perturb the QSL ground state. Third, in order to tilt the direction of the magnets by an external magnetic field, yet without breaking the QSL ground state, a soft magnetic axis is preferred. As a reference, taking $CrBr_3$ as the ferromagnet, the anisotropy energy can be overcome with a magnetic field of around 1 T [142], whose Zeeman energy scale of 0.04 meV is not expected to perturb QSL with exchange constants on the order of 5 meV. The application of a magnetic field is also expected to affect the magnons of the ferromagnetic encapsulation, yet those states will contribute with a uniform background to the d^2I/dV^2 signal that can be substracted [130, 143]. Finally, although our analysis has focused on a Dirac QSL, analogous calculations can be performed with other QSL ground states, such as the gaped QSL of $RuCl_3$ [28].

2.3.4 Summary

We explored the effect of twist engineering on the U(1) Dirac QSL at the mean-field level, where we see the emergence of spinon flat bands in a similar manner to TBG, and a topological gap opening in the spinon band structure. The spinon band structure exhibits high magnetic tunability, allowing for the detection of them in a magnetic heterostructure with STM. This further allows for the identification of the U(1) Dirac QSL state.

2.4 Coulomb engineered QSL

Coulomb engineering [144–146] refers to a strategy to tailor many-body interactions by means of dielectric environments, which is particularly efficient for low-dimensional materials. This is due to the pronounced role of non-local Coulomb interactions, which decisively define many-body properties in low-dimensional systems and which can be simultaneously efficiently externally modified. In this way band gaps [146–152] as well as excitonic [146, 151, 153] or plasmonic [154, 155] excitations and even topological properties [156] can be precisely tailored in 2D and 1D systems with the help of (structured) dielectric substrates. Furthermore, Coulomb interactions also play a crucial role in magnetic van der Waals materials, affecting the magnetic exchange between localized magnetic moments. This motivates us to investigate the effect of Coulomb engineering on

1T-TaS_2, aiming to drive it towards the U(1) Dirac QSL state.[6]

2.4.1 Effective model for 1T-TaS_2

To illustrate the effect of Coulomb interactions on the magnetic properties of 1T-TaS_2, we start from a single Wannier orbital model including long-range electronic interactions:

$$\begin{aligned} H = &\sum_{i,j,\sigma} t_{ij} c^\dagger_{i,\sigma} c_{j,\sigma} + U \sum_i n_{i,\uparrow} n_{i,\downarrow} \\ &+ \sum_{i,j,\sigma,\sigma'} \frac{V_{ij}}{2} n_{i,\sigma} n_{j,\sigma'}, \end{aligned} \tag{2.24}$$

where σ and σ' are spin indices, and $n_{i,\sigma} = c^\dagger_{i,\sigma} c_{i,\sigma}$. The first term describes the narrow band at the Fermi energy in 1T-TaS_2 in the absence of Coulomb interactions, and the second and third terms are Coulomb interaction terms. The hoppings t_{ij} are fitted to DFT data [43] where we find hoppings up to the 14^{th} neighbor. The hoppings exhibit an oscillating behavior in addition to a decay with distance. This oscillating behavior stems from the nature of the Wannier wavefunctions of this material, and is inherited from the electronic structure from first principles calculations.

Since there is no ab initio information about the Coulomb interactions, we study generic situations where the onsite-Coulomb U is a few 100meV. For simplicity we adopt the functional form of a modified Yukawa potential to capture the long-range Coulomb interactions

$$V_{ij} = \frac{U}{\sqrt{1 + \left(\frac{4\pi\varepsilon_0 U r_{ij}}{e^2}\right)^2}} e^{-r_{ij}/r_{\text{TF}}}, \tag{2.25}$$

where U is the on-site Coulomb interaction and r_{ij} the distance between sites i and j. The included Ohno potential [152, 157] results in a r^{-1} long-wavelength behavior, which is further suppressed by the exponential term controlled by an effective screening length r_{TF}. This way, the non-local Coulomb interaction is fully parameterized by the local interaction U and the screening length r_{TF}. It is worth noting that environmental screening to layered materials, such as resulting from dielectric substrates, is strongly non-local [144, 145, 158] such that long-ranged interactions V_{ij} are stronger reduced than the local one U. To fully characterize this model we, however, treat U and r_{TF} as independent parameters in the

[6] Part of this chapter is adapted from G. Chen, M. Rösner and J. L. Lado, J. Phys.: Condens. Matter 34 (2022) 485805.

following, understanding that any environmental screening will reduce both simultaneously.

2.4.2 Coulomb-dependent Heisenberg model

The interacting model of Eq. (2.24) is analyzed in two steps. In the limit $U \gg V_{ij}$, we can first integrate out the long-range interactions V_{ij}, leading to a renormalized dispersion for the low-energy band [159, 160]. The resulting Hamiltonian $\tilde{H}$ takes the form

$$\tilde{H} = \sum_{i,j,\sigma} \tilde{t}_{ij} c^{\dagger}_{i,\sigma} c_{j,\sigma} + U \sum_{i} n_{i,\uparrow} n_{i,\downarrow}, \tag{2.26}$$

where $\tilde{t}_{ij}$ are the renormalized hoppings derived from Eq. (2.24) using a Hatree-Fock variational wavefunction enforcing time-reversal symmetry.

For U between 100 and 500 meV as estimated for 1T metallic TMDs [43, 161, 162] and several choices of r_{TF}, the corresponding long-range Coulomb interactions V_n and renormalized hoppings $\tilde{t}_n$ are shown in Figs. 2.12(a,b), where V_n denotes n_{th} neighbor Coulomb interaction and similarly for $\tilde{t}_n$. We see that V_n is increased by increasing U and r_{TF}, which mostly affects $\tilde{t}_1$ for $r_{\text{TF}} < a$ (a is the CDW lattice constant), while the long-range interaction with $r_{\text{TF}} = a$ also modulates hoppings up to $\tilde{t}_5$. The renormalized hoppings result in a renormalized band structure as shown in Figs. 2.12(c-f). As maintaining the Mott regime requires that the bandwidth renormalization should not be too large, we focus on $r_{\text{TF}} \leq 0.4a$ in the following.

We then analyze the Hamiltonian Eq. (2.26) in the strong coupling limit, i.e. $U \gg \tilde{t}_{ij}$, using the Schrieffer-Wolf transformation, leading to an effective model for spin-degrees of freedom:

$$\mathcal{H} = \sum_{i,j} J_{ij} \mathbf{S}_i \cdot \mathbf{S}_j, \tag{2.27}$$

with $J_{ij} = 2\frac{\tilde{t}_{ij}^2}{U}$. Due to the renormalization of t_{ij} by V_{ij}, the magnetic superexchange interactions J_{ij} are controlled by changes to U and r_{TF} as well. In particular, we show in Fig. 2.13(a) the renormalized n^{th} neighbor exchange J_n. We see that J_1 exhibits a strong dependence on U and r_{TF}, stemming from the significant renormalization of $\tilde{t}_1$. In Fig. 2.13(b) we depict the full U and r_{TF} dependencies of J_1 in units of $J_1^0 = 0.1$meV, where J_1^0 is the typical magnitude of J_1 in our regime. The model of Eq. (2.27) thus realizes a long-range Heisenberg model with tunable spin exchange controlled by the local and non-local Coulomb interactions.

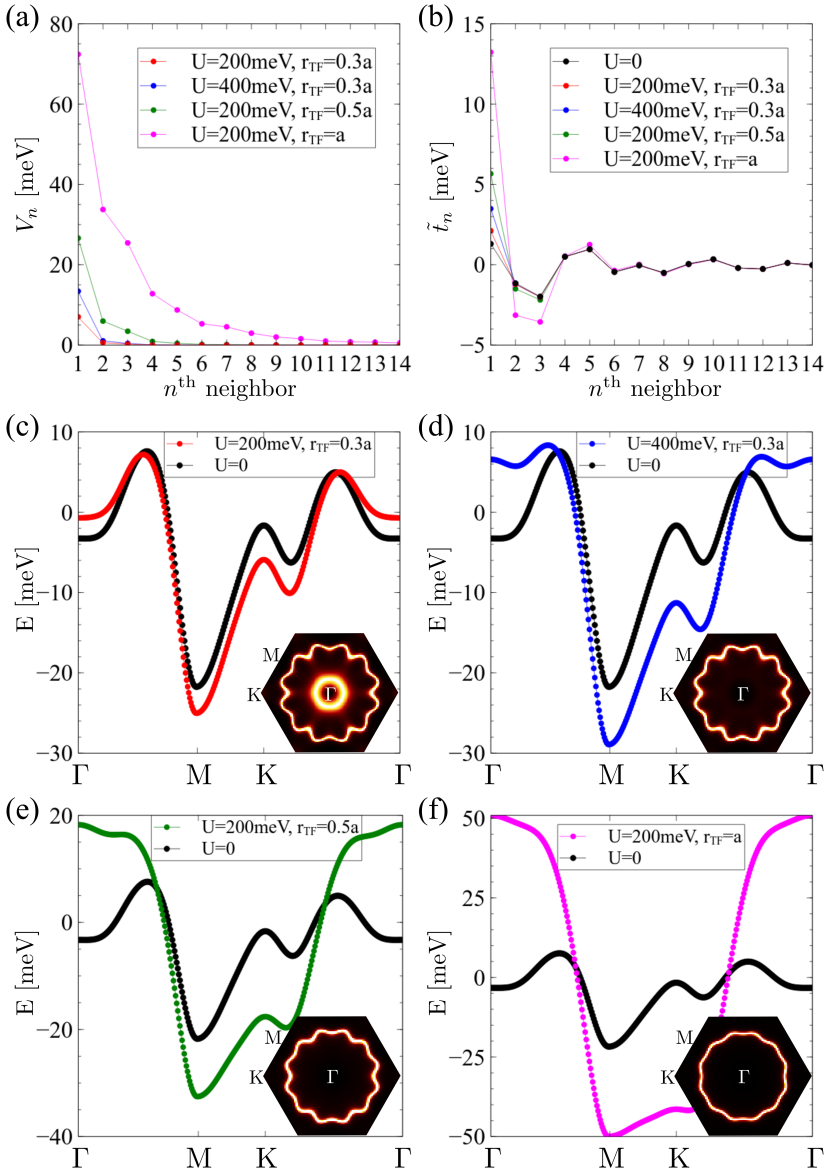

Figure 2.12. (a) Long-range Coulomb interactions V_n and (b) the corresponding renormalized hoppings $\tilde{t}_n$ for different values of parameters U and r_{TF}. (c-f) band structure renormalization for different values of U and r_{TF} in (a). The color matches the color used in (a). The insets show the corresponding Fermi surfaces for the renormalized bands.

2.4.3 Coulomb-dependent magnetic frustration

A full calculation of the phase diagram of Eq. (2.27) would require exactly solving the two-dimensional quantum many-body model, which is computationally challenging. We will thus focus on finding the regime where magnetic frustration is strong, as a QSL phase is more probable in such a

regime. A frustrated magnetic system has competing magnetic exchange interactions whose energies cannot be simultaneously minimized by any magnetic configuration [163]. As a consequence, classical magnetic ground states of a frustrated magnetic system exhibit a high degree of degeneracy, preventing the system from magnetic ordering and promoting a QSL state. We may thus characterize the frustration of a magnetic system by the degeneracy of classical magnetic ground states. We consider different non-collinear magnetic configurations characterized by a vector $\mathbf{q}$ [164,165] and compute their energy $\omega(\mathbf{q})$ from the extended Hubbard model Eq. (2.24). The resulting $\omega(\mathbf{q})$ is then shifted and scaled: $\tilde{\omega}(\mathbf{q}) = (\omega(\mathbf{q}) - \omega_0)/(\omega_1 - \omega_0)$ with $\omega_0 = \min(\omega(\mathbf{q}))$ and $\omega_1 = \max(\omega(\mathbf{q}))$. The shifted ground state energy is 0, and the scaling allows comparison between systems with different magnitudes of magnetic exchange interactions. Finally, the degeneracy of the states at a given shifted and scaled energy ω can be given by

$$\tilde{\rho}(\omega) = \int_{\mathbf{q}\in \mathrm{BZ}} \frac{\mathrm{d}^2\mathbf{q}}{(2\pi)^2} \delta(\tilde{\omega}(\mathbf{q}) - \omega). \tag{2.28}$$

In particular, $\tilde{\rho}(0)$ characterizes the ground state degeneracy of a magnetic system, and a more frustrated system is characterized by larger $\tilde{\rho}(0)$.

The computation of $\tilde{\rho}(\omega)$ is done self-consistently [166] for our model with different U and r_{TF}. We find a curve in the parameter space where $\tilde{\rho}(0)$ takes larger values than at other places (Fig.2.13(c)). Below this curve, $\tilde{\omega}(\mathbf{q})$ exhibits a minima between Γ and K (Fig.2.13(e)). As we approach this curve, J_1 increases, lowering $\tilde{\omega}(\mathbf{q})$ around $\mathbf{q} = \mathrm{K}$, eventually this results in an almost flat dispersion of $\tilde{\omega}(\mathbf{q})$ in the region between Γ and K. Above this curve, J_1 further increases and starts to dominate other exchanges. This results in the stabilization of the helical spiral state with $\mathbf{q} = \mathrm{K}$, where $\tilde{\omega}(\mathbf{q})$ takes its minimum. We have thus found that by tuning the substrate-screening of 1T-TaS_2, we can enhance the magnetic frustration and make the QSL ground state more favorable.

We note that the extended Hubbard model Eq. (2.24) and the Heisenberg model Eq. (2.27) consider only superexchange couplings stemming from the local repulsion. Apart from that, it is important to note that direct exchange stemming from the overlap of Wannier centers would also appear in the effective Heisenberg model [43, 167]. To account for this, we now include the direct exchange term $J_{\mathrm{DX}} \sum_{\langle i,j \rangle} \mathbf{S}_i \cdot \mathbf{S}_j$, which results from Hund's exchange interaction and can thus be assumed to be independent of the environmental screening [168]. As can be seen from Figs.2.13(d) and (f), the inclusion of this direct exchange term does not influence our main

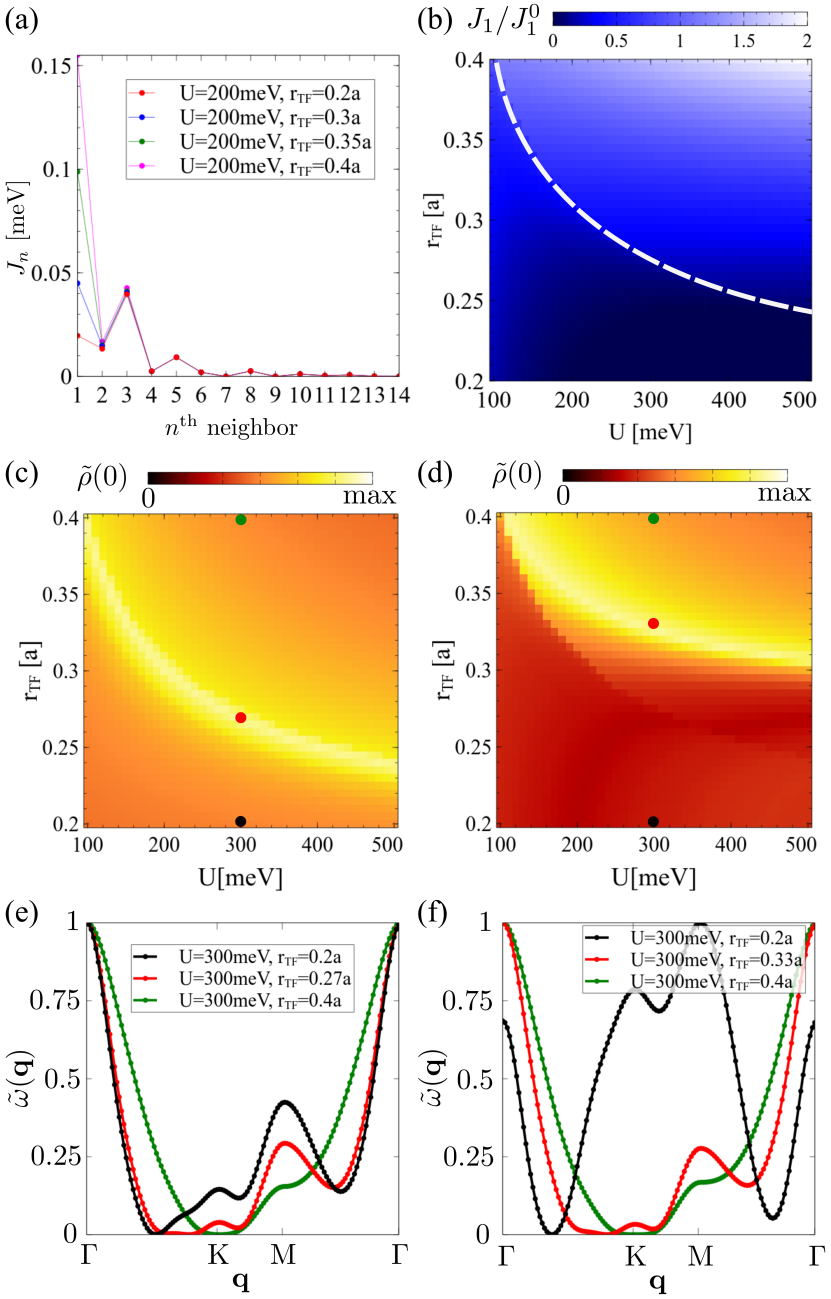

Figure 2.13. (a) Long-range spin superexchange couplings J_n for different values of U and r_{TF}. Only J_1 is significantly influenced by U and r_{TF}. (b) J_1 for different values of U and r_{TF}, in units of $J_1^0 = 0.1$meV. The dashed line indicates a discontinuity stemming from the Lifshitz transition. (c,d) Ground state degeneracy $\tilde{\rho}(0)$ for our model Eq.(2.24), as a function of U and r_{TF}. In (d) we include a direct exchange of $J_{\mathrm{DX}} = 0.5J_1^0$. (e,f) The corresponding $\tilde{\omega}(\mathbf{q})$ for the points indicated in (c,d), respectively.

result.

2.4.4 Summary

To summarize, we have shown that Coulomb engineering by modifying the substrate dielectric constant allows to tune the Coulomb interactions in a 2D strongly correlated material. In particular, for magnetic van der Waals materials such as 1T-TaS_2, this would allow to tune the spin exchange between local magnetic moments, and drive the material towards the frustrated regime where the emergence of a QSL is more probable.

2.5 Summary

1T-TaS_2 is a magnetic van der Waals material potentially hosting the U(1) Dirac QSL state. Owing to its 2D nature, it can be engineered in versatile ways. In particular, we have shown that impurity engineering allows for the identification of the QSL state in 1T-TaS_2, highlighting the emergence of spinon flat bands. Nevertheless, twist engineering also allows for the potential identification of QSL, featuring the magnetically tunable moire spinon dispersion. Finally, Coulomb engineering would allow tuning the spin exchange in 1T-TaS_2, and driving it toward the QSL regime. This chapter highlights how the versatility of magnetic van der Waals materials allows to overcome the experimental challenges in the realization and identification of an exotic phase of matter–the QSL, via engineering the properties of the magnetic van der Waals material. In the next chapter, we will explore how magnetic van der Waals materials can be used to engineer the properties of other materials, with a particular motivation for designing exotic phases of matter.

3. Designing exotic phases of matter with magnetic van der Waals materials

In the previous chapter, we have shown how the versatility of the magnetic van der Waals material 1T-TaS_2 allows for engineering and identifying the potential U(1) Dirac QSL state. In this chapter, we show another aspect: the versatility of magnetic 2D materials also allows for engineering the properties of other 2D materials with them. This can be particularly useful for designing exotic phases of matter [169] hard to find in natural compounds or to be realized in other materials. In particular, we focus on heterostructures between 2D magnets and other 2D materials, where we aim to design helical states and heavy fermions. The helical states are an essential ingredient for designing topological superconductivity. The heavy-fermion systems have their particular theoretical interest and are related to unconventional superconductivity.

Topological superconductivity represents one of the most fascinating topics in condensed matter. One particular reason is they are known to host Majorana fermions [28] that can be used for topological quantum computation [170, 171]. Despite the large interest in topological superconductivity, natural compounds hosting topological superconductivity have been relatively sparse [172–179]. This has motivated for the search for topological superconductivity in artificially designed systems [180–183]. In particular, a recipe for topological superconductivity is a combination of (i) s-wave pairing and (ii) helical edge states. Thus, designing helical states would be of critical interest to designing topological superconductivity. It is known that helical states can arise in a spinful electronic system in the presence of Rashba spin-orbit coupling (SOC) and magnetism [184, 185]. Yet, large spin-orbit coupling is rarely present in natural compounds. Interestingly, recently raised 2D magnet NiI_2 [186] hosts an exotic helimagnetic order that can induce an effective Rashba SOC and magnetic field. This motivates us to investigate how these helimagnets can be utilized to de-

sign helical states. In particular when they are in proximity to a strongly correlated material with superconducting instability such as TBG.

Heavy-fermion systems are exotic phases of matter where the effective mass of dispersive fermions (usually electrons) gets massively enhanced due to Kondo coupling to a lattice of magnetic moments [176, 187–190]. Interest in heavy-fermion systems stems from (i) the quantum critical point between the heavy-fermion and the magnetically ordered phase and (ii) the realization of unconventional topological superconductivity in these systems [173, 174, 176, 190–195]. The coexistence of (i) local magnetic moments which require strong localization and (ii) dispersive electrons makes natural heavy-fermion compounds to be relatively rare. This motivates the search for heavy-fermions in artificially designed systems [196]. In this line, magnetic 2D materials offer a versatile platform to realize the lattice of localized moments, and the dispersive electrons can be found in 2D conductors. The Kondo coupling can be realized by stacking the two different 2D materials together. We will show how this design is realized in a 1T/1H-TaS_2 heterostructure [40].

The rest of this chapter is organized as follows: in Sec.3.1 we illustrate the physics of a 2D magnet/metal heterostructure, highlighting the two interesting physical regimes in this heterostructure. In Sec.3.2 we show how a 2D helimagnet can be utilized in designing helical states in graphene and in particular in TBG. In Sec.3.3 we show how the 1T/1H-TaS_2 heterostructure can realize the heavy-fermion physics.

3.1 2D magnet/metal heterostructure

Let us first illustrate the physics in a heterostructure where a 2D magnet is stacked on top of a metal, which can be modeled as:

$$H = H_{\text{kinetic}} + \sum_{i,j} J_{ij} \mathbf{S}_i \cdot \mathbf{S}_j + \sum_{i,n} \mathcal{J}_{i,n} \mathbf{S}_i \cdot \mathbf{s}_n. \tag{3.1}$$

The first term of Eq. (3.1) describes the kinetic energy of electrons in the metal. The second term describes the spin exchange couplings between local magnetic moments in the 2D magnet, where $\mathbf{S}_i$ is the magnetic moment at site i. The third term describes the coupling between the local magnetic moments and the electrons, with $\mathbf{s}_n = c^\dagger_{n,\alpha} \boldsymbol{\sigma}_{\alpha\beta} c_{n,\beta}$ where $c^\dagger_{n,\alpha}$ is the electron creation operator at site n with spin α. In general this model is not solvable, yet in extreme limits approximations can be made as we illustrate below.

In the limit $J_{ij} \gg \mathcal{J}_{i,n}$, the ground state of the magnetic moments is dominated by the second term in Eq. (3.1) and we can ignore the influence of the coupling term. This allows us to replace $\mathbf{S}_i$ with its ground state expectation value given by the second term in Eq. (3.1):

$$H = H_{\text{kinetic}} + \sum_n \mathbf{B}_n \cdot \mathbf{s}_n. \tag{3.2}$$

where $\mathbf{B}_n = \sum_i \mathcal{J}_{i,n} \langle \mathbf{S}_i \rangle$ is the effective local magnetic field the electron at site n feel due to coupling to the magnet. We see that in this limit, the magnet induces a local magnetic field on the metal, that is dependent on the local magnetization $\langle \mathbf{S}_i \rangle$ in the ground state.

In the opposite limit $J_{ij} \ll \mathcal{J}_{i,n}$, the dynamics of the magnetic moments are dominated by the third term in Eq. (3.1) and we thus neglect the perturbations from the second term, giving rise to:

$$H = H_{\text{kinetic}} + \sum_{i,n} \mathcal{J}_{i,n} \mathbf{S}_i \cdot \mathbf{s}_n. \tag{3.3}$$

Assuming that the magnetic moments are aligned with the electronic sites, and that the coupling is local $\mathcal{J}_{i,n} = J_K \delta_{in}$, Eq. (3.3) becomes the standard form of the Kondo lattice model [197]:

$$H = H_{\text{kinetic}} + J_K \sum_i \mathbf{S}_i \cdot c^\dagger_{i,\alpha} \boldsymbol{\sigma}_{\alpha\beta} c_{i,\beta}. \tag{3.4}$$

We see that magnetic 2D materials can be utilized to generate a local magnetic field or induce the Kondo lattice model on a metal in different regimes. We will see in the next sections how these allow to promote unconventional superconductivity and heavy fermions, respectively.

3.2 Helical states with proximity helimagnetic field

In this section we show how recently raised helimagnets such as NiI_2 [186] can be utilized to engineer unconventional superconductivity when proxitimized to other van der Waals materials. Helimagnets are magnetic materials with a spatially-dependent magnetization in the ground state. An example of helimagnetic magnetization is the spin-spiral state in Fig.2.1(c). The key observation is that the spatially-dependent magnetization of the helimagnet will induce a spatially-dependent magnetic field, which acts effectively as a Rashba SOC and a magnetic field. We illustrate the physics of this in Sec.3.2.1 with a helimagnet in proximity to graphene. We then show how magnetic encapsulation, a method we have used to manipulate

spinon states in Sec.2.3, would affect superconducting instabilities in TBG with helimagnets.

3.2.1 Helimagnetic field on graphene

Before we investigate the band structure of helimagnetically encapsulated TBG, it is first illustrative to look at the band structure of a single-layer graphene in proximity to a helimagnet. The Hamiltonian of this heterostructure reads:

$$H = t\sum_{\langle i,j\rangle}(c_i^\dagger c_j + h.c.) + J\sum_i\sum_{\alpha,\beta}\mathbf{M}(i)\cdot\boldsymbol{\sigma}_{\alpha\beta}c_{i,\alpha}^\dagger c_{i,\beta} \tag{3.5}$$

where the first term is the Hamiltonian of graphene (Eq. (2.6)), J is the coupling between the helimagnet and graphene, and $\mathbf{M}(i)$ is the magnetization of the helimagnet around site i. We note that the above Hamiltonian requires the intra-layer spin exchange in the helimagnet to be much larger than the inter-layer coupling J, such that the helimagnetic order remains in the presence of the coupling. When the opposite happens, the system will become a Kondo lattice system as we see in Sec.3.1. In addition, we have assumed the lattice constant of the helimagnet is not much larger than the atomic spacing (between two nearest carbon atoms) in graphene. As a reference, NiI_2 has a lattice constant of 3.95Å, and the atomic spacing in graphene is 1.42Å. Let's assume that the local magnetization in the helimagnet has the following spatial dependence:

$$\mathbf{M}(i) = M_0(\cos(\mathbf{q}\cdot\mathbf{R}_i), \sin(\mathbf{q}\cdot\mathbf{R}_i), 0), \tag{3.6}$$

that is, the magnetization is in-plane and rotates in real space with a characteristic wavevector $\mathbf{q}$. The magnetization in NiI_2 satisfy this dependence, where the wavevector $\mathbf{q}$ has a norm of $1/(7\times 3.95)\text{Å}^{-1} \approx 0.036\text{Å}^{-1}$ [198]. With this spatial dependence, Eq. (3.5) reduces to graphene coupled to an external helimagnetic field:

$$H = t\sum_{\langle i,j\rangle}(c_i^\dagger c_j + h.c.) + \sum_i\sum_{\alpha,\beta}\mathbf{B}(i)\cdot\boldsymbol{\sigma}_{\alpha\beta}c_{i,\alpha}^\dagger c_{i,\beta} \tag{3.7}$$

where

$$\mathbf{B}(i) = B_0(\cos(\mathbf{q}\cdot\mathbf{R}_i), \sin(\mathbf{q}\cdot\mathbf{R}_i), 0), \tag{3.8}$$

where $B_0 = JM_0$ is the magnitude of the effective magnetic field on site i.

We now solve Eq. (3.7), considering the generic case that the effective magnetic field is incommensurate with the lattice of graphene. In this

case, translational symmetry is broken and we cannot utilize Bloch's theorem. To restore the translational symmetry, we would like to go to the rotating frame, by performing the following unitary transformation to Eq. (3.7) [164, 199, 200]:

$$U = \bigoplus_j U_j \tag{3.9}$$

where

$$U_j = e^{-\frac{i}{2}\mathbf{q}\cdot\mathbf{R}_j\sigma_z} = \begin{pmatrix} e^{-\frac{i}{2}\mathbf{q}\cdot\mathbf{R}_j} & 0 \\ 0 & e^{\frac{i}{2}\mathbf{q}\cdot\mathbf{R}_j} \end{pmatrix}. \tag{3.10}$$

The Hamiltonian in the rotating frame is

$$H' = U^\dagger H U = \sum_{\langle i,j\rangle}\sum_{\alpha,\beta} t e^{i\theta(i,j)(\sigma_z)_{\alpha\beta}} c^\dagger_{i,\alpha} c_{j,\beta} + B_0 \sum_i \sum_{\alpha,\beta} c^\dagger_{i,\alpha}(\sigma_x)_{\alpha\beta} c_{i,\beta} \tag{3.11}$$

where $\theta(i,j) = \frac{1}{2}\mathbf{q}\cdot(\mathbf{R}_i - \mathbf{R}_j)$. The Hamiltonian H' has the translational symmetry of the single-layer graphene. We see that in the rotating frame, the effect of the helimagnetic field is transformed into a uniform magnetic field and a spin-dependent phase shift. Since unitary transformations maintain the eigenvalues, the band structure of H' reflects the band structure of H in Eq. (3.7). In addition, since σ_z is invariant under the unitary transformation Eq. (3.9), the expectation value of σ_z computed in the rotating frame is the same as that in the original frame.

We start with the case when $\mathbf{q}$ is small: $\mathbf{q} \ll (\mathbf{b}_1 - \mathbf{b}_2)$ where $\mathbf{b}_{1,2}$ are reciprocal vectors of graphene. NiI_2 on graphene would fall into this regime. When the effective magnetic field $B_0 = 0$, the rotating frame Hamiltonian just shifts the band structure of spin-up/down electrons by a momentum of $\pm\mathbf{q}/2$ (Fig.3.1(a)). As we switch on the magnetic field, different spin channels start to hybridize. In particular, a gap opening due to hybridization happens at Γ and M points (Fig.3.1(b)). Due to this gap opening, the bandwidth of the middle two bands reduces, whereas the bandwidth of the other two bands increases. The hybridization gets stronger for larger B_0 (Fig.3.1(c)), but gets weaker for larger $\mathbf{q}$ (Fig.3.1(d)). However, the bandwidth depends mainly on B_0 and is not sensitive to $\mathbf{q}$ in this regime. We observe two main effects of the helimagnetic field on the band structure of graphene: (i) it results in a hybridization between originally degenerate spin channels, giving rise to bands with spin texture and (ii) due to the hybridization, the degeneracies at Time-Reversal-Invarant-Momenta (TRIM) Γ and M are lifted. An important consequence of (ii) is that when

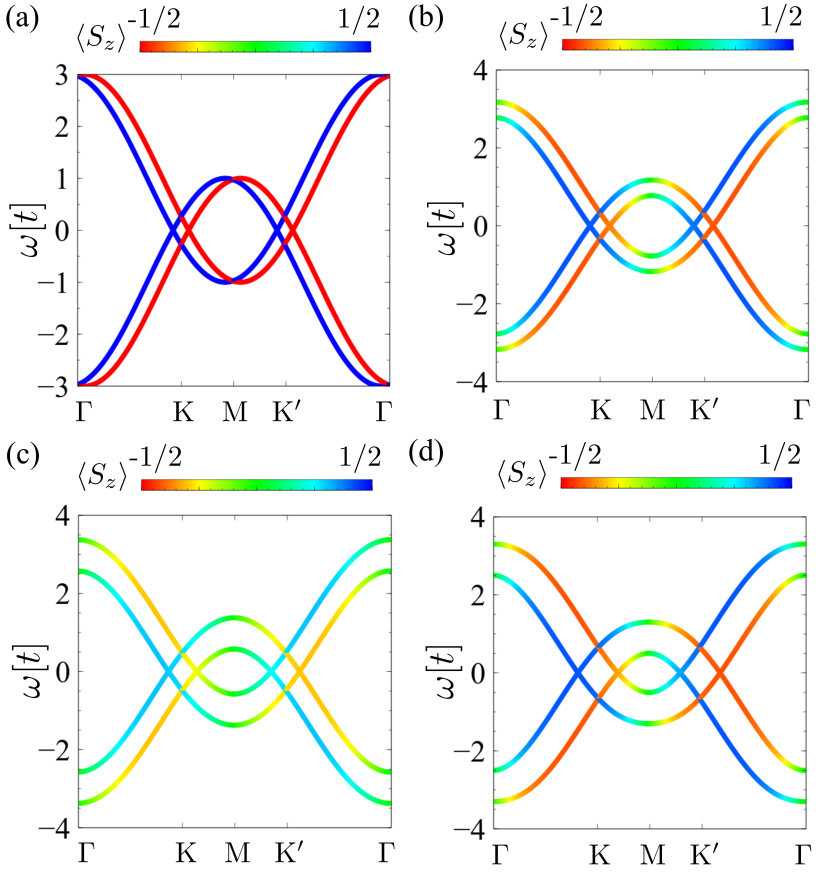

Figure 3.1. band structure of graphene in proximity to a helimagnet in the rotating frame Eq. (3.11) with $\mathbf{q} = 0.05(\mathbf{b}_1 - \mathbf{b}_2)$ in panels (a-c) and $\mathbf{q} = 0.1(\mathbf{b}_1 - \mathbf{b}_2)$ in panel (d), where $\mathbf{b}_{1,2}$ are reciprocal vectors of graphene. $B_0 = 0$ in (a), $B_0 = 0.2t$ in (b) and $B_0 = 0.4t$ in (c) and (d)

the Fermi surface lies inside the induced gap at Γ, we would have helical states, the essential ingredient for topological superconductivity.

Let us now focus on a particular point in the above band structures, the band crossings at K and K′ points. It can be seen that at large field the spin states hybridize at these points in Fig.3.1(c). However, unlike the hybridization in Γ and M points, this hybridization does not open a gap. This is due to the π Berry phase difference between the two states [109] as we illustrate below. The low-energy Bloch Hamiltonian near a Dirac cone at K(K′) point can be obtained using the $k \cdot p$ model:

$$H_{k\cdot p}\left(\mathrm{K}(\mathrm{K}') + \mathbf{p}\right) = \begin{pmatrix} 0 & |\mathbf{p}|e^{-i\phi(\mathbf{p})} \\ |\mathbf{p}|e^{i\phi(\mathbf{p})} & 0 \end{pmatrix}. \tag{3.12}$$

where $\phi(\mathbf{p}) = \arg(p_y/p_x)$ for K and $\phi(\mathbf{p}) = \pi + \arg(-p_y/p_x)$ for K′ is the

Berry phase. The eigenstates for the $k \cdot p$ Hamiltonian Eq.(3.12) are

$$|u_{\pm}\rangle = \frac{1}{2}\begin{pmatrix} \pm e^{-i\phi(\mathbf{p})} \\ 1 \end{pmatrix} \tag{3.13}$$

with $E_{\pm} = \pm|\mathbf{p}|$. Within the same Dirac cone, the Berry phase difference between $\mathbf{p}$ and $-\mathbf{p}$ is π. In such a case, the eigenstates are orthogonal:

$$\langle u_{\pm}(\mathbf{p})|u_{\pm}(-\mathbf{p})\rangle = 0. \tag{3.14}$$

Now, let us turn to the Bloch Hamiltonian of H' at K point, and utilize the $k \cdot p$ Hamiltonian for the spin-up/down channels:

$$\begin{aligned} H'(\mathbf{K}) &= H_0 + H_{int} \\ &= \begin{pmatrix} H_{k\cdot p}\left(\mathbf{K} + \frac{\mathbf{q}}{2}\right) & \\ & H_{k\cdot p}\left(\mathbf{K} - \frac{\mathbf{q}}{2}\right) \end{pmatrix} + \begin{pmatrix} & B_0 \cdot \mathbf{I} \\ B_0 \cdot \mathbf{I} & \end{pmatrix} \end{aligned} \tag{3.15}$$

where $\mathbf{I}$ is the identity matrix, stemming from the sublattice symmetry in the second term of Eq. (3.11). We can diagonalize Eq. (3.15) to see that the second term does not result in splitting. Alternatively, by noting that $\langle u_{\pm}(\mathbf{p})|B_0 \cdot \mathbf{I}|u_{\pm}(-\mathbf{p})\rangle = 0$, we can understand the zero splitting from the perturbation theory point of view.

We now switch to discuss another case where $\mathbf{q}$ is close to $(\mathbf{b}_1 - \mathbf{b}_2)/3$, which brings the two Dirac points originally from K and K′ close to each other (Fig.3.2(a)). We see that now a finite B_0 results in splitting at M point, since the Berry phase difference between these Dirac cones is no longer π (Fig.3.2(b)). Furthermore, the Dirac cones get split at large B_0 (Fig.3.2(c,d)). Similar to the small $\mathbf{q}$ case, we see spin-texture and band splitting at Γ and M. The difference is now the hybridization mainly takes place near Γ and M, as at other momenta the two spin channels are far in energy.

The helical states resulting from spin hybridization and band-splitting effects by a helimagnet in proximity to graphene motivate us to look at how this would affect the properties of TBG. In particular, We would like to see if helical states can be engineered in TBG with helimagnetic encapsulation. As these together with the superconducting instability of TBG can give rise to topological superconductivity.

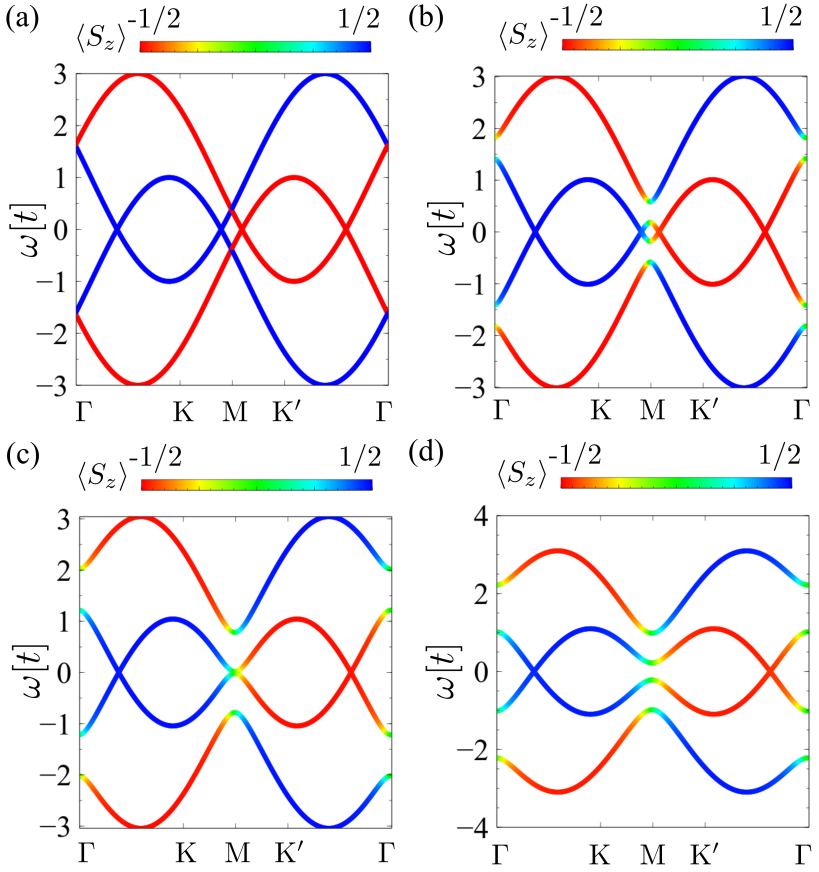

Figure 3.2. band structure of graphene in proximity to a helimagnet in the rotating frame Eq. (3.11) with $\mathbf{q} = 0.4(\mathbf{b}_1 - \mathbf{b}_2)$ and $B_0 = 0$ in (a), $B_0 = 0.2t$ in (b), $B_0 = 0.4t$ in (c) and $B_0 = 0.6t$ in (d).

3.2.2 Helimagnetic encapsulation on TBG

We now switch to consider the effect of helimagnetic encapsulation on TBG.[1] We consider twisted bilayer graphene at a twist angle $1.44°$, slightly above the flat band regime [88, 89, 141]. In this regime, the electronic structure of TBG shows strongly renormalized Dirac cones [141] and isolated moire energy bands [88, 89]. We consider TBG encapsulated between helimagnets with in-plane magnetization as shown in Fig. 3.3(a). Such heterostructure is expected to be stable as graphene shows stability for a large variety of substrates, including hBN [201, 202] WSe_2 [203, 204], and the magnetic insulator CrI_3 [205]. The impact of the helimagnet encapsulation is accounted for by integrating out the degrees of freedom of the

[1]Part of this section is adapted from G. Chen, M. Khosravian, J. L. Lado and A. Ramires, 2D Mater. 9 (2022) 024002.

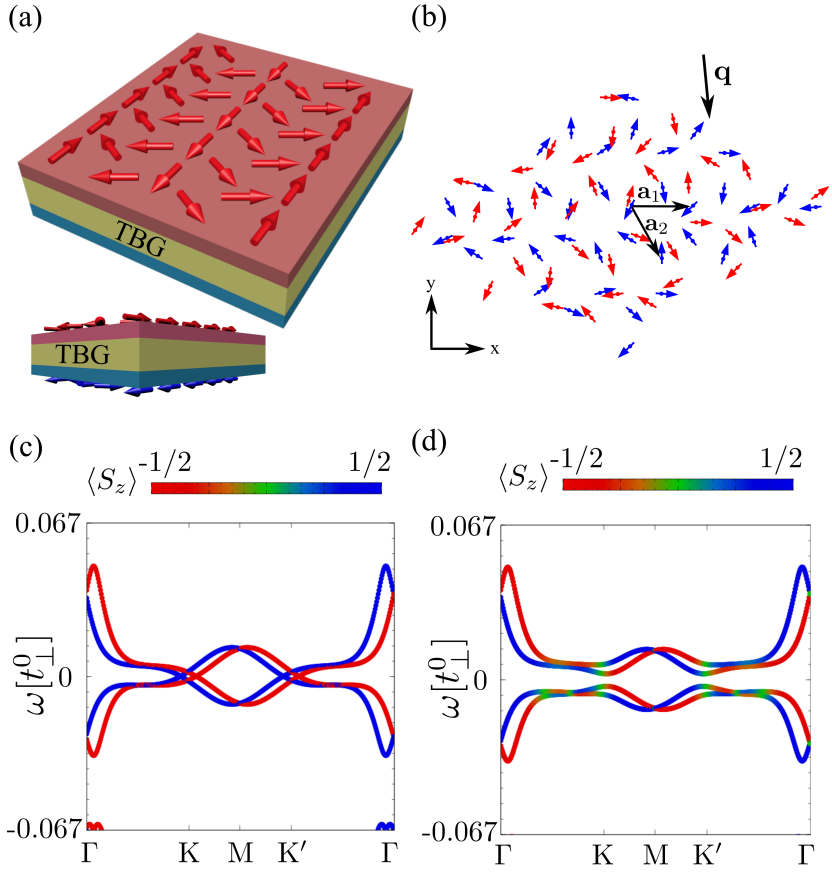

Figure 3.3. (a) Sketch of TBG encapsulated with helimagnets, viewed from top and side. (b) Local effective exchange field induced by proximity to helimagnets on top (red) and bottom (blue) layers of TBG. The direction of characteristic vector of the helimagnets $\mathbf{q}$ is denoted with the black arrow. (c) Band structure of the heterostructure described by Eq. (3.20) with $J_0 = 0$ and $\mathbf{q} = 0.05(\mathbf{b}_1 - \mathbf{b}_2)$. (d) Band structure of the heterostructure with $J_0 = 0.033t_\perp^0$, $\theta_0 = \pi$ and $\mathbf{q} = 0.05(\mathbf{b}_1 - \mathbf{b}_2)$. We took twist angle $1.44°$ for (c), (d).

helimagnets, leading to an effective exchange field in the twisted graphene bilayer, in a similar manner to what we did for single-layer graphene in the last section. The effective Hamiltonian of the proximitized multilayer takes the form

$$\begin{aligned} H = &\sum_l \sum_{\langle i,j \rangle} \sum_\alpha t c^\dagger_{i,\alpha,l} c_{j,\alpha,l} \\ &+ \sum_{l \neq l'} \sum_{i,j} \sum_\alpha t_\perp(i,j) c^\dagger_{i,\alpha,l} c_{j,\alpha,l'} \\ &+ J \sum_l \sum_i \sum_{\alpha,\beta} \mathbf{M}_l(i) \cdot \boldsymbol{\sigma}_{\alpha\beta} c^\dagger_{i,\alpha,l} c_{i,\beta,l} \end{aligned} \tag{3.16}$$

where $l = 1, 2$ is the layer index, i, j are site indexes, and α, β are spin indexes. t and $t_\perp$ are intra- and inter-layer hopping in TBG, $\langle i, j \rangle$ restricts the sum to nearest neighbours in the first term. The interlayer hopping takes the form $t_\perp(i,j) = t_\perp^0 \frac{(z_i - z_j)^2}{|\mathbf{r}_i - \mathbf{r}_j|^2} e^{-\xi(|\mathbf{r}_i - \mathbf{r}_j| - d)}$ [88, 105], where d is the distance between layers and ξ parameterizes the decay of the interlayer hopping[2]. J is the exchange coupling between the TBG and the helimagnets, $\mathbf{M}_l(i)$ is the magnetization around site i in the lth layer, and $\boldsymbol{\sigma}$ is a vector composed of Pauli matrices.

We consider a general helimagnetic order that can be incommensurate with the graphene sublattice structure. In addition to the spatially rotating behavior in Eq. (3.6), we consider that the magnetization has a sublattice imbalance that sublattice B has a relative rotation θ_0 w.r.t. that on sublattice A

$$\begin{aligned} \mathbf{M}(i \in A) &= M_0(\cos(\mathbf{q} \cdot \mathbf{R}_i), \sin(\mathbf{q} \cdot \mathbf{R}_i), 0) \\ \mathbf{M}(i \in B) &= M_0(\cos(\mathbf{q} \cdot \mathbf{R}_i + \theta_0), \sin(\mathbf{q} \cdot \mathbf{R}_i + \theta_0), 0) \end{aligned} \tag{3.17}$$

with M_0 being the magnitude of the local magnetization, $\mathbf{q}$ being the characteristic wave vector of the helimagnet, and $\mathbf{R}_i$ being the coordinate of site i. Due to the superexchange mechanism [132], the local magnetization at top and bottom magnets are expected to align antiferromagnetically, so we consider

$$\mathbf{M}_1(i) = -\mathbf{M}_2(i) = \mathbf{M}(i). \tag{3.18}$$

For the sake of simplicity, we consider $\mathbf{q}$ parallel to $\mathbf{b}_1 - \mathbf{b}_2$, which is a high-symmetry direction of the moire Brillouin zone, with $\mathbf{b}_{1,2}$ being the reciprocal vectors of the moire superlattice. When $\theta_0 = 0$, there is no sublattice imbalance and the magnets are fully characterized by the helimagnetic order (Fig. 3.3(b)). When $\theta_0 = \pi$, the helimagnetic order is overlayed with a staggered magnetization for the sublattices.

At low energy, the influence of the helimagnetization on the band structure of TBG depends only on the effective exchange field $J_0 = JM_0$ and the ratio between the characteristic vector $\mathbf{q}$ and the moire periodicity. The moire periodicity can be tuned by the twist angle θ, which can be controlled by tear and stack fabrication [206, 207], this allows us to explore regimes with different ratios between the characteristic vector $\mathbf{q}$ and the moire periodicity. For simplicity we consider small $\mathbf{q}$ that does not result in valley hybridization. When $\mathbf{q} \sim \mathbf{b}_1 - \mathbf{b}_2$, the helimagnet does not introduce a

[2] For computational efficiency we use a re-scaling relation [106–108] with $t_\perp^0 = 0.3t$

significant change to the low-energy dispersion of TBG [165]. We thus focus on the regime when $\mathbf{q} \ll \mathbf{b}_1 - \mathbf{b}_2$, as we learn from the case of graphene that smaller $\mathbf{q}$ results in stronger hybridization in Fig.3.1.

We now solve the system by going to the rotating frame, in the same spirit as what we did in Eq. (3.9) and (3.10). We perform a local unitary transformation to the Hamiltonian such that the local magnetization is aligned along the x direction for all sites:

$$U = \prod_i e^{-\frac{i}{2}\mathbf{q}\cdot\mathbf{r}_i\sigma_{z,i}} \tag{3.19}$$

with $\sigma_{z,i}$ the spin Pauli matrix in site i. The transformed Hamiltonian becomes:

$$\begin{aligned} H' &= U^\dagger H U \\ &= \sum_l \sum_{\langle i,j\rangle} \sum_{\alpha,\beta} t e^{i\theta(i,j)(\sigma_z)_{\alpha\beta}} c^\dagger_{i,\alpha,l} c_{j,\beta,l} \\ &+ \sum_{l\neq l'} \sum_{i,j} \sum_{\alpha,\beta} t_\perp(i,j) e^{i\theta(i,j)(\sigma_z)_{\alpha\beta}} c^\dagger_{i,\alpha,l} c_{j,\beta,l'} \\ &+ J_0 \sum_l \sum_{i\in\{A\}} \sum_{\alpha,\beta} f_l c^\dagger_{i,\alpha,l} (\sigma_x)_{\alpha\beta} c_{i,\beta,l} \\ &+ J_0 \sum_l \sum_{i\in\{B\}} \sum_{\alpha,\beta} \chi f_l c^\dagger_{i,\alpha,l} (\sigma_x)_{\alpha\beta} c_{i,\beta,l} \end{aligned} \tag{3.20}$$

where $J_0 = JM_0$ is the effective local exchange field, $f_1 = -f_2 = 1$, $\theta(i,j) = \frac{1}{2}\mathbf{q}\cdot(\mathbf{R}_i - \mathbf{R}_j)$ and $\chi = \cos\theta_0 = \pm 1$ for $\theta_0 = 0, \pi$. Since the magnetization is uniform up to a sublattice imbalance in H', H' has the same periodicity as an isolated TBG. With no proximity effect, i.e. when $J_0 = 0$, the only difference between H and H' is the additional phases in the hopping terms, resulting in a momentum shift of $\pm\mathbf{q}/2$ for spin-up/down channels, respectively (Fig. 3.3(c)). We note that the additional phase in the first two terms corresponds to an artificial in-plane spin-orbit coupling, while the last two terms correspond to exchange terms. For finite J_0, both time-reversal symmetry and inversion symmetry are broken in H, and spin-mixing occurs in the quasi-flat bands, creating a spin texture (Fig. 3.3(d)). In the following we address these spin-textured quasi-flat bands for both $\theta_0 = 0$ and $\theta_0 = \pi$.

For $\theta_0 = 0$, we have a helimagnet that induces a nearly ferromagnetic exchange in neighboring sites. In this case, the band structure with $\mathbf{q} = 0.05(\mathbf{b}_1 - \mathbf{b}_2)$ and different values of J_0 is shown in Fig. 3.4(a,b). We observe that spin-splittings and anticrossings appear in the nearly

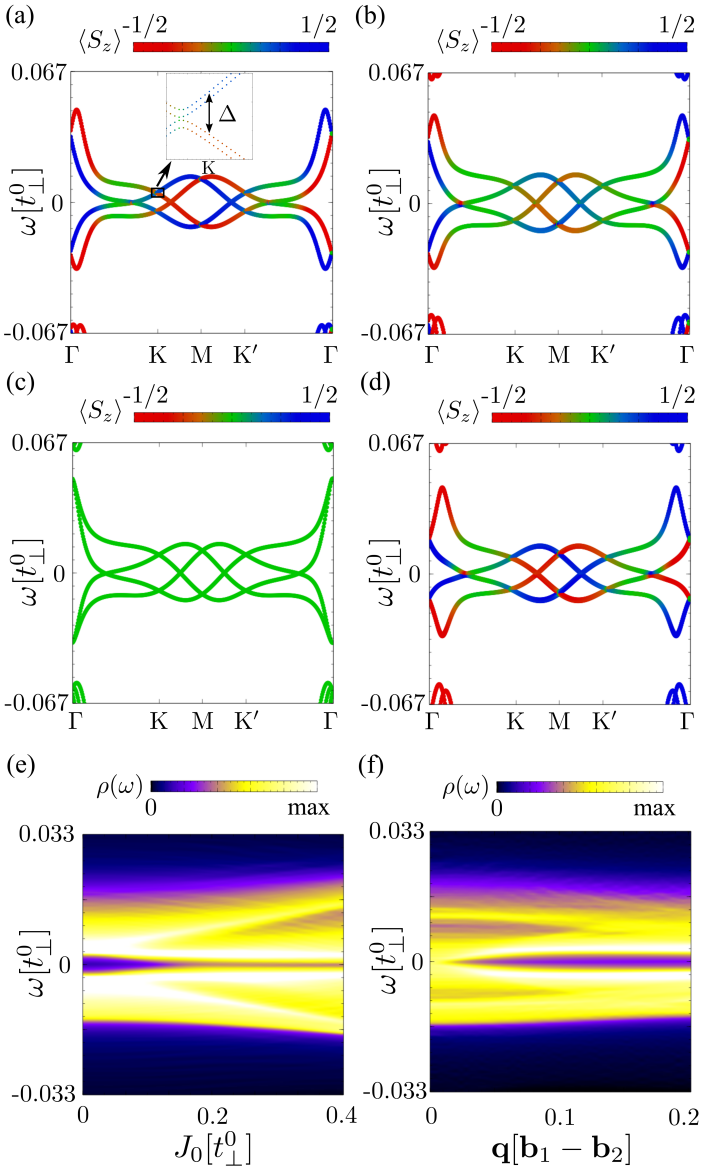

Figure 3.4. (a-d) Band structure and (e-f) DOS $\rho(\omega)$ of TBG with incommensurate helimagnetic encapsulation Eq. (3.20). The helimagnetic order, given by Eq. (3.17), has a characteristic vector $\mathbf{q}$ much smaller than the moire reciprocal vectors of TBG and $\theta_0 = 0$. We took in (a) $\mathbf{q} = 0.05(\mathbf{b}_1 - \mathbf{b}_2)$ and $J_0 = 0.067t_\perp^0$. Inset: spin-splitting Δ at K point. We took in (b) $\mathbf{q} = 0.05(\mathbf{b}_1 - \mathbf{b}_2)$ and $J_0 = 0.13t_\perp^0$, in (c) $\mathbf{q} = 0$ and $J_0 = 0.13t_\perp^0$, in (d) $\mathbf{q} = 0.1(\mathbf{b}_1 - \mathbf{b}_2)$ and $J_0 = 0.13t_\perp^0$, in (e) $\mathbf{q} = 0.05(\mathbf{b}_1 - \mathbf{b}_2)$ and in (f) $J_0 = 0.13t_\perp^0$.

flat bands. The anticrossing gap Δ at the K point as denoted in Fig. 3.4(a) exhibits a quadratic dependence on J_0, which indicates that the anticrossing is caused by a second-order contribution. The reason that the first-order contribution does not cause spin-splitting is due to the

orthogonality between the low energy eigenstates [109], similar to the explanation for Fig.3.1 in Eq. (3.14). Comparing the band structure with different $\mathbf{q}$ at $J_0 = 0.13t_\perp^0$ (Fig. 3.4(b-d)), we find that the spin texture exhibits a strong dependence on $\mathbf{q}$, whereas the dispersion does not change substantially with $\mathbf{q}$. The DOS versus J_0 and $\mathbf{q}$ (Fig. 3.4(e,f)), show that helimagnetic encapsulation does not spoil the small bandwidth of the low energy bands.

We now move on to the case when $\theta_0 = \pi$, i.e. the magnetization on the sublattices is opposite and we have a helimagnet inducing a nearly antiferromagnetic field in neighboring sites. The band structures with $\mathbf{q} = 0.05(\mathbf{b}_1 - \mathbf{b}_2)$ and different J_0 are shown in Fig. 3.5(a,b). In this regime, large anticrossings at K and K' appear, together with a simultaneous splitting of the Dirac cones. The splitting Δ' as denoted in Fig. 3.5(a) exhibits a linear dependence on J_0, indicating that the splitting stems from a first-order contribution. As a consequence of the splitting of the Dirac cones, the bands become flatter and shift away from each other as J_0 increases, which is in contrast to the case when $\theta_0 = 0$. The $\mathbf{q}$-dependence of the bands with fixed $J_0 = 0.13t_\perp^0$ is shown in Fig. 3.5(b-d). Interestingly, both the spin texture and the dispersion depend strongly on $\mathbf{q}$. The low energy DOS versus J_0 and $\mathbf{q}$ is shown in Fig. 3.5(e,f), highlighting that the nearly flat bands maintain their flatness as the system develops a strong spin texture.

We have thus seen that helimagnetical encapsulation results in spin-textured nearly flat bands in TBG. However, unlike the case for graphene, the splitting at Γ and M does not occur for helimagnetically encapsulated TBG. This is due to the existence of a combination of time-reversal with a horizontal mirror symmetry [208] in this heterostructure, and that Γ and M are invariant momenta under this symmetry. The preserved crossings at Γ and M result in multiple Fermi surfaces at finite doping, which prevents us from getting topological superconductivity from the helical states due to Kramer's degeneracy. Alternatively, if we consider $\mathbf{M}_1(i) = \mathbf{M}_2(i) = \mathbf{M}(i)$ instead of Eq. (3.18), the above symmetry will be broken. In such case, helical states with a single Fermi surface can arise at finite doping, and topological superconductivity gets promoted in this regime (Fig.3.6). Interestingly, the exchange field required to induce a sizable gap is much smaller than the inter-layer coupling of TBG, which is favorable for experimental realizations.

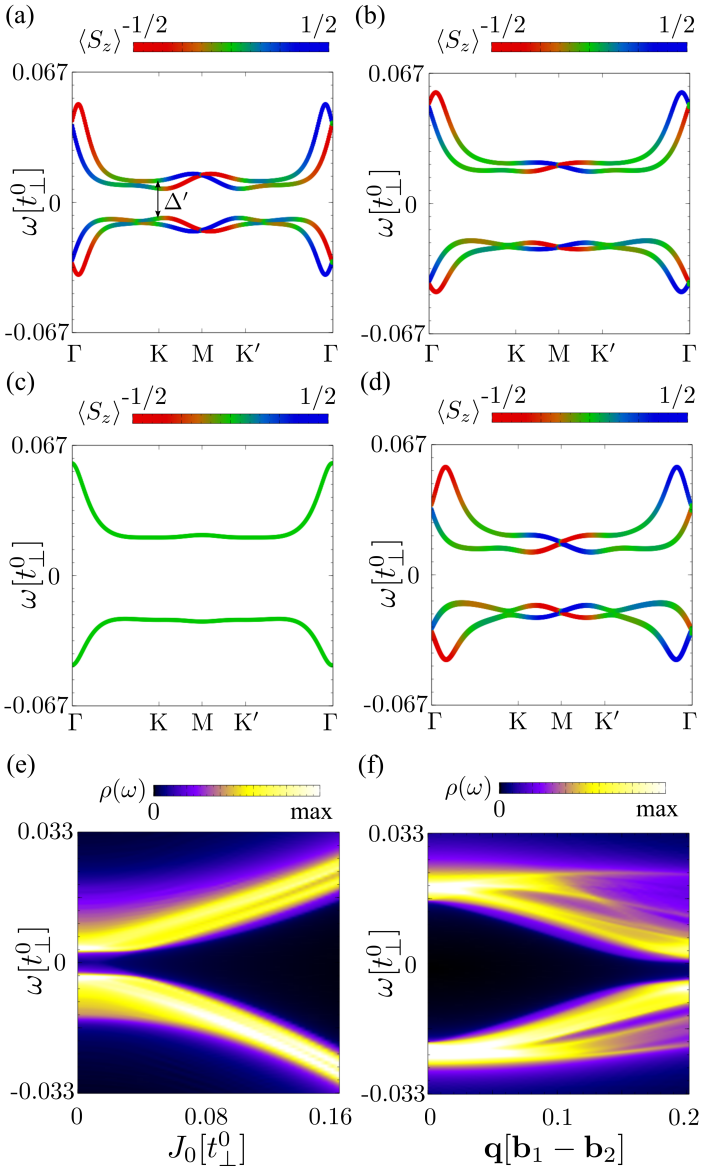

Figure 3.5. (a-d) Band structure and (e-f) DOS $\rho(\omega)$ of TBG with incommensurate helimagnetic encapsulation Eq. (3.20). The helimagnetic order, given by Eq. (3.17), has a characteristic vector $\mathbf{q}$ much smaller than the moire reciprocal vectors of TBG and $\theta_0 = \pi$. We took in (a) $\mathbf{q} = 0.05(\mathbf{b}_1 - \mathbf{b}_2)$ and $J_0 = 0.067t_\perp^0$, in (b) $\mathbf{q} = 0.05(\mathbf{b}_1 - \mathbf{b}_2)$ and $J_0 = 0.13t_\perp^0$, in (c) $\mathbf{q} = 0$ and $J_0 = 0.13t_\perp^0$, in (d) $\mathbf{q} = 0.1(\mathbf{b}_1 - \mathbf{b}_2)$ and $J_0 = 0.13t_\perp^0$, in (e) $\mathbf{q} = 0.05(\mathbf{b}_1 - \mathbf{b}_2)$ and in (f) $J_0 = 0.13t_\perp^0$.

3.2.3 Summary

In this section, we have seen how helimagnets can be utilized in engineering helical states. We first showed that a single-layer helimagnet in

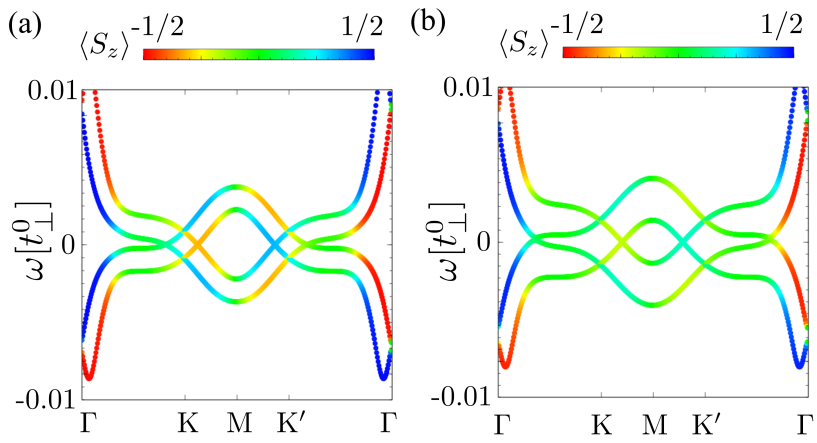

Figure 3.6. Band structure of TBG with incommensurate helimagnetic encapsulation Eq. (3.20) where $f_1 = f_2 = 1$, with $\mathbf{q} = 0.05(\mathbf{b}_1 - \mathbf{b}_2)$ and (a) $J_0 = 0.03t_\perp^0$ and (b) $J_0 = 0.06t_\perp^0$.

proximity to graphene can induce helical states in graphene. We then show that helimagnetal encapsulation creates helical states in TBG, similar to graphene. The difference to graphene is, the band crossings at Γ and M points are protected by symmetry in some cases in TBG, which results in multiple Fermi surfaces that prevents topological superconductivity. The emergence of helical states in helimagnetically engineered graphene and in particular in TBG would allow to promote topological superconductivity in these systems.

3.3 Heavy fermions in a bilayer van der Waals heterostructure

In this section, we show the realization of heavy-fermion physics in a 1T/1H-TaS_2 heterostructure [40], with an emphasis on the theoretical design. We first present how the Kondo lattice model Eq. (3.4) results in heavy-fermion physics. We then discuss how heavy fermions are realized and identified in 1T/1H-TaS_2 heterostructure.

3.3.1 Heavy fermions in the Kondo lattice model

The Kondo lattice model Eq. (3.4) represents one of the biggest challenges to solve even up to date [209]. Traditionally, this model was tackled using the large-N expansion [210–213]: assuming the spin-degree of freedom is N instead of 2, and that the N spin degrees of freedom are degenerate. In the limit $N \to \infty$, this allows us to drop terms of $O(1/N^2)$, and simplify

Eq. (3.4) as [211]:

$$H = H_{\text{kinetic}} + \frac{J_K}{N} \sum_i c^\dagger_{i,\beta} c_{i,\alpha} S_{i,\alpha\beta}. \tag{3.21}$$

where $S_{i,\alpha\beta}$ can be represented with pseudo-fermions:

$$S_{i,\alpha\beta} = f^\dagger_{i,\alpha} f_{i,\beta} - \frac{1}{N}\delta_{\alpha\beta} \tag{3.22}$$

with constraint $\sum_\alpha f^\dagger_{i,\alpha} f_{i,\alpha} = 1$. Physically, the large-N expansion drops terms of $O(1/N^2)$, which include RKKY interactions that tend to order the magnet. The remaining Hamiltonian Eq. (3.21) describes the electrons coupled to the partons $f_{i,\alpha}$ which are deconfined. Further performing a saddle point approximation [197] to Eq. (3.21), we obtain a mean-field Hamiltonian:

$$H = H_{\text{kinetic}} + \gamma_K \sum_{i,\alpha} (c^\dagger_{i,\alpha} f_{i,\alpha} + h.c.) \tag{3.23}$$

where $\gamma_K \propto e^{-1/(\rho(E_F) J_K)}$ characterizes the hybridization of electrons and pseudofermions into heavy fermions, with $\rho(E_F)$ being the density of states at Fermi level for the electrons.

Although Eqs. (3.21) and Eq. (3.23) are derived from a large-N expansion, they form a useful effective theory to illustrate the heavy fermion physics for small N systems. We thus utilize Eq. (3.23) to illustrate the heavy fermion physics in 1T/1H-TaS_2 in the next section.

3.3.2 Heavy fermions in 1T/1H-TaS_2 heterostructure

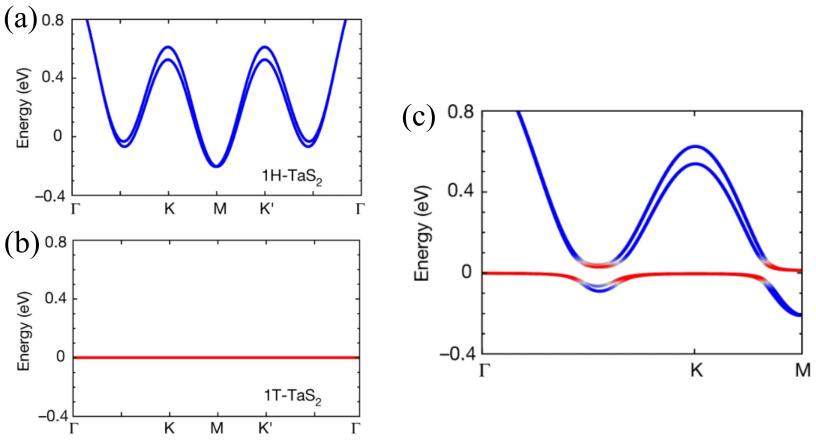

Figure 3.7. (a) Electronic band structure of 1H-TaS_2. (b) Pseudofermion band structure of 1T-TaS_2. (c) Hybrid band structure of 1T/1H-TaS_2 heterostructure. All panels are adapted from Ref. [40].

We now illustrate the heavy-fermion physics in the 1T/1H-TaS_2 heterostructure. As we have seen in Sec.2.1, 1T-TaS_2 hosts magnetic moments due to the formation of charge density waves (CDW). The CDW together with the spin-orbit coupling (SOC) results in a half-filled narrow band at the Fermi energy, with a bandwidth of a few 10meV [42]. On the other hand, 1H-TaS_2 is metallic [214] with a conduction band of bandwidth on the order of eV (Fig.3.7(a)). The chemical similarity between 1T-TaS_2 and 1H-TaS_2 allows a versatile synthesis of a heterostructure between them. When proper couplings between 1T-TaS_2 and 1H-TaS_2 is present, the heavy-fermion regime arises, and can be captured with the effective model Eq. (3.23) where the small pseudofermion dispersion is neglected and treated as a flat band (Fig.3.7(b)). Diagonalizing Eq. (3.23) for this heterostructure, we get a hybrid band structure (Fig.3.7(c)), highlighting a gap opening at the Fermi level due to the formation of heavy fermions.

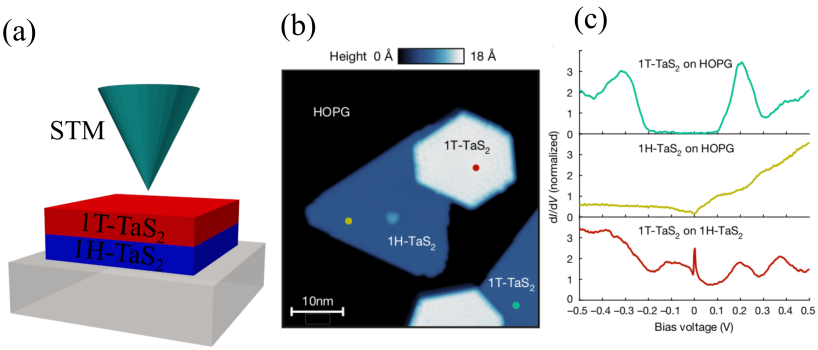

Figure 3.8. (a) Sketch of the STM setup to probe Kondo effect in 1T/1H-TaS_2 heterostructure. (b) STM image of a 1T/1H-TaS_2 vertical heterostructure on HOPG substrate. (c) Tunneling spectra of monolayer 1T-TaS_2 on HOPG (green), 1H-TaS_2 on HOPG (yellow) and monolayer 1T-TaS_2 on 1H-TaS_2 (red), corresponding to the dots of the same colour in (b). Panels (b) and (c) are adapted from Ref. [40].

Interestingly, due to the versatility of the 2D heterostructure, we are able to perform STM measurements from both the 1T and 1H sides by performing measurements on different islands. Let us first look at the measurement on the 1T side (Fig.3.8(a)), where the Kondo coupling results in additional tunneling mechanisms that interfere with direct tunneling processes. This interference is known to give rise to the Fano resonance [215], resulting in a Fano lineshape in the tunneling spectroscopy as shown in Fig.3.8(c). The field dependence of this Fano lineshape is in agreement with the Kondo mechanism, and the temperature dependence reveals a Kondo temperature of 18K [40].

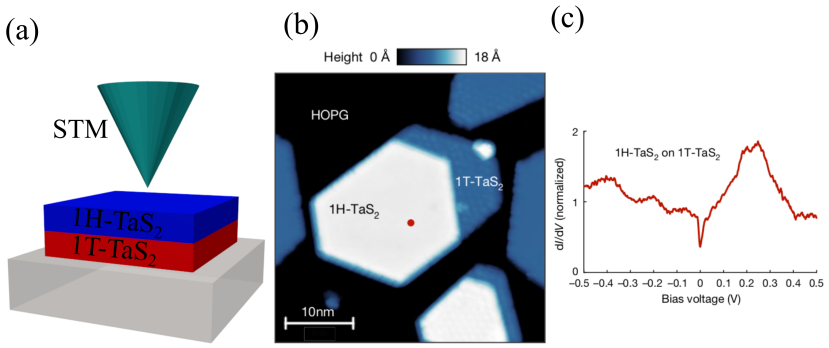

Figure 3.9. (a) Sketch of the STM setup to probe the heavy-fermion gap in 1H/1T-TaS_2 heterostructure. (b) STM image of a 1H/1T-TaS_2 vertical heterostructure on HOPG substrate. (c) Tunneling spectra of monolayer 1H-TaS_2 on 1T-TaS_2, corresponding to the dot of the same colour in (b). Panels (b) and (c) are adapted from Ref. [40].

On the other hand, if we perform a measurement on the 1H side (Fig.3.9(a)), due to the hybridization, we are expected to observe a heavy-fermion gap. This will result in a dip in the tunneling spectrum at zero bias, as is shown in Fig.3.9(c). The temperature and field dependence of this dip feature agrees with the behaviour of Kondo in the other heterostructure, and further demonstrates the heavy-fermion physics in this heterostructure.

3.3.3 Summary

In this section, we have seen how 2D magnets can be utilized in engineering heavy fermions. We first presented how heavy fermions arise from the Kondo lattice model which describes the magnet/conductor heterostructure in some regimes. We then show that the 1T/1H-TaS_2 heterostructure provides an experimental realization of heavy fermions.

3.4 Summary

Magnetic 2D materials are versatile for engineering the properties of other 2D materials. In this chapter, we demonstrated its power in designing helical states and heavy fermions. In particular, we showed the regime of proximity magnetic field and the regime of Kondo lattice for different coupling strengths in a magnet/conductor heterostructure. We showed that the proximity to helimagnets would give rise to an effective spatially-dependent magnetic field, which can be utilized to induce helical states in graphene and TBG. We also showed that the Kondo lattice can host heavy

fermions, which can be realized in the 1T/1H-TaS_2 heterostructure.

4. Utilizing the coupling to the world

We have seen in previous chapters how we can engineer exotic phases of matter with magnetic 2D materials. In these studies, we have been neglecting the effects of our system coupling to the rest of the world, which we refer to as the environment. In most cases this is fine as the system decays into the new ground state so fast due to coupling to the environment that we care only about the new ground state. In this case the environment can be modeled as an effective term. One illustrative example is the proximity effect: when we stack the 2D material (system) we are interested in on top of another one (environment), the coupling between these 2D materials will modify the ground state of the system. The fast dynamics from the old ground state to the new one is hardly accessible in experimental measurements. Thus we care only about the new ground state, which is dominated by the unperturbed system Hamiltonian plus a proximity term such as an effective magnetic field in Eq. (3.2) or a lattice potential. Another example is twisted multilayer 2D materials: when we stack multiple 2D materials in an incommensurate way, the lattice potential will result in the relaxation of the lattice structure and lead to commensurate stacking regions separated by domain walls. The relaxation takes place so fast that the properties of the system in an STM measurement are solely determined by the new commensurate twisted structure. Finally, the STM experiment itself is an example where we neglect the coupling to the environment, the STM tip. Due to this coupling, electrons can tunnel from the STM tip to the 2D material we are interested in. We can neglect the influence of this process on the property of the material since the electron quickly goes into the substrate and the system quickly relax to the unperturbed state. Quantitatively, the typical time scale for a tunneling process is ~ 1ps, which is way below the typical time scale of signals in an STM measurement.

However, the influence of coupling to the environment becomes not negligible when we care about high-frequency signals. In an STM measurement, it is due to the couplings to a variety of environments that creates high-frequency noise which hinders potential high-frequency signals. Another example where the coupling to the environment has more severe damage is in quantum computing, where the information stored in a qubit gets scrambled in nanoseconds due to coupling to the environment. This remarkable challenge greatly limits the power of quantum computing.

In addition to overcoming technical challenges, it is also of fundamental interest to understand the behavior of a (quantum) system coupled to the environment, usually called an open (quantum) system. A systematic understanding of open systems whose evolution is Markovian has been established, and this kind of system has been realized in highly-tunable platforms such as quantum optical systems and cold atom systems. Further than that, non-Markovian processes have been under intense investigation, providing us with more prediction power for open quantum systems. Yet, these studies have been limited to systems where interactions do not play an important role or small-size systems with interactions.

Condensed matter systems, despite not being the first platform to study the physics of open quantum systems, have recently emerged as a platform to investigate open quantum systems with interaction [216]. The advantage of condensed matter systems in the study of open quantum many-body physics is the easy access to a large system where both many-body interactions and openness are present. However, the biggest challenge is to overcome "random" couplings that result in noises. The recently raised pump-probe technique combined with STM [217–220] paves a way to solving this problem. In particular, for a spin system, Ref. [220] demonstrates the excitation of a quantum spin with a pulse of nano-seconds long and unveils the decay of the spin in the following ~ 100ns. The technical development towards turning "open noise" into "open signal" in condensed matter motivates us to think whether we can engineer the coupling to the environment, such that it becomes useful [221, 222]. In particular, we are interested in (i) overcoming experimental challenges, such as the information loss in quantum computing and (ii) enriching our fundamental understanding of open quantum many-body systems. We will show in this chapter how engineered coupling to the environment would allow to design topological phases of matter, which provides an answer to the questions above.

The rest of this chapter is organized as follows: in Sec.4.1 we review the theoretical framework to study Markovian open quantum systems, highlighting the quantum master equation and its relation to non-Hermitian (NH) matrices. In Sec.4.2 we review the study of topological phenomena in NH systems. In Sec.4.3 we present our result on designing NH topological many-body phases of matter.

4.1 Introduction to the dynamics of open quantum systems

4.1.1 Pedagogical example: quantum measurement

To illustrate how coupling to an environment modifies the dynamics of a quantum system, we present a pedagogical example: the quantum measurement [1, 223].

A quantum measurement refers to the process of probing a quantum observable. This is usually done through a machine/apparatus that generates different values for a macroscopic variable according to different values of the quantum observable. A typical example is the Stern-Gerlach experiment (conducted 101 years ago!), which probes the spin of electrons by injecting them into a region with an inhomogeneous magnetic field, and examines the positions of the electrons on the screen after the magnetic region. In the original Stern-Gerlach experiment, the observable we want to measure is the spin of the electron in z-direction, the apparatus is the applied magnetic field in z-direction and the screen, and the macroscopic variable is the location of the electrons on the screen. It is found in this experiment that unlike a classical magnet, the spin of electrons is quantized: the spins of an electron can either be $1/2$ or $-1/2$, since the position shift of the electrons are either $+L$ or $-L$ in z-direction where L depends on the gradient of the magnetic field and length of the magnetic field region.

To illustrate the theoretical framework describing this experiment, let's denote the spin-up/down states in z direction for the electron as $|0\rangle$ and $|1\rangle$, and denote $|\pm\rangle = \frac{1}{2}(|0\rangle \pm |1\rangle)$. Let's denote that macroscopic variable of the position of the electrons as $|z_\pm\rangle$ and $|\Omega\rangle$, where $|\Omega\rangle$ denotes no electrons are seen on the screen. In this way, when an electron goes through the inhomogeneous magnetic field in z direction, the following unitary transformation is applied to the electron and the screen:

$$U = |0\rangle\langle 0| \otimes |z_+\rangle\langle\Omega| + |1\rangle\langle 1| \otimes |z_-\rangle\langle\Omega|. \tag{4.1}$$

For example, if the initial state of the electron is $|0\rangle$, then the initial state of the whole system is $|\psi_0\rangle = |0\rangle \otimes |\Omega\rangle$, then $U|\psi_0\rangle = |0\rangle \otimes |z_+\rangle$ is the final state. More interestingly, if the initial electron is polarized in x direction $\rho_{0,e} = |+\rangle\langle+|$, the state of the whole system after the unitary transformation is:

$$\rho = U(\rho_{0,e} \otimes |\Omega\rangle\langle\Omega|)U^\dagger = \frac{1}{2}(|0\rangle\langle 0| \otimes |z_+\rangle\langle z_+| + |1\rangle\langle 1| \otimes |z_-\rangle\langle z_-|). \quad (4.2)$$

Eq. (4.2) informs us that the probability of finding the electron in position $|z_+\rangle$ is $\mathrm{tr}(\rho \mathbf{I} \otimes |z_+\rangle\langle z_+|) = 1/2$, where $\mathbf{I}$ is the identity matrix, and correspondingly we know the electron is in state $|0\rangle$. Similarly, we know that the electron has $1/2$ probability to be in state $|1\rangle$. Effectively, we can describe the state of the electron with a density matrix $\rho_{\mathrm{final},e} = 1/2(|0\rangle\langle 0| + |1\rangle\langle 1|)$. We see that, due to the coupling to the machine, the electron has gone through a non-unitary evolution that projects it on the states polarized in z axis:

$$\rho_{\mathrm{final},e} = \sum_{i=0,1} P_i \rho_{0,e} P_i \quad (4.3)$$

where $P_i = |i\rangle\langle i|$ is the projection on the basis $|i\rangle$.

In general, during a quantum measurement, we first project the system on a complete orthogonal basis P_i:

$$P_i P_j = \delta_{ij} P_i, P_i = P_i^\dagger, \sum_i P_i = \mathbf{I} \quad (4.4)$$

and modify the macroscopic state of the machine simultaneously by a unitary transformation:

$$U = \sum_{i,n} P_i \otimes |n+i\rangle\langle n| \quad (4.5)$$

where $|n\rangle$ is a complete orthogonal basis for the machine and $|n+i\rangle$ is the resulting state of the machine when the system is in the state $|i\rangle$ and the machine has initial state $|n\rangle$. Suppose the initial state of the whole system is $\rho_0 \otimes |0\rangle\langle 0|$, then the final state is

$$\rho_{f,\mathrm{tot}} = U(\rho_0 \otimes |0\rangle\langle 0|) = \sum_i P_i \rho_0 P_i \otimes |i\rangle\langle i|. \quad (4.6)$$

The probability to observe the machine in state $|i\rangle$ is $\mathrm{tr}(\rho_{f,\mathrm{tot}} \mathbf{I} \otimes |i\rangle\langle i|) = \mathrm{tr}(P_i \rho_0 P_i)$. Correspondingly, the system is in the normalized state $P_i \rho_0 P_i / \mathrm{tr}(P_i \rho_0 P_i)$. Thus, the system is effectively described by the following density matrix before we measure the outcome of the machine state:

$$\sum_i \mathrm{tr}(P_i \rho_0 P_i) \frac{P_i \rho_0 P_i}{\mathrm{tr}(P_i \rho_0 P_i)} = \sum_i P_i \rho_0 P_i, \quad (4.7)$$

which provides the non-unitary evolution of the system under the quantum measurement. In addition, if the outcome of the machine state is measured and found in state $|i\rangle$, the system would be projected with P_i, yielding the state

$$\rho_f = \frac{P_i \rho_0 P_i}{\mathbf{tr}(P_i \rho_0 P_i)}. \tag{4.8}$$

Eq. (4.8) describes the non-unitary evolution of the system when a specific result is obtained for the machine state.

In addition to a quantum measurement, there are also other cases when the quantum system we are interested in is coupled to an environment and becomes open. We are interested in a more general description of the dynamics of such systems, which we illustrate in the next section.

4.1.2 The quantum master equation

In this section we derive the general formula for the evolution of an open quantum system, without digging into the microscopic details. A microscopic derivation can be found in Ref. [224]. A generic evolution should map a quantum state to another one. From quantum theories we know that any state can be described by a density matrix ρ that satisfy:

- normalized probability: $\mathrm{tr}\rho = 1$
- (semi-)positive definite: $\langle\psi|\rho|\psi\rangle \geq 0$, $\forall|\psi\rangle$ in the same Hilbert space.
- hermiticity: $\rho = \rho^\dagger$

Thus, a quantum evolution is a mapping between density matrices $F : \rho \to \rho'$, that should satisfy:

- trace-preserving: $\mathrm{tr}\rho = \mathrm{tr}F(\rho)$
- positivity-preserving: if ρ is (semi-)positive definite, $F(\rho)$ is also (semi-)positive definite.

In addition, the evolution should satisfy convex-linearity:

$$F\left(\sum_i p_i \rho_i\right) = \sum_i p_i F(\rho_i) \tag{4.9}$$

where $\sum_i p_i = 1$. This follows from the fact that $\rho = \sum_i p_i \rho_i$ can be considered as an ensemble with probability p_i of being on the state ρ_i. Thus, $F(\rho)$ can be considered as an ensemble with p_i probability in the

state $F(\rho_i)$, hence Eq. (4.9). We have used the trace-preserving property of F in the above derivation[1].

Finally, suppose we have a larger system containing the system in state ρ: $\rho_{\text{tot}} = \rho \otimes \rho'$. We would expect the evolution $F \otimes \mathbf{I}$ to map ρ_{tot} to another density matrix. That is, if ρ_{tot} is positive-definite, $(F \otimes \mathbf{I})\rho_{\text{tot}}$ is also positive-definite.

Summarizing the above, we have that the mapping F describing the evolution of a quantum state ρ should satisfy:

- convex-linear: $F(\sum_i p_i \rho_i) = \sum_i p_i F(\rho_i)$
- trace-preserving: $\text{tr}\rho = \text{tr}F(\rho)$
- completely positive: $\rho \otimes \rho' \geq 0$ implies $(F \otimes \mathbf{I})(\rho \otimes \rho') > 0$, $\forall \rho, \rho'$

It can be proved that a mapping F satisfies the above 3 properties if and only if F can be represented as:

$$F(\rho) = \sum_i K_i \rho K_i^\dagger \tag{4.10}$$

for some set of operators K_i [1] satisfying $\sum_i K_i^\dagger K_i = \mathbf{I}$. A convex-linear trace-preserving completely positive (TPCP) map is also called a quantum channel, and Eq. (4.10) is an operator-sum representation of a quantum channel. The operators K_i are called Kraus operators. We see that quantum measurement is a specific kind of quantum channel where the Kraus operators are Hermitian.

We now consider the time-evolution of an open quantum system:

$$\rho(t) = F_t[\rho(0)] = \sum_\alpha K_{\alpha,t} \rho(0) K_{\alpha,t}^\dagger, \tag{4.11}$$

and we introduce the assumption of Born-Markov approximation to simplify the evolution. Born-Markov approximation requires that the evolution of the system is local in time, i.e. the state $\rho(t + dt)$ is completely determined by $\rho(t)$. This approximation allows us to write the equation of motion for $\rho(t)$ as

$$\frac{d}{dt}\rho(t) = \mathcal{L}[\rho(t)] \tag{4.12}$$

where $\mathcal{L}$ is a superoperator acting on $\rho(t)$. Inserting Eq. (4.12) into Eq. (4.11), we have

$$\frac{d}{dt}F_t = \mathcal{L}F_t \tag{4.13}$$

[1]The property should also hold for non-trace-preserving mappings, which can be interpreted as part of a quantum trajectory.

That is, the mapping/superoperator F_t can be generated by $\mathcal{L}$: $F_t \propto e^{\mathcal{L}t}$, this allows us to determine F_t with the infinitesimal time-evolution $F_{dt} \approx 1 + \mathcal{L}dt$. We have

$$\rho(t+dt) = F_{dt}[\rho(0)] = \sum_\alpha K_{\alpha,t}\rho(0)K_{\alpha,t}^\dagger = \rho(t) + O(dt). \tag{4.14}$$

Without loss of generality, we may assume that $K_{0,dt} = \mathbf{I} + O(dt)$, and $K_{\alpha,dt} = O(\sqrt{dt})$.[2] Consider $K_{0,dt} = \mathbf{I} - iHdt$ and $K_{\alpha,dt} = 0$ otherwise, we have $F_{dt}[\rho] = \rho - i[H,\rho]dt$, which is the von Neumann equation for the time-evolution of a closed quantum system. Generically, we have

$$\begin{aligned} K_{0,dt} &= \mathbf{I} - iAdt \\ K_{\alpha,dt} &= L_\alpha\sqrt{dt} \end{aligned} \tag{4.15}$$

The condition $\sum_\alpha K_\alpha^\dagger K_\alpha = 1$ requires $\sum_\alpha L_\alpha^\dagger L_\alpha = i(A^\dagger - A)$, we can thus write A as $A = H - i\sum_\alpha L_\alpha^\dagger L_\alpha/2$ where H is a Hermitian operator. The time evolution generated with this set of Kraus operators is

$$\frac{d}{dt}\rho(t) = \mathcal{L}[\rho(t)] = -i[H,\rho(t)] + \sum_\alpha \left(L_\alpha\rho(t)L_\alpha^\dagger - \frac{1}{2}\{L_\alpha^\dagger L_\alpha, \rho(t)\}\right) \tag{4.16}$$

Eq. (4.16) is called the quantum master equation, $\mathcal{L}$ is called the Liouvillian superoperator, and the operators L_α are called jump operators or Lindblad operators, attributed to the original discovery of this equation by Lindblad, et. al [225, 226]. The first term of Eq. (4.16) describes the dynamics of a closed quantum system with the Hamiltonian H, and the second term describes the non-unitary evolution of the system due to coupling to the environment.

4.1.3 Relation to non-Hermitian (NH) matrices

We now discuss how the dynamics of an open quantum system described by the quantum master equation Eq. (4.16) can be captured by diagonalizing non-Hermitian matrices. The first observation is that if we vectorize the density matrix ρ:

$$\rho = \sum_{i,j}\rho_{ij}|i\rangle\langle j| \to |\tilde{\rho}\rangle = \sum_{i,j}\rho_{ij}|i\rangle|j\rangle, \tag{4.17}$$

the quantum master equation becomes

$$\frac{d}{dt}|\tilde{\rho}\rangle = \tilde{L}|\tilde{\rho}\rangle \tag{4.18}$$

[2]The operator-sum representation for a quantum channel is not unique, one can perform a unitary transformation to get a different operator-sum representation.

with

$$\tilde{\mathcal{L}} = -iH \otimes \mathbf{I} + i\mathbf{I} \otimes H^T + \sum_\alpha \left(L_\alpha \otimes L_\alpha^* - \frac{1}{2}(L_\alpha^\dagger L_\alpha \otimes \mathbf{I} + \mathbf{I} \otimes L_\alpha^T L_\alpha^*) \right) \quad (4.19)$$

being a non-Hermitian operator. Diagonalizing $\tilde{\mathcal{L}}$, we get its eigenvalues and right eigenvectors $\{\lambda_n, |\tilde{\rho}_n\rangle\}$. Thus, the evolution for $|\tilde{\rho}(0)\rangle = \sum_n c_n |\tilde{\rho}_n\rangle$ becomes

$$|\tilde{\rho}(t)\rangle = \sum_n c_n e^{\lambda_n t} |\tilde{\rho}_n\rangle, \quad (4.20)$$

or, in the form of density matrices:

$$\rho(t) = \sum_n c_n e^{\lambda_n t} \rho_n. \quad (4.21)$$

Since the evolution is trace-preserving, we have

$$\frac{d}{dt}(\mathrm{tr}\rho(t)) = \sum_n c_n \lambda_n e^{\lambda_n t} \mathrm{tr}\rho_n = 0, \quad (4.22)$$

indicating that either $\lambda_n = 0$ or $\mathrm{tr}\rho_n = 0$ for all n. In addition, we have $\mathrm{tr}\rho(t) = 1$, thus there exists at least one zero eigenvalue λ_m such that the corresponding density matrix is not traceless: $\mathrm{tr}\rho_m \neq 0$. In addition, due to the TPCP property of $F_{dt} = e^{\mathcal{L}t}$, it can be proved that the real part of all the eigenvalues of $\mathcal{L}$ are 0 or negative.

Thus, by solving the non-Hermitian matrix $\tilde{\mathcal{L}}$, we can answer what the steady state is–i.e. the state after long-time evolution, which is simply the eigenstate corresponding to the 0 eigenvalue of $\tilde{\mathcal{L}}$. In addition, we can answer how fast the system decays into the steady state. This time scale is determined by the second-largest real eigenvalue of $\tilde{\mathcal{L}}$, and is usually referred to as the Liouvillian gap.

Interestingly, another regime in the dynamics of open quantum systems can also be described by a non-Hermitian matrix. Recall from Eq. (4.8) that when a result $|i\rangle$ is observed in a quantum measurement, the system undergoes an evolution given by the Kraus operator K_i. In the quantum master equation described by the Kraus operators Eq. (4.15), if we perform a measurement with an outcome related to the Kraus operator $K_{0,dt}$, we would have

$$\rho(t + dt) = K_{0,dt}\rho(t)K_{0,dt}^\dagger = \rho(t) - i(A\rho(t) - \rho(t)A^\dagger) + O(dt^2) \quad (4.23)$$

yielding

$$\rho(t) = e^{-iAt}\rho(0)e^{iA^\dagger t} \quad (4.24)$$

with the non-Hermitian matrix $A = H - i\sum_\alpha L_\alpha^\dagger L_\alpha/2$. Eq. (4.24) describes the dynamics of the system between two quantum jumps. Experimentally, we can select the path with such evolution by successively performing a quantum measurement on the system and picking the path that no quantum jump has occurred [227–229], which is referred to as post-selection.

4.2 NH topology

We have seen in the previous section how solving the dynamics of an open quantum system can be simplified to solving non-Hermitian matrices. In fact, in addition to describing the dynamics of open quantum systems, the study of the properties of non-Hermitian Hamiltonians is of great theoretical interest. The interplay between non-Hermicity with symmetry [230–232] and topology [233–239] has led to unique phenomena without a counterpart in Hermitian systems. We are particularly interested in NH topology in our case as it may find application in utilizing the openness of quantum systems for topological prediction.

4.2.1 Hermitian topology

Let us first briefly go through the study of topological phenomena in Hermitian systems. The investigation of topological effects was first inspired by the quantum Hall effect (QHE) [240]: the Hall resistivity of a 2D electron gas under strong magnetic field exhibits a series of plateaus with quantized values $h/(ne^2)$ with n being an integer. The quantized Hall resistance/conductance was then explained by D. J. Thouless et. al. [241]: using linear-response theory, they find that the quantized Hall conductance is related to a topological invariant–the TKNN number. The reason for the plateaus is due to the fact that the bulk is insulating: due to the existence of impurities in the sample, most bulk electrons get localized and the main contribution to the conductance comes from the edge electron channels, which is proportional to the TKNN number. We see that the essential ingredients for QHE are an insulating bulk with non-trivial topology and edge states related to the topological invariant of the bulk. The relation between the edge states and the non-trivial bulk topology is referred to as the bulk-boundary correspondence [242]. Plenty of models hosting these essential ingredients were proposed since then. Representative examples include the Haldane model [243] whose topological invariant is the Chern

number, and the quantum spin Hall insulator [244, 245] with a Z_2 topological invariant [246]. The topological invariant allowed in a model is related to the symmetry of the Hamiltonian, which has been classified into different symmetry classes [242].

Due to the translational symmetry of the above models, we can use Bloch band theory to study the topology of these models. We illustrate this with the Haldane model, whose Bloch Hamiltonian reads [243] (up to a k-dependent constant)

$$\begin{aligned} H(\mathbf{k}) =& t_1 \sum_i \left(\cos(\mathbf{k}\cdot\mathbf{a}_i)\sigma_x + \sin(\mathbf{k}\cdot\mathbf{a}_i)\sigma_y\right) \\ &+ \left(M - 2t_2 \sin\phi \left(\sum_i \sin(\mathbf{k}\cdot\mathbf{b}_i)\right)\right)\sigma_z \end{aligned} \tag{4.25}$$

The band structure of the above Hamiltonian is gapless for $M = 0$ and $\phi = 0, \pi$. Otherwise, the topological invariant of the gap is given by the Chern number:

$$C = i \int_{\mathrm{BZ}} \frac{d^2\mathbf{k}}{2\pi} \left(\langle \partial_x u(\mathbf{k}) | \partial_y u(\mathbf{k})\rangle - \langle \partial_y u(\mathbf{k}) | \partial_x u(\mathbf{k})\rangle\right) \tag{4.26}$$

where $|u(\mathbf{k})\rangle$ is the eigenstate corresponding to the smaller eigenvalue of $H(\mathbf{k})$. The Chern number is an integer number: $C = \pm 1$ for $|M/t_2| < 3\sqrt{3}|\sin\phi|$ and $C = 0$ otherwise. The number of chiral edge states under open boundary conditions is given by the Chern number, showing the bulk-boundary correspondence in this specific case.

In recent years, the study of Hermitian topology has been generalized to the interacting case. In the interacting case, calculation of the bulk topological invariant is no longer an easy task [95, 247, 248] as Bloch band theory no longer applies. Yet, bulk-boundary correspondence still holds and is used as an efficient way to examine the many-body topology: the characterization of topological boundary states [249] is much easier than computing bulk topological invariant, thus we use them to show the non-trivial topology in the bulk. We show this with the following model:

$$\begin{aligned} H =& J_1 \sum_{l=1}^{N/2} \left(S^x_{2l-1}S^x_{2l} + S^y_{2l-1}S^y_{2l}\right) + J_2 \sum_{l=1}^{N/2-1} \left(S^x_{2l}S^x_{2l+1} + S^y_{2l}S^y_{2l+1}\right) \\ &+ J_z \sum_{l=1}^{N-1} S^z_l S^z_{l+1} \end{aligned} \tag{4.27}$$

where $J_2 \neq J_1$. The model Eq. (4.27) can be mapped to the SSH model with

interactions with the Jordan-Wigner transformation:

$$\begin{aligned}\tilde{H} =& J_1 \sum_{l=1}^{N/2} \left(c_{2l-1}^\dagger c_{2l} + c_{2l}^\dagger c_{2l-1}\right) + J_2 \sum_{l=1}^{N/2-1} \left(c_{2l}^\dagger c_{2l+1} + c_{2l+1}^\dagger c_{2l}\right) \\ &+ J_z \sum_{l=1}^{N-1} \left(c_l^\dagger c_l - \frac{1}{2}\right)\left(c_{l+1}^\dagger c_{l+1} - \frac{1}{2}\right).\end{aligned} \tag{4.28}$$

Eq. (4.28) reduces to the SSH model when $J_z = 0$, where we know that topological boundary modes appear for $J_1 < J_2$. To reveal the topology of this model in the many-body case $J_z \neq 0$, we compute the local spectral function:

$$\chi(\omega, l) = \langle \mathrm{GS}|S_l^z \delta(\omega - H + E_0) S_l^z|\mathrm{GS}\rangle \tag{4.29}$$

where $|\mathrm{GS}\rangle$ is the ground state and E_0 is the ground state energy. The spectral functions computed with (i) $J_1 = J_z = J/2$ and $J_2 = J$ and (ii) $J_2 = J_z = J/2$ and $J_1 = J$ are shown in Fig.4.1. The spectral function reveals the existence of topological zero modes in case (i), indicating the non-trivial many-body topology in this case.

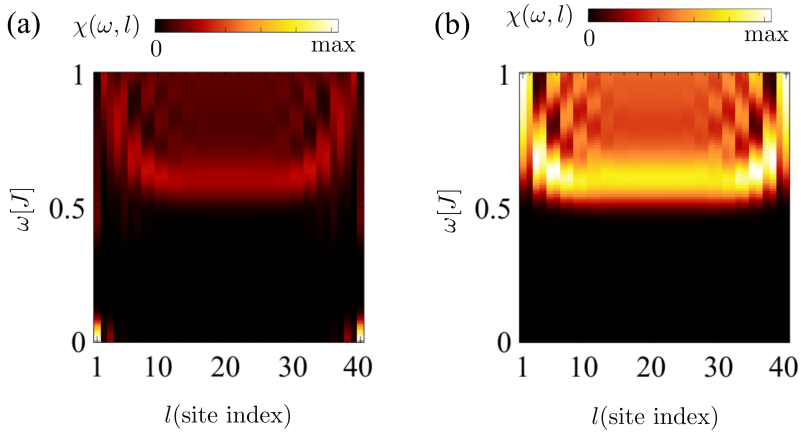

Figure 4.1. Local spectral function $\chi(\omega, l)$ of H defined in Eq. (4.27) with $N = 40$ and (a) $J_1 = J_z = J/2$ and $J_2 = J$ (b) $J_2 = J_z = J/2$ and $J_1 = J$.

In essence, the study of Hermitian topology focuses on the characterization of the topology of a gap (near Fermi level) by a topological invariant in the bulk and/or the behaviour of the topological edge states determined by bulk-boundary correspondence. We shall see in the next subsection that (i) the gap, (ii) the topological invariant and (iii) the bulk-boundary correspondence has non-trivial generalizations in the NH case.

4.2.2 NH topology

Let us first look at the spectral properties of a NH matrix. In general, an eigen-decomposition of a NH matrix is:

$$H = \sum_n \omega_n |\psi_{R,n}\rangle\langle\psi_{L,n}| \tag{4.30}$$

where $\omega_n \in \mathbb{C}$ are the eigenvalues, and $|\psi_{L(R),n}\rangle$ are the corresponding left(right) eigenvectors satisfying

$$\begin{aligned} H|\psi_{R,n}\rangle &= \omega_n|\psi_{R,n}\rangle \\ \langle\psi_{L,n}|H &= \omega_n\langle\psi_{L,n}| \\ \langle\psi_{L,m}|\psi_{R,n}\rangle &= \delta_{mn}. \end{aligned} \tag{4.31}$$

We see that due to the non-Hermicity, the eigenvalues ω_n are not necessarily real. In addition, the left and right eigenvectors do not have to be the same, and they satisfy the bi-orthogonal relation Eq. (4.31).

The fact that the eigenvalues of a non-Hermitian matrix spread over the complex plane allows for two different definitions of a non-Hermitian gap [233, 234, 250]: the line gap and the point gap. When the spectrum of a Hamiltonian does not appear on a line in the complex plane, we say that this is a line gap of the Hamiltonian. The line gap is a generalization of the gap in the Hermitian case: when all eigenvalues lie on the real axis, the line perpendicular to the real axis that goes across the real gap is the line gap. The point gap is defined as a point that the spectrum of the Hamiltonian does not go across.

Due to the two different definitions of a NH gap, there exists correspondingly different gap topology. The line gap topology is a generalization of the Hermitian gap topology. Whereas the point gap topology focuses on the winding of the spectrum with respect to a specific point on the complex plane and is non-trivial when the winding is non-zero. Thus the point gap topology is a unique feature of NH systems: although we can define point gap in a Hermitian system, its topology must be trivial as the winding of the spectrum with respect to this point is 0. The topological classification of NH Hamiltonians [235] is different from Hermitian Hamiltonians, and can have different topological invariants.

We have seen the differences in the definition of a gap and the corresponding topology between Hermitian and NH systems. To this end, we discuss the generalization of bulk-boundary correspondence (BBC) in Hermitian systems to non-Hermitian ones. Essentially, a direct correspondence be-

tween the topological invariant of a gap and the number of boundary states no longer holds in the non-Hermitian case. This have been demonstrated in a 1D lattice with asymmetric hoppings [236] in which topological boundary modes appear even when the line gap closes. The reason for this is the strong dependence of the behaviour of bulk states on the boundary condition: under PBC, the bulk states are well-defined Bloch waves, whereas under OBC, the bulk states are localized at the boundary instead of being extended as in the Hermitian case. This localization of bulk states under OBC is named non-Hermitian skin effect (NHSE) [236, 239, 251], which is the reason for the breakdown of conventional BBC. To recover the BBC, one has to take into account that NHSE makes the bulk states to have complex wave-vectors, and these complex wave-vectors lie on a generalized Brillouin zone (GBZ). In 1D, a non-Bloch band theory [252] has been developed to systematically compute the GBZ. Whereas in higher dimensions the calculation of GBZ remains a challenge.

Interestingly, BBC also exists for a non-trivial point gap. The boundary modes corresponding to a topologically nontrivial point gap are essentially the localized modes due to NHSE [253, 254].

In short, NH topology shows a drastic difference from conventional Hermitian topology. A systematic theoretical regime has been established to study NH topology for 1D. Yet, even for 2D non-interacting NH systems the discussion about topology is a remarkable challenge. The investigation of NH topology for interacting systems is even harder.

4.3 NH many-body topology in NH spin chain

With the understanding that NH Hamiltonians describe the dynamics of open quantum systems and that the topology of NH Hamiltonian is understood at 1D non-interacting level. We are finally in a situation to ask (i) how to engineer open quantum many-body systems in order to have topologically protected states and (ii) how to understand the NH topology in interacting (1D) systems. Interestingly, as a building block towards both these goals, the characterization of NH topology in interacting 1D systems with (i) easy-to-compute and (ii) experimentally accessible quantities is essential. Utilizing the BBC, we come up with a characterization of NH many-body topology by probing local spectral functions that reveal topo-

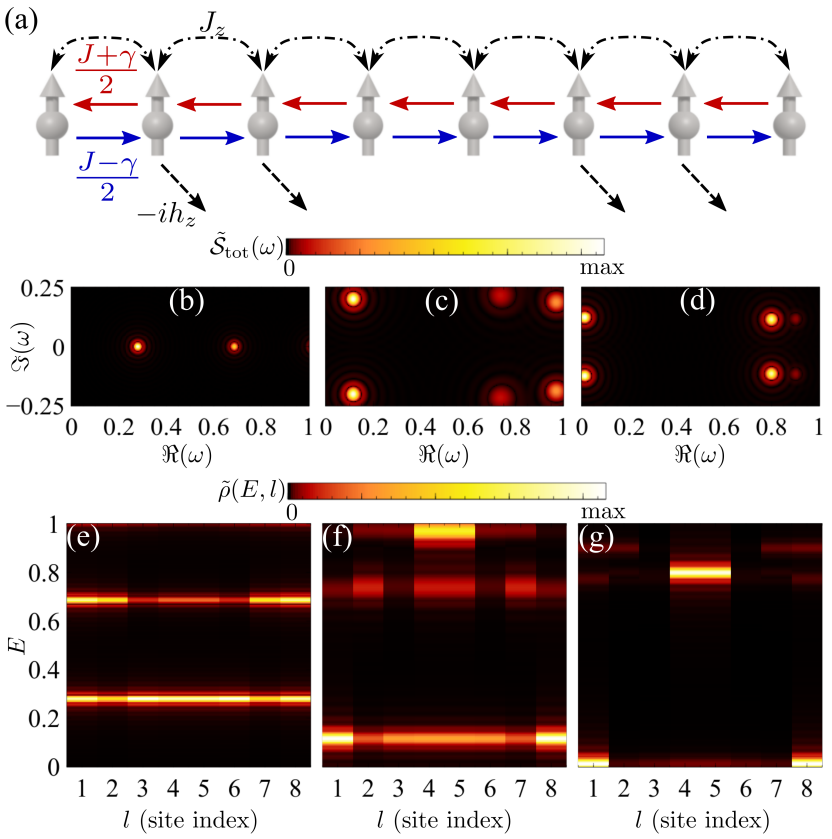

Figure 4.2. (a) Sketch of the model Hamiltonian H in Eq. (4.32). (b-d) Total dynamical spin correlator $\tilde{\mathcal{S}}_{\rm tot}(\omega)$ of H with $L=8$, $\gamma=0$ and (b) $h_z=0$, (c) $h_z=J$, (d) $h_z=2J$. (e-g) Projected local dynamical structure factor $\tilde{\rho}(E,l)$ corresponding to cases (b-d), respectively. Topological spin excitations with almost zero real energy are revealed in (g).

logical many-body excitations[3]. We illustrate our idea with a NH $S=1/2$ chain with antiferromagnetic exchange $J=1$ (Fig.4.2(a)):

$$H=\sum_{l=1}^{L-1}\left(\frac{J+\gamma}{2}S_l^+S_{l+1}^-+\frac{J-\gamma}{2}S_l^-S_{l+1}^++J_zS_l^zS_{l+1}^z\right)+\sum_{l=1}^{L}ih_l^zS_l^z \tag{4.32}$$

where $h_l^z=-h_z$ if $l \mod 4=2,3$ and $h_l^z=0$ otherwise. It is first illustrative to perform a Jordan-Wigner transformation to Eq. (4.32), leading to a

[3]The rest of this section is adapted from G. Chen, F. Song and J. L. Lado, Phys. Rev. Lett. 130, 100401 with revisions.

NH interacting spinless fermion model:

$$\begin{aligned}\tilde{H} = \sum_{l=1}^{L-1} \Bigg(& \frac{J+\gamma}{2} c_l^\dagger c_{l+1} + \frac{J-\gamma}{2} c_{l+1}^\dagger c_l \\ & + J_z (c_l^\dagger c_l - \frac{1}{2})(c_{l+1}^\dagger c_{l+1} - \frac{1}{2}) \Bigg) + \sum_{l=1}^{L} i h_l^z (c_l^\dagger c_l - \frac{1}{2}).\end{aligned} \tag{4.33}$$

When $J_z = 0$, Eq. (4.33) becomes a non-interacting spinless fermion model, which for $\gamma = 0$ and nonzero h_z is known to give rise to topological end states whose real part of the energy is 0 [255, 256]. The bulk topology of this model is characterized by a hidden Chern number which faithfully predicts the number of stable end states with purely imaginary energy [256, 257]. It has been shown that in the presence of a finite interaction J_z, a sufficiently large h_z would still give rise to the topological end states [216]. We reveal the non-Hermitian many-body topology of the model via computing dynamical excitations $\mathcal{S}(\omega, l)$:

$$\begin{aligned}\mathcal{S}(\omega, l) = & \langle \mathrm{GS_L} | S_l^- \delta^2(\omega + E_{\mathrm{GS}} - H) S_l^+ | \mathrm{GS_R} \rangle \\ & + \langle \mathrm{GS_L} | S_l^+ \delta^2(\omega + E_{\mathrm{GS}} - H) S_l^- | \mathrm{GS_R} \rangle,\end{aligned} \tag{4.34}$$

using the Non-Hermitian Kernel Polynomial Method (NHKPM) introduced in Chapter 6, both in the absence and presence of NHSE. The NHKPM algorithm has a power-law scaling with respect to the system size compared to the exponential scaling for exact diagonalization (ED), thus making the quantity easy to compute for large systems. For concreteness we take $J_z = 1/2J$, and note that analogous results can be obtained for general values of J_z.

We first focus on a chain of length $L = 8$ and compute the total dynamical spin correlator, defined as:

$$\tilde{\mathcal{S}}_{\mathrm{tot}}(\omega) = \left| \sum_{l=1}^{L} \mathcal{S}(\omega, l) \right| \tag{4.35}$$

where $\mathcal{S}(\omega, l)$ is defined in Eq. (4.34) [4]. The total dynamical spin correlator reveals the energy of the states that have finite overlap with the ground state with one $S_z = \pm 1$ excitation. We see that as h_z increases, the real part of the energy of the lowest excited states is shifted towards 0, whereas the higher states are shifted away from 0 (Figs.4.2(b-d)). To see if the lowest excited states are topological end states, we compute the projected

[4] We take the absolute value in Eq. (4.35) since $\mathcal{S}(\omega, l)$ is no longer real-valued in this case.

local dynamical structure factor, defined as

$$\tilde{\rho}(E \in \mathbb{R}, l) = \left| \int \mathcal{S}(E + iy, l) dy \right|. \tag{4.36}$$

This quantity identifies the local spectral density of $S_z = \pm 1$ excitations at a given real energy E. In particular, when H is Hermitian, $\tilde{\rho}(E, l)$ is reduced to the local spin structure factor defined in Eq. (4.29). Figs.4.2(e-g) show $\tilde{\rho}(E, l)$ for different values of h_z, we see that for $h_z = 0$ the lowest states show non-vanishing spectral density in the bulk. As h_z increases to $h_z = J$ the spectral density in the bulk reduces, and eventually for sufficiently large $h_z = 2J$ the states become localized at the ends, reflecting the non-trivial line topology in the bulk. Due to the short chain length, finite-size effects prevent clearly observing topological end states for $h_z = J$ due to hybridization.

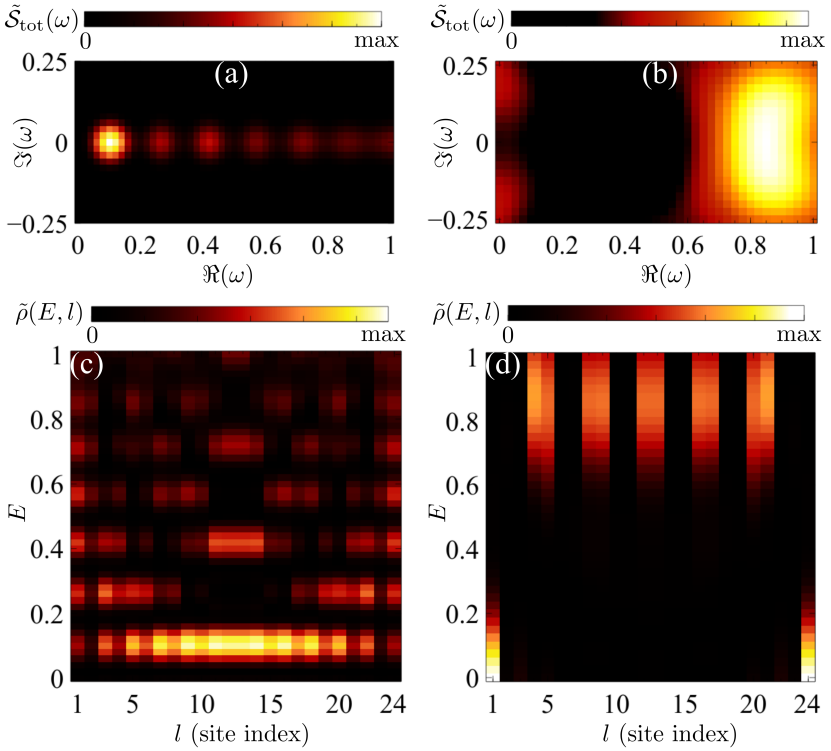

Figure 4.3. (a,b) Total dynamical spin correlator $\tilde{\mathcal{S}}_{\mathrm{tot}}(\omega)$ of H defined in Eq. (4.32) with $L = 24$, $\gamma = 0$ and (a) $h_z = 0$ and (b) $h_z = J$. $\tilde{\mathcal{S}}_{\mathrm{tot}}(\omega)$ reveals a many-body line gap in (b). (c,d) Projected local dynamical structure factor $\tilde{\rho}(E, l)$ corresponding to cases (a,b), respectively. $\tilde{\rho}(E, l)$ reveals topological many-body excitations in (d), indicating that the line gap in (b) is topological.

To approach the thermodynamic limit, we now move on to consider a chain of length $L = 24$. As these systems are too large to be treated by exact diagonalization, we now use a full tensor network implementation with

MPS in the NHKPM algorithm. The total dynamical spin correlator $\tilde{\mathcal{S}}_{\text{tot}}(\omega)$ and the projected local dynamical structure factor $\tilde{\rho}(E, l)$ are computed for $h_z = 0$ and $h_z = J$ in this case (Fig.4.3). We see from Figs.4.3(a,b) that for $h_z = J$ there are clearly 2 states close to 0 real energy, and are isolated from the higher states with a line gap, whereas for $h_z = 0$ there is no such behavior. From Figs.4.3(c,d) we can observe the topological end states for $h_z = J$, whereas for $h_z = 0$ the lowest states are mainly distributed in the bulk. These show that the model Eq. (4.32) is not topological for $h_z = 0$, and is topological for $h_z = J$ even in the presence of many-body interactions.

Interestingly, the way we come up with as a characterization of NH many-body topology does not suffer from NHSE. This can be demonstrated by considering a finite $\gamma < J$ in the Hamiltonian Eq. (4.34), which gives rise to NHSE. This case can be reduced to $\gamma = 0$ under a similarity transformation to H:

$$T = e^{\sum_l l\alpha S_l^z}, \alpha = \ln r, r = \sqrt{\frac{J+\gamma}{J-\gamma}}$$
$$TH(J, \gamma, J_z, h_z)T^{-1} = H'(J', 0, J_z, h_z). \tag{4.37}$$

The new uniform exchange is $J' = \sqrt{(J+\gamma)(J-\gamma)}$ which is approximately J for $\gamma = 0.1J$. This similarity transformation changes the spectral function Eq. (4.34) for H to the same spectral function for H', leading to dynamical correlators analogous to the $\gamma = 0$ case for $\gamma \ll J$, thus demonstrating the faithful prediction of boundary modes in the presence of NHSE.

To this end, let us discuss the potential probe of the topological boundary modes in an experimental setup, assuming the Hamiltonian Eq. (4.32) can be engineered with an array of magnetic atoms coupling to an engineered substrate. Basically, the spectral function Eq. (4.34) reveals local spin excitations at complex energy ω, that tells how a spin excitation evolves in time in this system. The real part of ω reveals the oscillation of this excitation in time and the imaginary part informs its decay. Thus, by first preparing the initial state to be the ground state, and applying a pulse that excites the local spin, the following short-time dynamics of the spin informs us about the spectral functions we computed in frequency space. Interestingly, this short-time dynamics can be probed with the pump-probe method that has recently been combined with STM [217–220], with a particular focus on spin dynamics in Ref. [220]. As an outlook, the scheme we proposed would eventually allow to engineer 2D magnetic materials utilizing the coupling to the world.

4.4 Summary

Quantum devices are inevitably open due to coupling to the environment. Instead of treating the effects of openness as noise, we can systematically understand the dynamics of an open quantum system under the Markovian approximation with the quantum master equation. The dynamics given by the quantum master equation can be captured by an effective non-Hermitian matrix. Non-Hermitian matrices host unique topological properties drastically different from Hermitian systems. Understanding NH many-body topology is of both applicational and fundamental interest. We present a non-Hermitian many-body system with non-trivial non-Hermitian many-body topology, where we put forward the local spectral function Eq. (4.34) as an easy-to-compute and experimentally accessible quantity to identify topological boundary modes in a non-Hermitian many-body system. Notably, the quantity faithfully reveals topological boundary modes in the presence of the NHSE, which breaks the conventional bulk-boundary correspondence. The topological boundary modes can be potentially probed with pump-probe STM, which allows to characterize the non-trivial bulk many-body topology.

5. Softwares developed

In this section, I present the two libraries I developed during my Ph.D. studies, Twistronics.jl and NHKPM.jl. The prerequisite to use these libraries is having Julia[1] installed.

The Twistronics.jl is a library focusing on solving band structures of twisted bilayer systems. It is built upon the up-to-date understanding of TBG, in particular, the independence of low-energy spectrum on the functional form of inter-layer coupling and the scaling relation. The objective of this library is to provide a versatile way to compute the band structure of twisted bilayer systems. In particular, it does not require the user to have knowledge of twisted multilayer systems.

The NHKPM.jl is a library focusing on computing spectral functions in NH many-body systems. It is built upon our recently developed non-Hermitian kernel polynomial method [258] and is still experiencing rapid development. The aim of this library is to overcome numerical challenges to solve NH many-body systems.

5.1 Twistronics.jl

The Twistronics.jl is a library focusing on solving band structures of twisted bilayer systems. This library can be downloaded from my github repository https://github.com/GUANGZECHEN/Twistronics.jl.

5.1.1 Supercell and band structure of TBG

Source code: Twistronics.jl/examples/Twisted_bilayer_graphene/TBG.jl

In Fig.5.1 we present the supercell and band structure of TBG computed with Twistronic.jl. Bands at different twist angles and be computed by

[1] https://julialang.org/. Current versions of the libraries are compatible with Julia version 1.7

tuning the parameters $m, r \in \mathbb{R}$ in the code, and the twist angle θ is given by $\theta = \arccos\left[(3m^2 + 3mr + r^2/2)/(3m^2 + 3mr + r^2)\right]$. We recommend computations with $r = 1$ for computational simplicity.

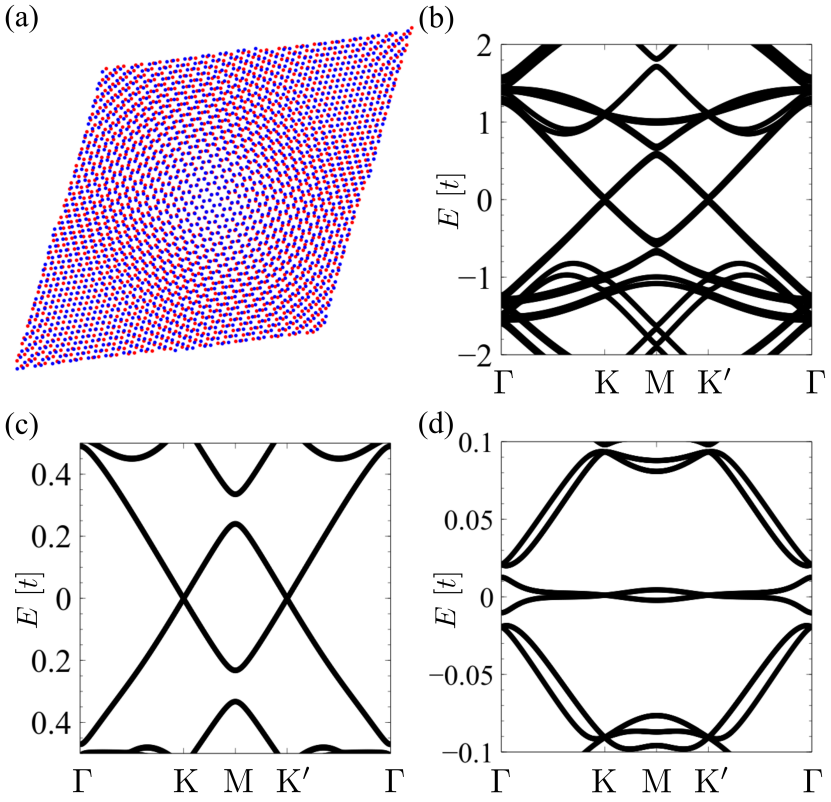

Figure 5.1. (a) Supercell of TBG at twist angle $1.89°$. (b)-(d) band structure of TBG at twist angle (b) $\theta = 21.79°$, (c) $\theta = 9.43°$ and (d) $\theta = 1.89°$.

5.1.2 Layer hybridization in TBG

Source code: Twistronics.jl/examples/tbg_layer_index/TBG_layer.jl

One feature of TBG is the hybridization of electronic bands between the two different layers. As the twist angle gets smaller, such hybridization gets stronger. This can be illustrated by applying an inter-layer bias $V(P_1 - P_2)$ to TBG, where V is the strength of the bias and $P_{1,2}$ is the projection operator on layers 1 and 2. The layer operator $L = P_1 - P_2$ allows us to analyze the layer polarization of the bands. As is shown in Fig.5.2, the low-energy bands remain layer-polarized at a large twist angle, but becomes completely layer-mixed at a small twist angle.

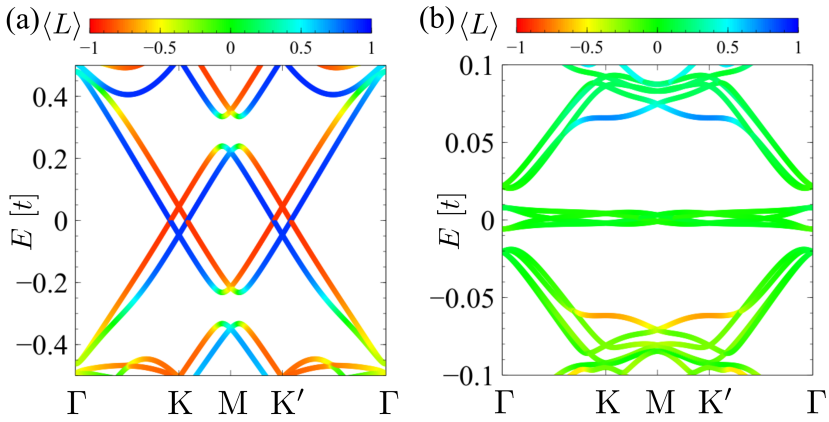

Figure 5.2. band structure of TBG with inter-layer bias $V = 0.1t$ at twist angle (a) $\theta = 9.43^\circ$ and (b) $\theta = 1.89^\circ$.

5.1.3 Emergent valley degrees of freedom in TBG

Source code: Twistronics.jl/examples/tbg_valley_degen/TBG_valley_degen.jl and Twistronics.jl/examples/tbg_inter-layer_bias_valley/TBG_inter-layer_bias_valley.jl

One important feature of TBG is the emergent valley degrees of freedom for low-energy bands at small twist angles. The two valleys are degenerate along Γ-K-M-K′-Γ. To reveal this degeneracy, we add a small valley potential to the Hamiltonian. This shifts the bands from different valleys (Fig.5.3(a)). Interestingly, inter-layer bias is known to lift up the valley degeneracy along Γ-K-M-K′-Γ in TBG [95], this is illustrated in Fig.5.3(b).

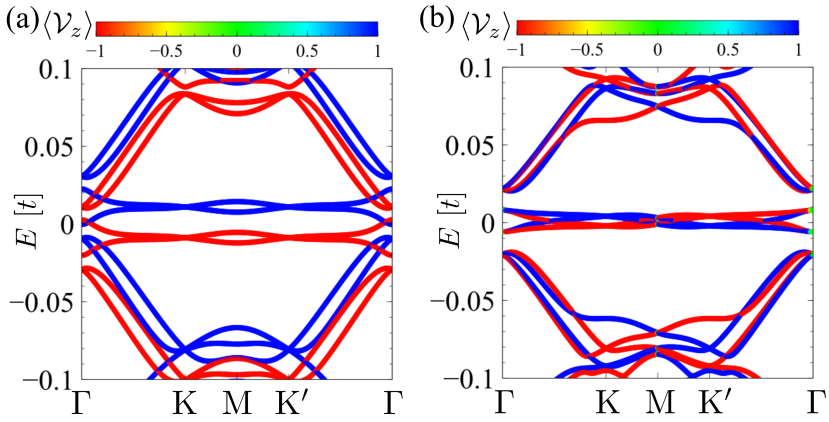

Figure 5.3. (a) band structure of TBG with a small valley potential $0.05\mathcal{V}_z$. (b) band structure of TBG with an inter-layer bias $V = 0.1t$. The color indicates the valley polarization.

5.1.4 Twisted π-flux model

Source code: Twistronics.jl/examples/Twisted_Dirac_QSL/TBQSL.jl

Twistronics.jl also allows to study band structures of twisted systems beyond TBG, such as the twisted π-flux model [44, 45] as shown in Fig.5.4.

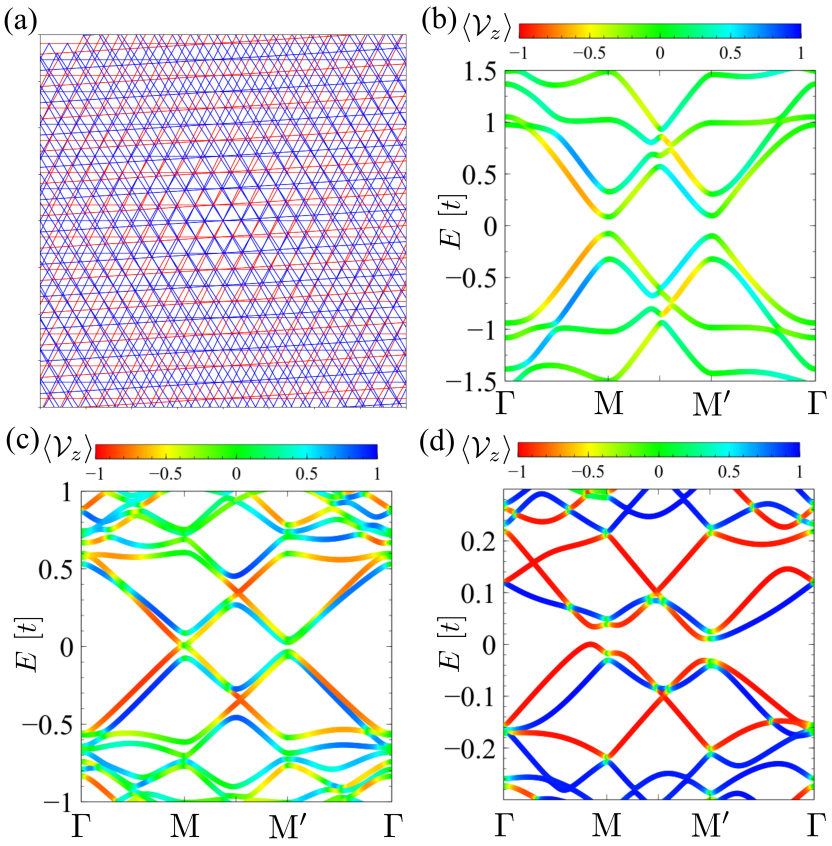

Figure 5.4. (a) Part of the supercell of the twisted π-flux model at twist angle 3.48° under a fixed gauge. (b)-(d) band structure of the twisted π-flux model at twist angle (b) $\theta = 21.79^\circ$, (c) $\theta = 9.43^\circ$ and (d) $\theta = 3.48^\circ$.

5.2 NHKPM.jl

The NHKPM.jl is a library built upon the non-Hermitian kernel polynomial method (NHKPM) [258] that we will explain in detail in Sec.6.3. This library features computing (local) spectral functions in NH systems, with a highlight of power-law scaling for spectral functions in NH many-body systems, that would allow to tackle large-size NH many-body systems beyond the capability of exact diagonalization (ED). The library can be downloaded

from my repository https://github.com/GUANGZECHEN/NHKPM.jl.

5.2.1 Non-interacting models

Non-interacting NH systems are computationally simple and can be tackled with conventional methods such as exact diagonalization (ED). We show the computation of spectral functions with NHKPM for these systems as a benchmark. In particular, we show that the spectral function:

$$\rho_{\text{tot}}(\omega) = \sum_i \langle i|\delta^2(\omega - H)|i\rangle \tag{5.1}$$

where $|i\rangle$ forms a complete basis provides the total spectrum of the Hamiltonian. In addition, we show that the spectral function computed on a local basis can reveal topological boundary modes:

$$\rho_{\text{L}}(E, l) = \left| \int dy \langle l|\delta^2(E + iy - H)|l\rangle \right|. \tag{5.2}$$

We illustrate these with some paradigmatic non-Hermitian models.

Hatano-Nelson model

Source code: NHKPM.jl/examples/NH_single_particle/Hatano/

We compute the spectrum of the Hatano-Nelson model [259]:

$$H_{\text{HN}} = \sum_{l=1}^{L-1} (t+\gamma) c_l^\dagger c_{l+1} + (t-\gamma) c_{l+1}^\dagger c_l, \tag{5.3}$$

with $L = 20$. The PBC and OBC spectra are computed both with NHKPM and ED (Fig.5.5).

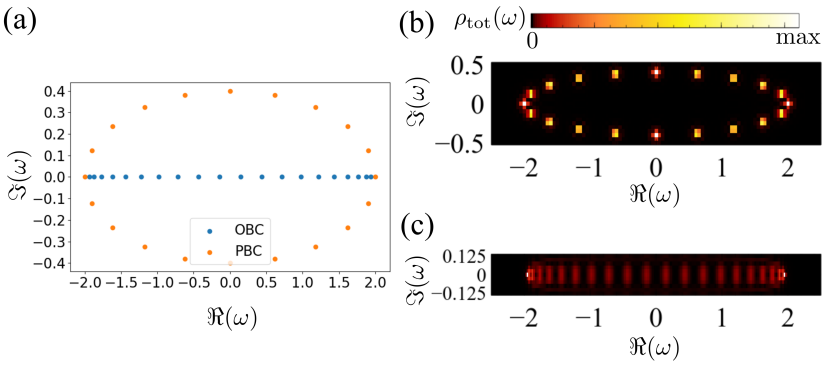

Figure 5.5. (a) Spectrum of the Hatano-Nelson model under OBC and PBC, computed with ED (b,c) tDOS for PBC and OBC. Parameter: $\gamma = 0.2$.

Asymmetric SSH model

Source code: NHKPM.jl/examples/NH_single_particle/asymmetric_SSH/

We consider the asymmetric SSH model [236]:

$$H = \sum_{l=1}^{N/2-1} \Big((t_1+\gamma/2)c_{2l-1}^\dagger c_{2l} + (t_1-\gamma/2)c_{2l}^\dagger c_{2l-1} + t_2(c_{2l}^\dagger c_{2l+1} + c_{2l+1}^\dagger c_{2l}) \Big) \\ + (t_1+\gamma/2)c_{N-1}^\dagger c_N + (t_1-\gamma/2)c_N^\dagger c_{N-1}, \tag{5.4}$$

which is a model used in the study of the influence of NHSE on bulk-boundary correspondence. It was found that in some parameter regime the PBC spectrum does not have a line gap, whereas the OBC spectrum still shows topological zero modes. Below we show the spectral functions of this model computed with NHKPM under both OBC and PBC in several parameter regimes. The results are in agreement with the spectrum obtained with exact diagonalization.

We first illustrate the gapped, topologically trivial region in Fig.5.6, where the PBC spectrum shows two rings separated by a line gap, and the OBC spectrum does not show in-gap states.

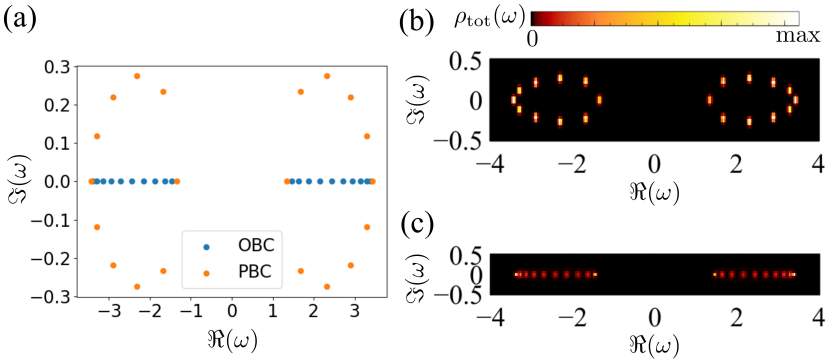

Figure 5.6. (a) Spectrum of the asymmetric SSH model computed with ED. (b,c) Total spectral function $\rho_{\rm tot}(\omega)$ computed for the model under PBC and OBC. Parameters: $t_1 = 2.5$, $t_2 = 1$, $\gamma = 0.2$ and $N = 20$.

We then show the gapless, topologically non-trivial region in Fig.5.7, where the PBC spectrum is a single ring without a gap. The local spectral function $\rho_{\rm L}(E, l)$ computed under OBC indicates the existence of 2 boundary modes near zero energy, which are the topological boundary modes in this case.

We finally show the gapped, topologically non-trivial region in Fig.5.8, where the PBC spectrum hosts a line gap. In addition, the OBC spectrum shows a PT-symmetry breaking and the eigenvalues are no longer real. The local spectral function shows the topological zero modes in this case.

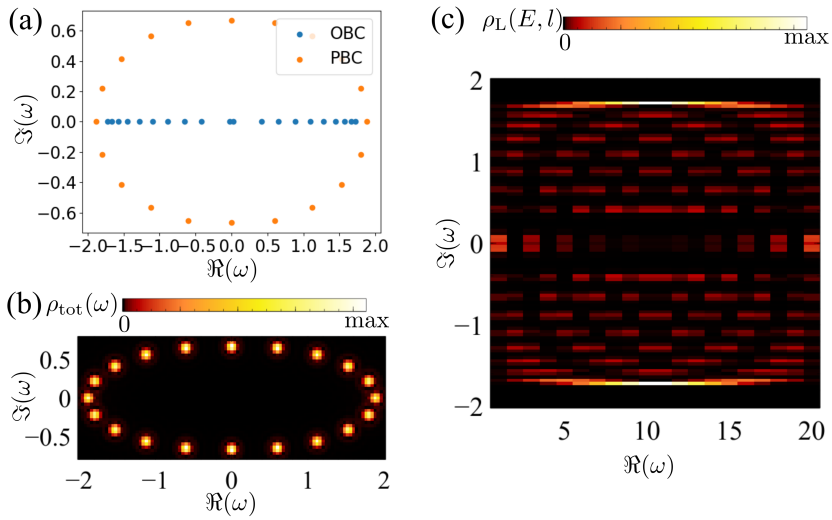

Figure 5.7. (a) Spectrum of the asymmetric SSH model computed with ED. (b) Total spectral function $\rho_{\mathrm{tot}}(\omega)$ computed for the model under PBC. (c) Local spectral function $\rho_{\mathrm{L}}(E,l)$ computed under OBC. Parameters: $t_1 = 1$, $t_2 = 1$, $\gamma = 0.2$ and $N = 20$.

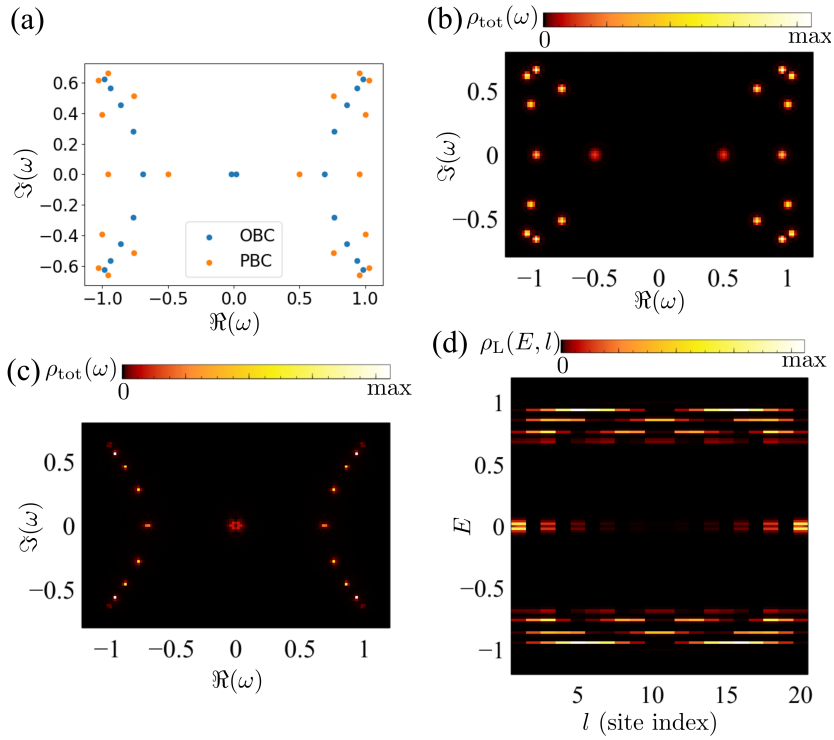

Figure 5.8. (a) Spectrum of the asymmetric SSH model computed with ED. (b,c) Total spectral function $\rho_{\mathrm{tot}}(\omega)$ computed for the model under PBC and OBC. (d) Local spectral function $\rho_{\mathrm{L}}(E,l)$ computed under OBC. Parameters: $t_1 = 1/6$, $t_2 = 1$, $\gamma = 0.2$ and $N = 20$.

A model with a topologically nontrivial line gap induced by an NH term

NHKPM.jl/examples/NH_single_particle/Hidden_Chern/

We consider the following model [255, 256]:

$$H = \sum_{l=1}^{L-1} t(c_l^\dagger c_{l+1} + c_{l+1}^\dagger c_l) + \sum_{l=1}^{L} i u_l c_l^\dagger c_l \tag{5.5}$$

where $u_l = -u$ if $l \mod 4 = 2, 3$. This model hosts a topologically nontrivial line gap for $u \neq 0$, we show the spectral functions in this regime in Fig.5.9. In particular, the local spectral function indicates the existence of topologically zero modes.

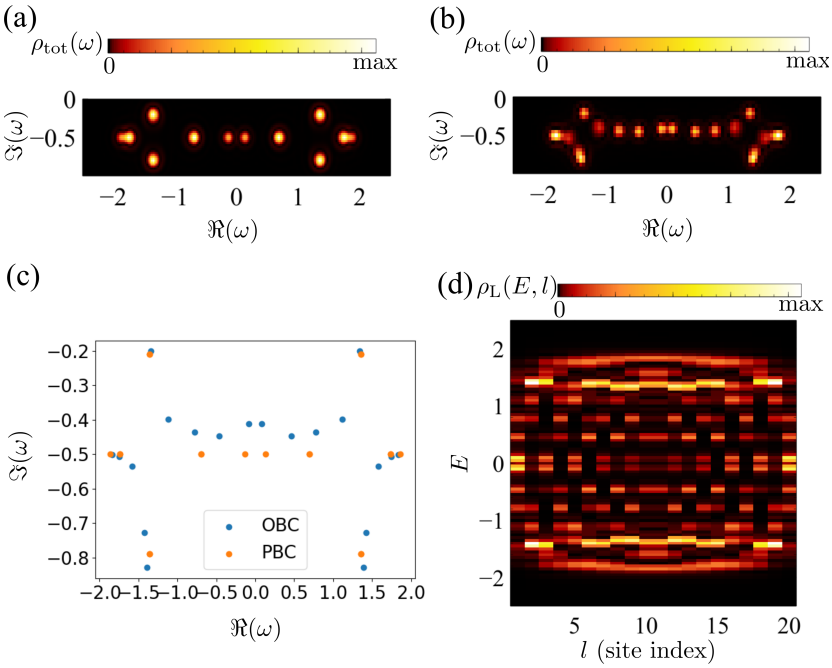

Figure 5.9. (a,b) Total spectral function $\rho_{\rm tot}(\omega)$ computed for the model Eq. (5.5) under PBC and OBC. (c) Spectrum of the model under PBC and OBC. (d) Local spectral function $\rho_{\rm L}(E, l)$ computed under OBC. Parameters: $t = 1$, $u = 1$ and $N = 20$.

2D model with NHSE

Source code: NHKPM.jl/examples/NH_single_particle/2D_skin/

We study the 2D version of the Hatano-Nelson model:

$$
\begin{aligned}
H = &\sum_{l=1}^{L-1}\sum_{m=1}^{L-1}\Big((t+\gamma)(c^{\dagger}_{l,m}c_{l+1,m}+c^{\dagger}_{l,m}c_{l,m+1})+(t-\gamma)(c^{\dagger}_{l+1,m}c_{l,m}+c^{\dagger}_{l,m+1}c_{l,m})\Big)\\
&+\sum_{l=1}^{L-1}\Big((t+\gamma)c^{\dagger}_{l,L}c_{l+1,L}+(t-\gamma)c^{\dagger}_{l+1,L}c_{l,L}\Big)\\
&+\sum_{m=1}^{L-1}\Big((t+\gamma)c^{\dagger}_{L,m}c_{L,m+1}+(t-\gamma)c^{\dagger}_{L,m+1}c_{L,m}\Big).
\end{aligned}
\tag{5.6}
$$

This model also has NHSE that the bulk states get localized under OBC. However, unlike the 1D case, the NHSE here is not related to a point gap: there does not exist a point gap in the spectrum under PBC in the thermal dynamic limit. In Fig.5.10 we show the spectrum computed for this model.

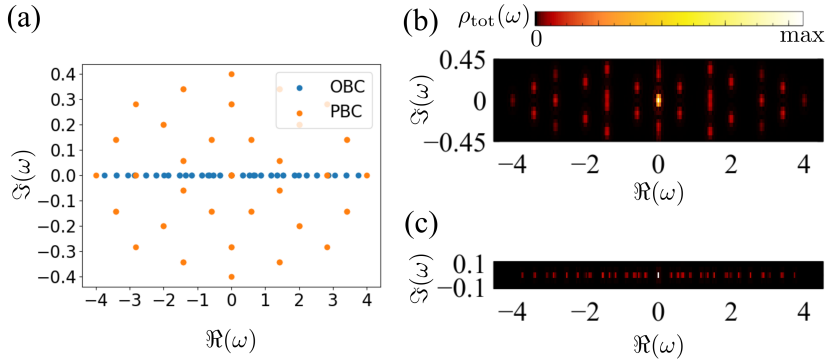

Figure 5.10. (a) Spectrum of the 2D Hatano-Nelson model computed with ED. (b,c) Total spectral function $\rho_{\rm tot}(\omega)$ computed for the model under PBC and OBC. Parameters: $t=1$, $\gamma=0.1$ and $L=8$.

5.2.2 Interacting models

In this subsection we show how the spectral functions computed with NHKPM allows to address interacting non-Hermitian models, where we utilize the MPS representation of the states. We note that the computations for interacting NH models can be time-consuming, and it is recommended to utilize parallel computation for spectral functions at different energies ω.

NH Many-body topology

Source code: NHKPM.jl/examples/NH_manybody/topology/

The two source codes "get_eigs_Krylov.jl" and "DOS.jl" would allow to compute the spectral functions shown in Sec.4.3. First, the ground state is computed with the Krylov-Schur method [260] in "get_eigs_Krylov.jl",

where the parameters of the Hamiltonian in Eq.(4.32) can be modified inside the script. The script will generate a ".jls" file containing information about the Hamiltonian and its left/right ground states and corresponding energies. Then, using this ".jls" file as input, we can compute spectral functions of the Hamiltonian using the script "DOS.jl".

Correlators in a Liouvillian

Source code: NHKPM.jl/examples/NH_manybody/Liouvillian/Liouvillian.jl

To this end, let us present the implementation of NHKPM to figure out the correlators in a Liouvillian instead of characterizing NH topology. We shall see that correlators in the frequency domain computed with NHKPM allow to predict the decay rate of perturbations above the steady state. We consider the Liouvillian:

$$\frac{d}{dt}\rho(t) = \mathcal{L}[\rho(t)] = -i[H,\rho(t)] + \sum_{l=1}^{N}\left(L_l\rho(t)L_l^\dagger - \frac{1}{2}\{L_l^\dagger L_l, \rho(t)\}\right) \tag{5.7}$$

with

$$H = -\sum_{l=1}^{N/2} J_x\sigma_{2i-1}^x\sigma_{2i}^x - \sum_{l=1}^{N/2-1} J_y\sigma_{2i}^y\sigma_{2i+1}^y \tag{5.8}$$

and $L_l = \sqrt{\gamma}\sigma_l^z$ [261]. Vectorizing the density matrix ρ as we did for Eq. (4.19), the Liouvillian can be expressed as

$$\tilde{\mathcal{L}} = -iH\otimes\mathbf{I} + i\mathbf{I}\otimes H + \sum_{l=1}^{N}\gamma\sigma_l^z\otimes\tau_l^z - \gamma N \tag{5.9}$$

with H given by Eq. (5.8) and we used the fact that $H = H^T$. This Liouvillian has 2 steady states $\rho_\pm = (\mathbf{I}\pm Q)/2^N$ where $Q = \prod_l \sigma_l^z$ is a conserved charge. For simplicity we assume $\rho_s = I/2^N$ to be the steady state, which is true when a small magnetic field is applied in x direction.

The time-evolution of a perturbation O above the steady state is given by:

$$C(t) = \mathbf{tr}(O(t)O\rho_s) = \mathbf{tr}(e^{t\mathcal{L}^*}[O]O\rho_s) = \mathbf{tr}(Oe^{t\mathcal{L}}[O\rho_s]) \tag{5.10}$$

where $\mathcal{L}^*$ is the adjoint operator of $\mathcal{L}$. In the vectorized form, Eq. (5.10) reads:

$$C(t) = \langle\mathbf{I}|O\otimes\mathbf{I}e^{t\tilde{\mathcal{L}}}O\otimes\mathbf{I}|\tilde{\rho}_s\rangle \tag{5.11}$$

where $|\mathbf{I}\rangle = \sum_n |n\rangle|n\rangle$ is the vectorized form of the identity matrix. We have used $\mathbf{tr}(A) = \langle\mathbf{I}|\tilde{A}\rangle$ and $A\rho B = A\otimes B^T|\tilde{\rho}\rangle$ [261] in deriving Eq. (5.11). Performing a Fourier transform on Eq. (5.11), we have:

$$C(t) = \int d^2\omega e^{\omega t}C(\omega) \tag{5.12}$$

up to a renormalization factor, where the correlator $C(\omega)$ is given by

$$C(\omega) = \langle \mathbf{I}|O \otimes \mathbf{I}\delta^2(\omega - \tilde{\mathcal{L}})O \otimes \mathbf{I}|\tilde{\rho}_s\rangle \tag{5.13}$$

and can be computed with NHKPM. We show the computation for this correlator with $O = \sigma_1^z$ and $N = 10$. As the Hilbert space is of dimension 2^{20} in this case, we use MPS representation for $|\tilde{\rho}_s\rangle = |\mathbf{I}\rangle$. The results are shown in Fig.5.11, where the largest real value in the computed spectrum indicates the inverse life time of the perturbation. We see that for $J_x = 0.5$ and $J_y = 1$, when the model is topological, the perturbation has a long lifetime even in the presence of large dissipation $\gamma = 0.5$ (Fig.5.11(a)). Whereas in the topologically trivial regime $J_x = 1$ and $J_y = 0.5$, the perturbation is not protected and decays faster as γ increases. The results agree with Ref. [261].

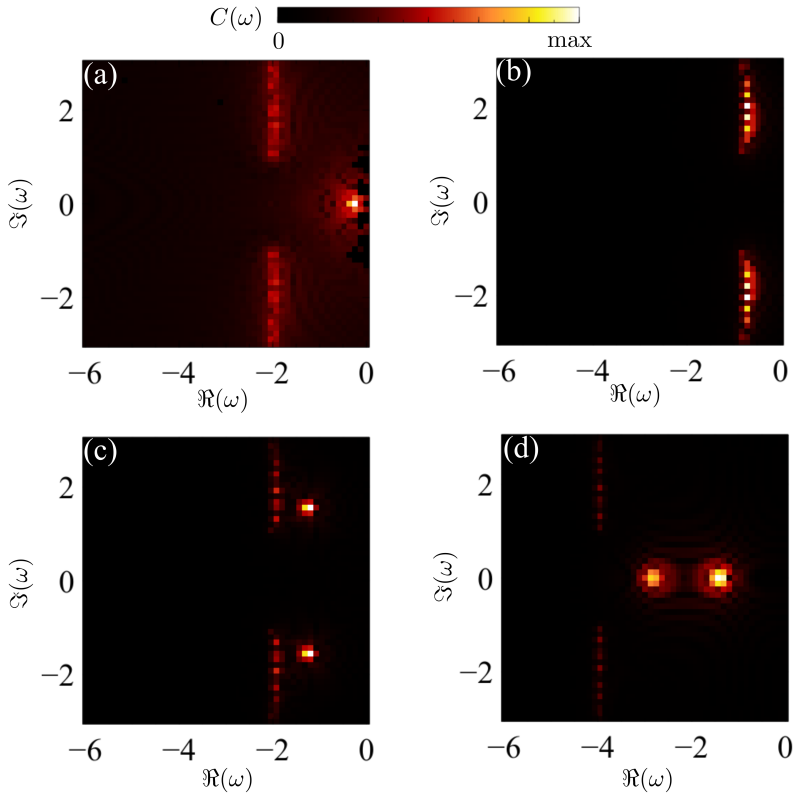

Figure 5.11. Correlator $C(\omega)$ in Eq. (5.13) computed for the Liouvillian Eq. (5.9) with $O = \sigma_1^z$ and $N = 10$ and (a) $J_x = 0.5, J_y = 1$ and $\gamma = 0.5$, (b) $J_x = 1, J_y = 0.5$ and $\gamma = 0.2$, (c) $J_x = 1, J_y = 0.5$ and $\gamma = 0.5$ and (d) $J_x = 1, J_y = 0.5$ and $\gamma = 1$.

6. Methods

We summarize the methods used in this thesis in this chapter.

6.1 Green's function embedding method

The Green's function embedding method [66, 262, 263] is a method to compute local spectral function in an inhomogeneous infinite system. We utilize it to compute the local density of states (LDOS) near an impurity site in an infinitely large lattice. The essence of this method is as follows.

For a unit cell containing the impurity, the Green's function in this unit cell can be written using Dyson's equation as:

$$G(\omega) = (\omega - H' - \Sigma(\omega))^{-1}, \tag{6.1}$$

where H' is the Hamiltonian of the unit cell and $\Sigma(\omega)$ is the self-energy due to the coupling of the unit cell to the rest of the infinite pristine system. The impurity does not influence $\Sigma(\omega)$ since it does not change the hoppings that couple the unit cell to the rest of the system. Therefore, in the absence of the impurity, the Green's function of the pristine unit cell coupled to the infinite system is:

$$G_0(\omega) = (\omega - H_0 - \Sigma(\omega))^{-1}, \tag{6.2}$$

where H_0 is the Hamiltonian of the pristine unit cell. Since the whole system is now pristine, this Green's function can also be computed by:

$$G_0(\omega) = \frac{1}{(2\pi)^2} \int d^2\mathbf{k} (\omega - H_\mathbf{k} - i0^+)^{-1}, \tag{6.3}$$

where $H_\mathbf{k}$ is the Bloch Hamiltonian associated to H_0 on this unit cell. Using Eq.(6.2), the self-energy can be computed as $\Sigma(\omega) = \omega - H_0 - G_0^{-1}(\omega)$, and the Green's function of the defective unit cell can be solved with Eq.(6.1). The DOS in the unitcell is thus $\rho(\omega) = -\frac{1}{\pi} \operatorname{Im} G(\omega)$.

6.2 The Krylov-Schur algorithm

The Krylov-Schur algorithm [260] is a method to solve extreme eigenvalues of a non-Hermitian matrix. The core of the Krylov-Schur algorithm is the Krylov decomposition of a matrix A:

$$AU_k = U_k B_k + u_{k+1} b_{k+1}^\dagger \tag{6.4}$$

where $U_k = (u_1, u_2, \ldots, u_k)$ with $\{u_i\}$ being a set of linearly-independent vectors. $B_k = V_k^\dagger A U_k$ is called the Rayleigh quotient where $V_k^\dagger$ is the left inverse of U_k. In particular, if we require $\{u_i\}$ to be an orthogonal set of vectors, the Krylov decomposition reduces to the Lanczos decomposition for a Hermitian matrix A and the Arnoldi decomposition for a non-Hermitian matrix A, which are building blocks of the Lanczos and Arnoldi algorithms, respectively. The lifted restriction on the orthogonality of $\{u_i\}$ allows the Krylov-Schur algorithm to be more efficient than the Arnoldi algorithm [260].

The Krylov-Schur algorithm relies on (i) initializing a Krylov decomposition of A with a random vector x, then performing (ii) a truncation to obtain a Krylov subspace of our interest, and (iii) a re-expansion successively until convergence.

The initialization of a Krylov decomposition on the Krylov subspace $\{x, Ax, \ldots, A^{j-1}x\}$ can be done with the Gram-Schmidt method. The Krylov decomposition of A on this subspace is given by the m-step Arnoldi algorithm:

$$\begin{aligned}
&u_1 = \frac{x}{||x||} \\
&\textbf{for} \quad j = 1 : m \\
&\qquad r = A u_j \\
&\qquad \textbf{for} \quad i = 1 : j \\
&\qquad\qquad B_{ij} = u_i^\dagger r \\
&\qquad\qquad r = r - B_{ij} u_i \\
&\qquad \textbf{end} \\
&\qquad B_{j+1,j} = ||r|| \\
&\qquad u_{j+1} = \frac{r}{B_{j+1,j}} \\
&\textbf{end}
\end{aligned} \tag{6.5}$$

which gives $AU_m = U_m B_m + u_{m+1} b_{m+1}^\dagger$.

We then truncate the above Krylov decomposition to the subspace of our interest by first performing a unitary transformation Z_1 to B_m to make it upper triangle $T_m = Z_1^\dagger B_m Z_1$. This is also known as Schur decomposition, and the orthogonal elements of T_m are called Schur values. We then move the Schur values of our interest (for example, the smallest real Schur values) to the top-left corner of T_m with another unitary transformation Z_2: $\tilde{T}_m = Z_2^\dagger T_m Z_2$. Let $Z = Z_1 Z_2$, we have

$$A(U_m Z) = (U_m Z)\tilde{T}_m + u_{m+1} b_{m+1}^\dagger Z. \tag{6.6}$$

Keeping the first k columns of 6.6 would give us the Krylov decomposition in the truncated Krylov subspace of our interest:

$$A(U_m Z)_k = (U_m Z)_k (\tilde{T}_m)_k + u_{m+1}(b_{m+1}^\dagger Z)_k \tag{6.7}$$

where $(U_m Z)_k$ refers to the truncated matrix keeping the first k columns of $U_m Z$.

Finally, the expansion of the Krylov decomposition Eq. (6.7) can be done by applying Eq. (6.5) taking $x = u_k$, where u_k is the kth column of $(U_m Z)_k$.

We note that the operations on A and $\{u_i\}$ in the Krylov-Schur algorithm involve only (i) Au_i in Eq. (6.5)and (ii) linear combinations of u_i in Eq. (6.6). This fact essentially allows the Krylov-Schur algorithm to be performed with MPO representation of A and MPS representation of u_i.

6.3 The Kernel Polynomial Method

The kernel polynomial method (KPM) [264] is a method to efficiently compute spectral functions for Hermitian Hamiltonians:

$$\rho(E) = \langle \psi_L | \delta(E - H_0) | \psi_R \rangle \tag{6.8}$$

where $|\psi_{L,R}\rangle$ are arbitrary states. Since the eigenvalues of H_0 are bounded, we can perform a shifting and a rescaling on H_0 such that the eigenvalues lie in $[0, 1)$. In such case, $\rho(E \in [0, 1), l)$ is a bounded single-variable function for fixed l, which is a crucial property that allows it to be expanded in Chebyshev polynomials $T_n(E) = \cos(n \arccos E)$:

$$\rho(E, l) = \frac{1}{\pi\sqrt{1 - E^2}} \left(\mu_0 + 2 \sum_{n=1}^{\infty} \mu_n T_n(E) \right) \tag{6.9}$$

where the coefficients satisfy $\mu_n = \int_{-1}^{1} \mathrm{d}E \rho(E) T_n(E) = \langle \psi_L | T_n(H_0) | \psi_R \rangle$. Using the recursion relation of Chebyshev polynomials: $T_{n+1}(x) = 2xT_n(x) -$

$T_{n-1}(x)$, μ_n can be computed as $\mu_n = \langle\psi_L|v_n\rangle$ with

$$\begin{aligned} |v_{n+1}\rangle &= 2H_0|v_n\rangle - |v_{n-1}\rangle \\ |v_0\rangle &= |\psi_R\rangle, |v_1\rangle = H_0|\psi_R\rangle. \end{aligned} \tag{6.10}$$

The recursive structure of Eq. (6.10) allows the efficient computation of μ_n and $\rho(E)$. Finally, Eq. (6.9) is approximated with a truncation of the summation to N^{th} order, where a Jackson kernel

$$g_n^N = \frac{(N-n+1)\cos\frac{n\pi}{N+1} + \sin\frac{n\pi}{N+1}\cot\frac{\pi}{N+1}}{N+1} \tag{6.11}$$

is multiplied to the coefficients μ_n to damp Gibbs oscillations [264].

We would like to note that Eq. (6.10) essentially involves only operations of $H_0|v_n\rangle$ and linear combinations of vectors. This allows the KPM to be implemented with MPS representation of $|\psi_{L,R}\rangle$.

6.4 The Non-Hermitian Kernel Polynomial Method

The Non-Hermitian Kernel Polynomial Method (NHKPM) [258] is a method to efficiently compute generic spectral functions of a non-Hermitian Hamiltonian H:

$$f(\omega) = \langle\psi_{\mathrm{L}}|\delta^2(\omega - H)|\psi_{\mathrm{R}}\rangle \tag{6.12}$$

where $|\psi_{\mathrm{L}}\rangle, |\psi_{\mathrm{R}}\rangle$ are arbitrary states. We summarize the essence of this method below.[1]

The key observation is, although Eq. (6.12) cannot be computed with KPM directly [265], it can be related to the spectral functions of the Hermitized form of $\omega - H$:

$$\mathcal{H} = \begin{pmatrix} & \omega - H \\ \omega^* - H^\dagger & \end{pmatrix}. \tag{6.13}$$

In particular, using $\partial_{\omega^*}(1/\omega) = \pi\delta(\mathrm{Re}(\omega))\delta(\mathrm{Im}(\omega))$ [266], we can rewrite Eq. (6.12) as

$$f(\omega) = \frac{1}{\pi}\partial_{\omega^*}G(E=0) \tag{6.14}$$

where $G(E) = \langle\mathrm{L}|(E-\mathcal{H})^{-1}|\mathrm{R}\rangle$ is the Green's function of $\mathcal{H}$ with $|\mathrm{L}\rangle = \begin{pmatrix} 0 \\ |\psi_{\mathrm{L}}\rangle \end{pmatrix}$ and $|\mathrm{R}\rangle = \begin{pmatrix} |\psi_{\mathrm{R}}\rangle \\ 0 \end{pmatrix}$. Since $\mathcal{H}$ is Hermitian, its Green's function

[1] The rest of this section is adapted from G. Chen, F. Song and J. L. Lado, Phys. Rev. Lett. 130, 100401 with revisions.

$G(E)$ has the Chebyshev expansion Eq. (6.9), resulting in an expansion of $f(\omega)$ in Chebyshev polynomials of $\mathcal{H}$:

$$f(\omega) = \frac{2}{\pi^2} \sum_{n=1}^{\infty} (-1)^{n+1} \langle \mathrm{L} | \partial_{\omega^*} T_{2n-1}(\mathcal{H}) | \mathrm{R} \rangle \tag{6.15}$$

with the recursion relation

$$\partial_{\omega^*} T_{n+1}(\mathcal{H}) = 2 \begin{pmatrix} 0 & 0 \\ 1 & 0 \end{pmatrix} T_n(\mathcal{H}) + 2\mathcal{H} \partial_{\omega^*} T_n(\mathcal{H}) - \partial_{\omega^*} T_{n-1}(\mathcal{H}). \tag{6.16}$$

Finally, the above recursion relation on $T_n(\mathcal{H})$ is transformed into an update of vectors, similar to Eq. (6.10), allowing $f(\omega)$ to be computed with KPM. We note that similar to KPM, the NHKPM can also be implemented with MPS representation of states. The details of this method are explained in the following subsections.

6.4.1 Technical details of NHKPM

We derived in the last section that the spectral function

$$f(\omega) = \langle \psi_{\mathrm{L}} | \delta^2(\omega - H) | \psi_{\mathrm{R}} \rangle \tag{6.17}$$

can be computed with

$$f(\omega) = \frac{1}{\pi} \partial_{\omega^*} G(E = 0) \tag{6.18}$$

where

$$G(E) = \langle \mathrm{L} | (E - \mathcal{H})^{-1} | \mathrm{R} \rangle \tag{6.19}$$

is an entry of the Green's function of the Hermitized Hamiltonian $\mathcal{H}$ in Eq. (6.13) with

$$|\mathrm{L}\rangle = \begin{pmatrix} 0 \\ |\psi_{\mathrm{L}}\rangle \end{pmatrix}, |\mathrm{R}\rangle = \begin{pmatrix} |\psi_{\mathrm{R}}\rangle \\ 0 \end{pmatrix}. \tag{6.20}$$

Since $G(E)$ is a function of a single variable, we can apply KPM to compute $G(E)$, let

$$G(E) = B(E) - iA(E), \tag{6.21}$$

where $A(E) = \langle \mathrm{L} | \delta(E - \mathcal{H}) | \mathrm{R} \rangle$ and $B(E)$ is its Hilbert transform:

$$B(E) = \frac{1}{\pi} \mathcal{P} \int_{-\infty}^{\infty} \mathrm{d}E' \frac{A(E')}{E - E'}, \tag{6.22}$$

where $\mathcal{P}$ denotes the Cauchy principal value. Performing a scaling on $\mathcal{H}$: $\mathcal{H} \to \mathcal{H}/\Delta$ such that its spectrum lies in $(-1,1)$, we can perform a Chebyshev expansion on $A(E)$[2]:

$$A(E) = \frac{1}{\pi\sqrt{1-E^2}}\left(\mu_0 + 2\sum_{n=1}^{\infty}\mu_n T_n(E)\right), \tag{6.23}$$

where

$$\mu_n = \int_{-1}^{1} \mathrm{d}E A(E) T_n(E) = \langle \mathbf{L}|T_n(\mathcal{H})|\mathbf{R}\rangle, \tag{6.24}$$

and $T_n(x) = \cos(n \arccos x)$ satisfying the following recursion relation:

$$\begin{aligned} T_0(x) = 1, T_1(x) = x, \\ T_{n+1}(x) = 2xT_n(x) - T_{n-1}(x). \end{aligned} \tag{6.25}$$

Using

$$\mathcal{P}\int_{-1}^{1} \frac{T_n(y)\mathrm{d}y}{(y-x)\sqrt{1-y^2}} = \pi U_{n-1}(x), \tag{6.26}$$

together with Eqs. (6.22) and (6.23), we have

$$B(E) = \frac{2}{\pi}\sum_{n=1}^{\infty}\mu_n U_{n-1}(E) \tag{6.27}$$

where $U_n(x) = \sin[(n+1)\arccos x]/\sin[\arccos x]$. Combining Eqs. (6.21),(6.23) and (6.27), we have

$$G(E=0) = \frac{2}{\pi}\sum_{n=1}^{\infty}(-1)^{n+1}\mu_{2n-1}, \tag{6.28}$$

which can be computed by noting that $\mu_n = 0$ for even n and $T_n(0) = U_n(0) = 0$ for odd n. Combining Eq. (6.18), Eq. (6.24) and Eq. (6.28), we have

$$f(\omega) = \frac{2}{\pi^2}\sum_{n=1}^{\infty}(-1)^{n+1}\langle \mathbf{L}|\partial_{\omega^*} T_{2n-1}(\mathcal{H})|\mathbf{R}\rangle, \tag{6.29}$$

with the recursion relation

$$\partial_{\omega^*} T_{n+1}(\mathcal{H}) = 2\begin{pmatrix} & 0 \\ 1 & \end{pmatrix} T_n(\mathcal{H}) + 2\mathcal{H}\partial_{\omega^*} T_n(\mathcal{H}) - \partial_{\omega^*} T_{n-1}(\mathcal{H}). \tag{6.30}$$

We now elaborate on the numerical details in the computation of $f(\omega)$. Let

$$|A_n\rangle = T_n(\mathcal{H})|\mathbf{R}\rangle \tag{6.31}$$

[2]Although $A(E)$ is a complex-valued function, we can do Chebyshev expansion for its real and imaginary parts, respectively, then adding up the coefficients to get Eq. (6.23)

and

$$|\Psi_n\rangle = \partial_{\omega^*} T_n(\mathcal{H})|\mathrm{R}\rangle. \tag{6.32}$$

We can verify that

$$\begin{aligned} |A_0\rangle &= \begin{pmatrix} |\psi_{\mathrm{R}}\rangle \\ 0 \end{pmatrix}, |A_1\rangle = \begin{pmatrix} 0 \\ (\omega^* - H^\dagger)|\psi_{\mathrm{R}}\rangle \end{pmatrix} \\ |\Psi_0\rangle &= \begin{pmatrix} 0 \\ 0 \end{pmatrix}, |\Psi_1\rangle = \begin{pmatrix} 0 \\ |\psi_{\mathrm{R}}\rangle \end{pmatrix} \end{aligned} \tag{6.33}$$

with recursion relation

$$\begin{aligned} |A_{n+1}\rangle &= 2\mathcal{H}|A_n\rangle - |A_{n-1}\rangle \\ |\Psi_{n+1}\rangle &= 2\begin{pmatrix} 0 \\ 1 \end{pmatrix}|A_n\rangle + 2\mathcal{H}|\Psi_n\rangle - |\Psi_{n-1}\rangle. \end{aligned} \tag{6.34}$$

Let

$$\begin{aligned} |A_{2n}\rangle &= \begin{pmatrix} |\alpha_{2n}\rangle \\ 0 \end{pmatrix}, |A_{2n+1}\rangle = \begin{pmatrix} 0 \\ |\alpha_{2n+1}\rangle \end{pmatrix} \\ |\Psi_{2n}\rangle &= \begin{pmatrix} |\psi_{2n}\rangle \\ 0 \end{pmatrix}, |\Psi_{2n+1}\rangle = \begin{pmatrix} 0 \\ |\psi_{2n+1}\rangle \end{pmatrix} \end{aligned} \tag{6.35}$$

where $n \in \mathbb{Z}$ and $n \geq 0$. We thus arrive at the following recursion relation

$$\begin{aligned} |\alpha_{2n}\rangle &= 2(\omega - H)|\alpha_{2n-1}\rangle - |\alpha_{2n-2}\rangle \\ |\alpha_{2n+1}\rangle &= 2(\omega^* - H^\dagger)|\alpha_{2n}\rangle - |\alpha_{2n-1}\rangle \\ |\psi_{2n}\rangle &= 2(\omega - H)|\psi_{2n-1}\rangle - |\psi_{2n-2}\rangle \\ |\psi_{2n+1}\rangle &= 2|\alpha_{2n}\rangle + 2(\omega^* - H^\dagger)|\psi_{2n}\rangle - |\psi_{2n-1}\rangle \end{aligned} \tag{6.36}$$

with

$$\begin{aligned} |\alpha_0\rangle = |\psi_{\mathrm{R}}\rangle, |\alpha_1\rangle = (\omega^* - H^\dagger)|\psi_{\mathrm{R}}\rangle \\ |\psi_0\rangle = 0, |\psi_1\rangle = |\psi_{\mathrm{R}}\rangle, \end{aligned} \tag{6.37}$$

and Eq.(6.29) becomes

$$f(\omega) = \frac{2}{\pi^2}\sum_{n=1}^{\infty}(-1)^{n+1}\langle\psi_L|\psi_{2n-1}\rangle. \tag{6.38}$$

In practice, we do a truncation of Eq. (6.38) to order N:

$$f_{\mathrm{KPM}}(\omega) = \frac{2}{\pi^2}\sum_{n=1}^{N}(-1)^{n+1} g_{2n-1}^{2N}\langle\psi_L|\psi_{2n-1}\rangle. \tag{6.39}$$

where

$$g_n^{2N} = \frac{(2N-n+1)\cos\frac{n\pi}{2N+1} + \sin\frac{n\pi}{2N+1}\cot\frac{\pi}{2N+1}}{2N+1} \tag{6.40}$$

is the Jackson kernel to suppress Gibbs oscillations and improve the accuracy [264]. We note that Eq. (6.39) can also be written as:

$$f_{\text{KPM}}(\omega) = \frac{1}{\pi}\partial_{\omega^*} G_{\text{KPM}}(E=0) \tag{6.41}$$

where

$$G_{\text{KPM}}(E=0) = \frac{2}{\pi}\sum_{n=1}^{N}(-1)^{n+1} g_{2n-1}\mu_{2n-1} \tag{6.42}$$

is a finite-series approximation to Eq. (6.28) with the Jackson kernel g_n. The truncation to the N^{th} order polynomial with a Jackson kernel is known to provide a Gaussian approximation to the Dirac delta function [264]:

$$(\delta(x))_{\text{Jackson}} \approx \frac{1}{\sqrt{2\pi\sigma^2}} e^{-\frac{x^2}{2\sigma^2}}, \tag{6.43}$$

where $\sigma = \pi/N$. Performing a Hilbert transform on both sides of Eq. (6.43), we have:

$$\left(\frac{1}{x}\right)_{\text{Jackson}} \approx \frac{2}{\sqrt{2\sigma^2}} F\left(\frac{x}{\sqrt{2\sigma^2}}\right) \tag{6.44}$$

where $F(x) = \exp\left(-x^2\right)\int_0^x \exp\left(t^2\right)dt$ is the Dawson function [267]. Eq. (6.44) provides a good approximation for $1/x$ for $x \gtrsim 2\sigma$. Now, for $G(E=0)$, the KPM procedure provides an approximation:

$$\begin{aligned} G(E=0) &= -\langle \mathbf{L}|\mathcal{H}^{-1}|\mathbf{R}\rangle \\ &= -\sum_n \langle \mathbf{L}|\varphi_n\rangle \mathcal{E}_n^{-1}\langle\varphi_n|\mathbf{R}\rangle \\ &\approx -\sum_n \langle \mathbf{L}|\varphi_n\rangle \left(\mathcal{E}_n^{-1}\right)_{\text{Jackson}} \langle\varphi_n|\mathbf{R}\rangle, \end{aligned} \tag{6.45}$$

where $\mathcal{E}_n$ and $|\varphi_n\rangle$ are the eigen-decomposition of $\mathcal{H}$. Eq. (6.45) is a good approximation as long as

$$\sigma \lesssim \frac{\min(\mathcal{E}_n)}{2\Delta}, \tag{6.46}$$

where Δ is the factor we divide $\mathcal{H}$ with to keep its spectrum in $(-1,1)$. A sufficiently small σ can be achieved by increasing N in our computation.

Due to the derivative in Eq. (6.18), a quantitative analysis of the approximation we did for $f(\omega)$ is difficult. Qualitatively, delta functions in $f(\omega)$ are smeared in $f_{\text{KPM}}(\omega)$ with a width $d \approx \frac{\pi\Delta}{N}$, where Δ is the scaling factor

to $\mathcal{H}$ to make its spectrum in $(-1, 1)$. For $L = 8$, $\Delta = 6$ is sufficient in our computation, and for $L = 24$, we take $\Delta = 16$.

For $L = 8$, the low-energy spectra computed with NHKPM in Fig.4.2 agree with results obtained with exact diagonalization (ED) qualitatively (Fig.6.1). An exact correspondence does not exist here since in ED the delta function is approximated with a Gaussian, whereas with NHKPM it is approximated with another peaked function as discussed above.

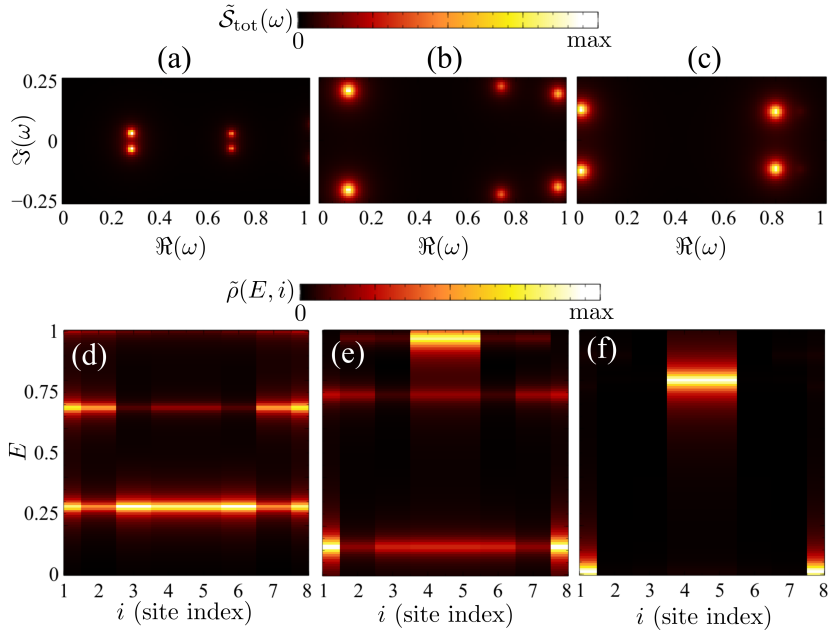

Figure 6.1. Spectral functions in Fig.4.2 computed with exact diagonalization.

6.4.2 Numerical complexity of NHKPM

We analyze the numerical complexity of the NHKPM algorithm in this section. In essence, an optimized version of the algorithm scales approximately as L^3, with L the number of sites. This power law dependence makes our algorithm scalable to bigger systems. We elaborate on the details below.

We analyze the time consumption to compute the spectral function Eq. (4.34):

$$\begin{aligned}\mathcal{S}(\omega, l) =& \langle \mathrm{GS_L} | S_l^- \delta^2(\omega + E_{\mathrm{GS}} - H) S_l^+ | \mathrm{GS_R} \rangle \\ &+ \langle \mathrm{GS_L} | S_l^+ \delta^2(\omega + E_{\mathrm{GS}} - H) S_l^- | \mathrm{GS_R} \rangle\end{aligned} \tag{6.47}$$

with NHKPM for different system size L, where H and $|\mathrm{GS_{L,R}}\rangle$ are given.

In our particular case, the Hamiltonian H is given by Eq. (4.32), and $|\mathrm{GS}_{\mathrm{L,R}}\rangle$ are computed with the Krylov-Schur algorithm. We focus on the topologically non-trivial regime: $h_z = J, \gamma = 0$, and fix $\omega = 0.23i$ and $l = 1$ as the spectral function shows a peak at this point due to the topological edge excitations. We note that the energy mesh and a sweep over all sites required to compute the full spectral function can be easily parallelized. As a result, the scaling of the algorithm is determined by the size dependence for a fixed ω and l.

We fix the broadening of the peak for the scaling analysis. As the system size increases, a larger scaling factor Δ is required to scale the spectrum of $\mathcal{H}$ into $(-1, 1)$. Thus, to ensure the same broadening, the number of polynomials N should correspondingly increase. For our specific model, Δ is proportional to L, and thus we choose $N \propto L$ for the scaling analysis.

We first analyze the scaling of our algorithm for a generic case where the bond dimension of the MPS m is fixed. In this case, the time consumption shows an approximately 3rd power dependence on the system size (Fig.6.2(a)). This scaling is the same as the kernel polynomial algorithm for Hermitian interacting systems [249].

We also analyze the scaling for our specific computation, where the entanglement entropy of states increases during the recursive calculations in the kernel polynomial method. In this case, to ensure computational accuracy, a sufficiently large m is required, which increases with L. In Fig.6.3, we show the computed spectral functions as a function of m for different sizes L. We show this for both $\omega = 0.23i$ where the spectral function is dominated at the boundary, and for $\omega = 0.8$ where the spectral function is dominated in the bulk. We observe that as m increases, the computed spectral function approaches the accurate value as expected. We also observe that although the accuracy is low for small m, it is still clear that for $\omega = 0.23i$ there exist edge excitations, and for $\omega = 0.8$ the excitations are more distributed in the bulk. Thus, a relative error of 10% is sufficient for the characterization of topological edge states. The smallest m required for this accuracy is $m = 40, 50, 60, 80$ for $L = 12, 16, 20, 24$, respectively. For simplicity, we choose $m = 10L/3$ to study the scaling, resulting in computational time $t \propto L^5$ (Fig.6.2(b)). Compared to the fixed m case, the additional power of 2 originates from the fact that the complexity of applying a matrix product operator (MPO) on an MPS is proportional to m^2, and we have used $m \propto L$ in this case.

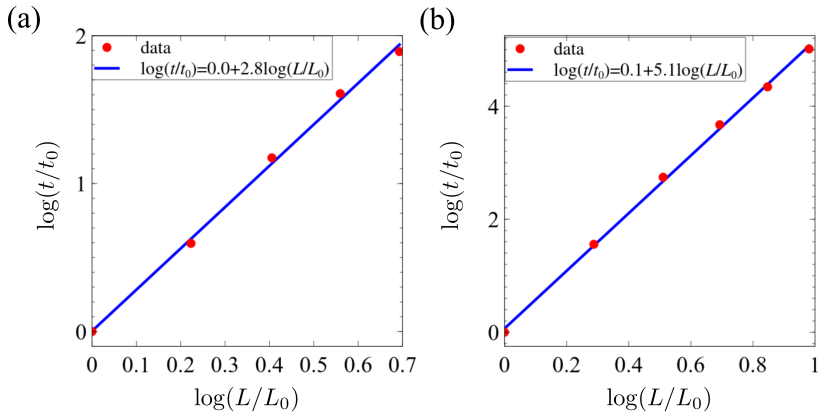

Figure 6.2. (a) Complexity of NHKPM algorithm with fixed bond dimension $m = 80$ in MPS computations and $N = 25L/2$, with $L_0 = 16$ and $t_0 = 442.9$s. The log-log data is fitted with a linear function, indicating that the complexity of the algorithm is power-law with $(t/t_0) \propto (L/L_0)^{2.8}$. (b) Complexity of NHKPM algorithm with bond dimension $m = 10L/3$ in MPS computations and $N = 25L/2$, with $L_0 = 12$ and $t_0 = 30.4$s. The log-log fit indicates a power-law complexity with $(t/t_0) \propto (L/L_0)^5$.

6.4.3 Stability of NHKPM in the presence of NHSE

In the presence of NHSE, the Hamiltonian becomes a non-normal matrix, that is $HH^\dagger \neq H^\dagger H$. Non-normal matrices have large condition numbers [268] that results in numerical instabilities. This can be illustrated with a simple 2×2 matrix:

$$M = \begin{pmatrix} & \frac{1}{x} \\ x & \end{pmatrix} \tag{6.48}$$

with $x \neq 0, 1$. The eigenvalues of M are clearly ± 1, with right eigenvectors $\frac{1}{\sqrt{1+x^2}}(1, \pm x)^T$, where T denotes the transpose. One might assume the numerical diagonalization of this matrix should be as simple and accurate. However, with smaller x, better numerical precision is required even to diagonalize this simple matrix. In fact, for $x \sim 1e300$, even though we can numerically capture the matrix M, the numeircal diagonalization of it proves wrong due to the lack of numerical accuracy.

Non-interacting limit

In the non-interacting limit, the spectrum of H in the presence of NHSE is known to be drastically different under different boundary conditions: in the thermodynamic limit, the spectrum of H is purely real under open boundary condition (OBC), and features a point gap under periodic boundary condition (PBC). On the contrary, the spectrum of the Hermitized

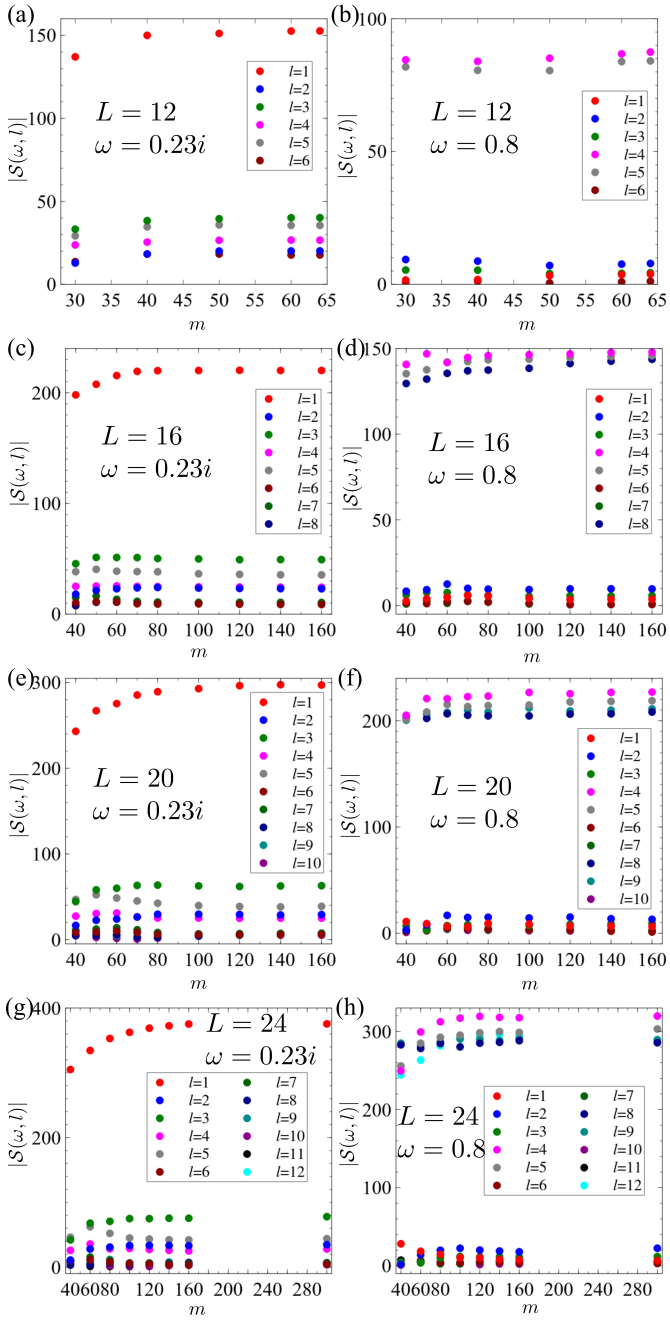

Figure 6.3. The spectral function $\mathcal{S}(\omega, l)$ computed for different L and ω as a function of maximum bond dimension m. The parameters for H (Eq. (4.32)) are $h_z = J$ and $\gamma = 0$.

Hamiltonian $\mathcal{H}$ is not sensitive to boundary conditions: in the thermodynamic limit, the spectrum is the same under both boundary conditions except that when ω lies in the point gap of H, the spectrum under OBC

shows more topological zero modes than that under PBC [253, 269]. It is due to the contribution of these additional zero modes to the Green's function of $\mathcal{H}$ in Eq. (6.14) that allows faithfully computing the spectral function of H using NHKPM, despite the different sensitivities of the spectral functions of H and $\mathcal{H}$ to the boundary condition. We illustrate this with the Hatano-Nelson model [259]:

$$H_{\text{HN}} = \sum_{l=1}^{L-1} (t+\gamma) c_l^\dagger c_{l+1} + (t-\gamma) c_{l+1}^\dagger c_l, \tag{6.49}$$

which exhibits NHSE when $\gamma \neq 0$. We compute the total density of states of the model:

$$\rho_{\text{tot}}(\omega) = \sum_n \delta(\text{Re}(\omega - E_n))\delta(\text{Im}(\omega - E_n)). \tag{6.50}$$

For simplicity, we take $L = 8$, and we note that analogous results can be obtained for larger L. The spectrum of H_{HN} computed with ED with $t = 1$ and $\gamma = 0.4$ under periodic boundary condition (PBC) and open boundary condition (OBC) are shown in Figs.6.4(a) and (d). We see that the PBC spectrum features a point gap, whereas the OBC spectrum is purely real. The spectrum computed with NHKPM in both cases are shown in Figs.6.4(b) and (e), demonstrating the capability of NHKPM to provide faithful results in both cases. The reason that NHKPM provides a faithful OBC spectrum in this case is due to the contribution of the zero modes of $\mathcal{H}$ to $G(E = 0)$ when ω lies in the point gap of H. Due to finite-size effects, these zero modes have an exponentially small finite energy: $\mathcal{E}_0 \propto \exp(-L/L_0)$ where L_0 is a constant. According to Eq. (6.46), to accurately capture the contribution of this zero mode to $G(E = 0)$, we require:

$$\sigma = \frac{\pi}{N} \lesssim \frac{\mathcal{E}_0}{2\Delta}, \tag{6.51}$$

which for the exponentially small $\mathcal{E}_0$ requires an exponentially large N, hence the large N in Figs.6.4(e). When smaller N is used, the computed spectrum becomes a pseudo-spectrum [270] under OBC (Fig.6.4(f)) due to inaccurately accounting for the contribution of the zero mode to $G(E = 0)$, while the spectrum under PBC only gets broadened (Fig.6.4(c)). For comparison we also show the OBC spectrum computed with $\gamma = 0$ (Fig.6.4(g-i)), where only a broadening is observed for smaller N due to the absence of NHSE.

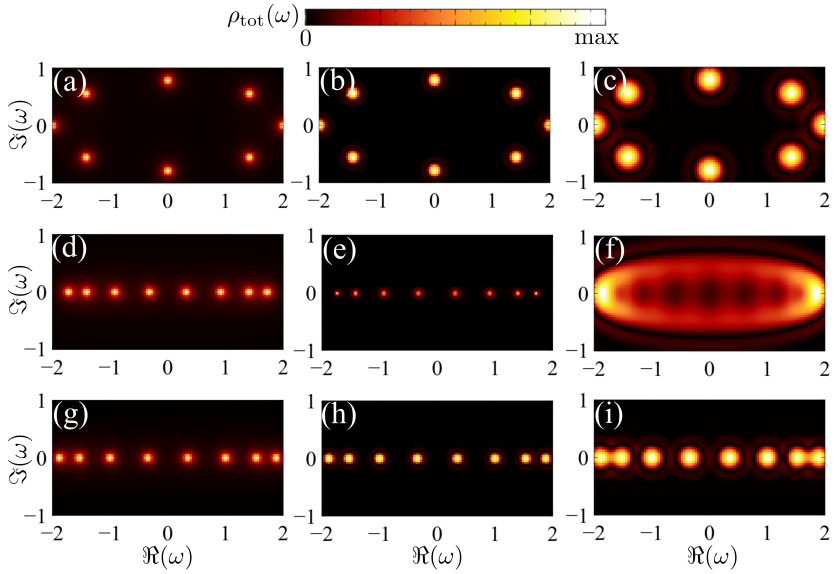

Figure 6.4. Total density of states $\rho_{\mathrm{tot}}(\omega)$ defined in Eq. (6.50) for H_{HN} with $L = 8$ and $t = 1$, with (a) $\gamma = 0.4$, under PBC, computed with ED, (b) $\gamma = 0.4$, under PBC, computed with NHKPM with $N = 100$, (c) $\gamma = 0.4$, under PBC, computed with NHKPM with $N = 50$, (d) $\gamma = 0.4$, under OBC, computed with ED, (e) $\gamma = 0.4$, under OBC, computed with NHKPM with $N = 1000$, (f) $\gamma = 0.4$, under OBC, computed with NHKPM with $N = 50$, (g) $\gamma = 0$, under OBC, computed with ED, (h) $\gamma = 0$, under OBC, computed with NHKPM with $N = 100$, and (i) $\gamma = 0$, under OBC, computed with NHKPM with $N = 50$.

Interacting limit

In the interacting case, the spectrum of H has no point gaps in the thermodynamic limit, and the above analysis no longer holds. Thus, it is unclear whether the algorithm allows for comparable accuracy, which we examine for the model studied in Sec.4.3.

As a benchmark, we compute both $\tilde{\mathcal{S}}_{\mathrm{tot}}(\omega)$ and $\tilde{\rho}(E, l)$ for H with $L = 8$, $h_z = 2J$ and $\gamma = 0.1J$ under OBC (Figs.6.5(a) and (c)), where the results are analogous to Figs.4.2(d) and (g), demonstrating that the NHKPM faithfully computes both spectral functions. We also show $\tilde{\mathcal{S}}_{\mathrm{tot}}(\omega)$ for H under the same set of parameters under PBC, where faithful results are obtained: the two end states with almost 0 real energy under OBC vanish under PBC. We also compute $\tilde{\rho}(E, l)$ for a longer chain with $L = 24$, $h_z = J$ and $\gamma = 0.1J$ (Fig.6.5(d)), where analogous results to Fig.4.3(d) are obtained. This demonstrates the capability of NHKPM to compute spectral functions and identify topological edge modes in the presence of NHSE. We note that in the presence of NHSE, bulk states become also localized at the edge. In this case, it is the definition of the local dynamical spin correlator in Eq. (4.34) that allows to distinguish edge states from bulk

states, and image edge modes in real space. Another remark is that in the presence of NHSE, the condition number [268] of H increases exponentially. Therefore, numerically determining the exact spectrum of a Hamiltonian with NHSE is often very hard and time-consuming. In our algorithm, by using Eq.(6.14), this hard task is converted to the computation of the Green's function of a Hermitian Hamiltonian, which is relatively more controllable.

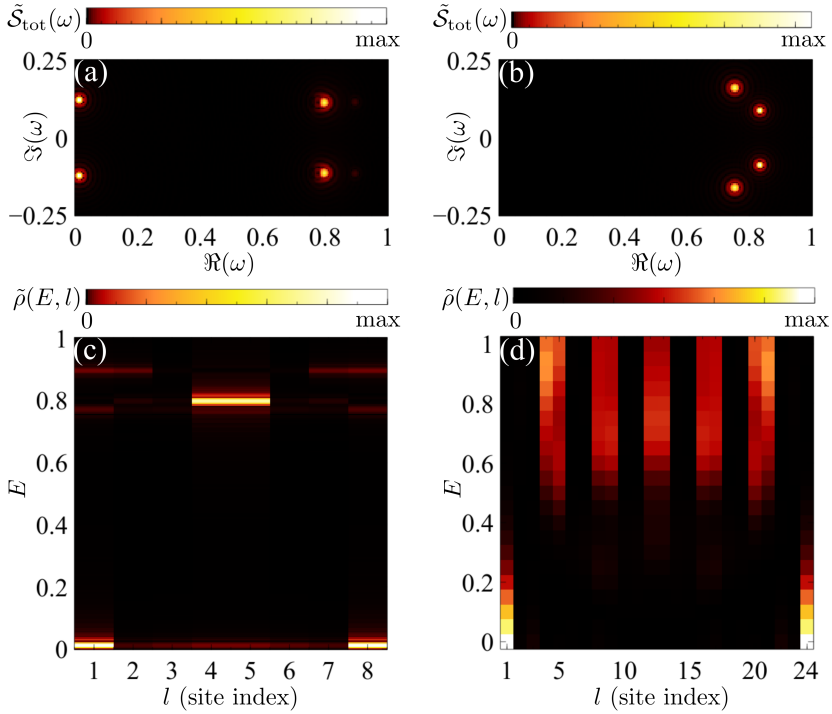

Figure 6.5. (a,b) Total dynamical spin correlator $\tilde{\mathcal{S}}_{\rm tot}(\omega)$ of H defined in Eq. (4.32) with $L = 8$, $h_z = 2J$ and $\gamma = 0.1J$ under (a) open boundary condition and (b) periodic boundary condition. (c) Projected local dynamical structure factor $\tilde{\rho}(E, l)$ corresponding to (a), showing the persistence of topological end modes in the presence of NHSE. (d) $\tilde{\rho}(E, l)$ of H with $L = 24$, $h_z = J$ and $\gamma = 0.1J$, showing the topological end modes in the presence of NHSE for a longer chain.

7. Summary and outlook

Quantum magnetism plays an essential role in a variety of exotic phases including quantum spin liquids, topological superconductivity, and heavy fermions. Despite the great interest in these phases, remarkable challenges remain in their realization and identification in quantum materials. The recently raised magnetic van der Waals materials pave the way to solve this problem. Owing to their two-dimensional nature, they provide a versatile platform to engineer quantum magnetism for the realization and identification of these exotic phases. Throughout the thesis, we have explored the versatility of magnetic van der Waals materials and quantum magnets in three aspects, (i) the engineering of magnetic van der Waals materials for exotic magnetic phases of matter, (ii) the utilization of magnetic van der Waals for designing exotic phases of matter and (iii) the engineering of quantum magnets to get exotic out-of-equilibrium phases.

In particular, exotic magnetic phases of matter such as quantum spin liquids can be realized and probed via external engineering on candidate magnetic van der Waals materials such as 1T-TaS_2. We have shown that, by putting single magnetic atoms on top of 1T-TaS_2, a scanning tunneling microscope measurement would allow to probe the potential U(1) Dirac quantum spin liquid state in this material due to the impurity-induced spinon zero modes. In a similar spirit, a twisted-bilayer 1T-TaS_2 would also allow the probe of the quantum spin liquid state in 1T-TaS_2 due to the magnetically tunable spinon dispersion. In addition, we have shown that depositing 1T-TaS_2 on a substrate and tuning the substrate dielectric constant would allow to drive 1T-TaS_2 toward the quantum spin liquid state.

The versatility of magnetic van der Waals materials is not limited to engineering only magnetic phases of matter. They can also be utilized to design other exotic phases of matter. In particular, we have shown that

helimagnets can be utilized to design helical states in both single-layer graphene and twisted graphene bilayers. In addition, we have presented how heavy fermions can arise in a 1T/1H-TaS_2 heterostructure, which has been realized in experiments.

The versatility of quantum magnets can be even utilized to design exotic phases at non-equilibrium. In particular, we have shown that, by tuning the coupling between a Heisenberg spin chain and the environment, a many-body topological phase emerges solely due to the coupling to the environment. Although we considered a one-dimensional magnet due to computational limitations, our results can be generalized to two-dimensional magnets.

Throughout the above studies, we have implemented a variety of powerful numerical tools. In particular, we have presented two computational libraries developed during the studies. The Twistronics.jl is a user-friendly library allowing non-experts to reproduce the results we presented for twisted multi-layer systems. The NHKPM.jl is a library aiming to overcome numerical challenges in the study of open quantum many-body systems and is based on a newly-developed method we have presented in Sec.6.4.

Our research highlights the versatility of magnetic van der Waals materials for engineering exotic phases of matter. The numerical libraries we have presented help to reduce the difficulty in theoretical studies on these systems. As an outlook, our proposals provide potential guidelines for the experimental research on exotic phases of matter with magnetic van der Waals materials. Our studies can also stimulate further theoretical studies on designing other exotic phases of matter with magnetic van der Waals materials, such as multiferroics.

Bibliography

[1] Nielsen, M. A. *et al.* *Quantum Computation and Quantum Information: 10th Anniversary Edition* (Cambridge University Press, 2010).

[2] Wen, X. G. Vacuum degeneracy of chiral spin states in compactified space. *Phys. Rev. B* **40**, 7387–7390 (1989). URL https://link.aps.org/doi/10.1103/PhysRevB.40.7387.

[3] Tsui, D. C. *et al.* Two-dimensional magnetotransport in the extreme quantum limit. *Phys. Rev. Lett.* **48**, 1559–1562 (1982). URL https://link.aps.org/doi/10.1103/PhysRevLett.48.1559.

[4] Laughlin, R. B. Anomalous quantum hall effect: An incompressible quantum fluid with fractionally charged excitations. *Phys. Rev. Lett.* **50**, 1395–1398 (1983). URL https://link.aps.org/doi/10.1103/PhysRevLett.50.1395.

[5] Kalmeyer, V. *et al.* Equivalence of the resonating-valence-bond and fractional quantum hall states. *Phys. Rev. Lett.* **59**, 2095–2098 (1987). URL https://link.aps.org/doi/10.1103/PhysRevLett.59.2095.

[6] Kivelson, S. A. *et al.* Topology of the resonating valence-bond state: Solitons and high-T_c superconductivity. *Phys. Rev. B* **35**, 8865–8868 (1987). URL https://link.aps.org/doi/10.1103/PhysRevB.35.8865.

[7] Kitaev, A. Fault-tolerant quantum computation by anyons. *Annals of Physics* **303**, 2–30 (2003). URL https://www.sciencedirect.com/science/article/pii/S0003491602000180.

[8] Kitaev, A. Anyons in an exactly solved model and beyond. *Annals of Physics* **321**, 2–111 (2006). URL https://www.sciencedirect.com/science/article/pii/S0003491605002381. January Special Issue.

[9] Novoselov, K. S. Electric field effect in atomically thin carbon films. *Science* **306**, 666–669 (2004). URL https://doi.org/10.1126/science.1102896.

[10] Guinea, F. *et al.* Energy gaps and a zero-field quantum hall effect in graphene by strain engineering. *Nature Physics* **6**, 30–33 (2009). URL https://doi.org/10.1038/nphys1420.

[11] Gonzalez-Herrero, H. *et al.* Atomic-scale control of graphene magnetism by using hydrogen atoms. *Science* **352**, 437–441 (2016). URL https://doi.org/10.1126/science.aad8038.

[12] Cao, Y. *et al.* Correlated insulator behaviour at half-filling in magic-angle graphene superlattices. *Nature* **556**, 80–84 (2018). URL https://doi.org/10.1038/nature26154.

[13] Cao, Y. *et al.* Unconventional superconductivity in magic-angle graphene superlattices. *Nature* **556**, 43–50 (2018). URL https://doi.org/10.1038/nature26160.

[14] Park, J.-G. Opportunities and challenges of 2d magnetic van der waals materials: magnetic graphene? *Journal of Physics: Condensed Matter* **28**, 301001 (2016). URL https://doi.org/10.1088/0953-8984/28/30/301001.

[15] Huang, B. *et al.* Layer-dependent ferromagnetism in a van der waals crystal down to the monolayer limit. *Nature* **546**, 270–273 (2017). URL https://doi.org/10.1038/nature22391.

[16] Gong, C. *et al.* Discovery of intrinsic ferromagnetism in two-dimensional van der waals crystals. *Nature* **546**, 265–269 (2017). URL https://doi.org/10.1038/nature22060.

[17] Gibertini, M. *et al.* Magnetic 2d materials and heterostructures. *Nature Nanotechnology* **14**, 408–419 (2019). URL https://doi.org/10.1038/s41565-019-0438-6.

[18] Law, K. T. *et al.* 1t-TaS2 as a quantum spin liquid. *Proceedings of the National Academy of Sciences* **114**, 6996–7000 (2017). URL https://doi.org/10.1073/pnas.1706769114.

[19] Klanjšek, M. *et al.* A high-temperature quantum spin liquid with polaron spins. *Nature Physics* **13**, 1130–1134 (2017). URL https://doi.org/10.1038/nphys4212.

[20] Chen, Y. *et al.* Strong correlations and orbital texture in single-layer 1t-TaSe2. *Nature Physics* **16**, 218–224 (2020). URL https://doi.org/10.1038/s41567-019-0744-9.

[21] Banerjee, A. *et al.* Proximate kitaev quantum spin liquid behaviour in a honeycomb magnet. *Nature Materials* **15**, 733–740 (2016). URL https://doi.org/10.1038/nmat4604.

[22] Balents, L. Spin liquids in frustrated magnets. *Nature* **464**, 199–208 (2010). URL https://doi.org/10.1038/nature08917.

[23] Lee, P. A. An end to the drought of quantum spin liquids. *Science* **321**, 1306–1307 (2008). URL https://doi.org/10.1126/science.1163196.

[24] Broholm, C. *et al.* Quantum spin liquids. *Science* **367**, eaay0668 (2020). URL https://doi.org/10.1126/science.aay0668.

[25] Zhou, Y. *et al.* Quantum spin liquid states. *Rev. Mod. Phys.* **89**, 025003 (2017). URL https://link.aps.org/doi/10.1103/RevModPhys.89.025003.

[26] Savary, L. *et al.* Quantum spin liquids: a review. *Reports on Progress in Physics* **80**, 016502 (2016). URL https://doi.org/10.1088%2F0034-4885%2F80%2F1%2F016502.

[27] ANDERSON, P. W. The resonating valence bond state in la2cuo4 and superconductivity. *Science* **235**, 1196–1198 (1987). URL https://doi.org/10.1126/science.235.4793.1196.

[28] Kitaev, A. Anyons in an exactly solved model and beyond. *Annals of Physics* **321**, 2–111 (2006). URL https://doi.org/10.1016/j.aop.2005.10.005.

[29] Aasen, D. *et al.* Electrical probes of the non-abelian spin liquid in kitaev materials. *Phys. Rev. X* **10**, 031014 (2020). URL https://link.aps.org/doi/10.1103/PhysRevX.10.031014.

[30] Kelly, Z. A. *et al.* Electron doping a kagome spin liquid. *Phys. Rev. X* **6**, 041007 (2016). URL https://link.aps.org/doi/10.1103/PhysRevX.6.041007.

[31] Han, T.-H. *et al.* Fractionalized excitations in the spin-liquid state of a kagome-lattice antiferromagnet. *Nature* **492**, 406–410 (2012). URL https://doi.org/10.1038/nature11659.

[32] Bordelon, M. M. *et al.* Field-tunable quantum disordered ground state in the triangular-lattice antiferromagnet NaYbO2. *Nature Physics* **15**, 1058–1064 (2019). URL https://doi.org/10.1038/s41567-019-0594-5.

[33] Murayama, H. *et al.* Effect of quenched disorder on the quantum spin liquid state of the triangular-lattice antiferromagnet $1t-\mathrm{tas}_2$. *Phys. Rev. Research* **2**, 013099 (2020). URL https://link.aps.org/doi/10.1103/PhysRevResearch.2.013099.

[34] Mañas-Valero, S. *et al.* Multiple Quantum Spin Liquid Phases in 1T-TaS2. *arXiv e-prints* arXiv:2007.15905 (2020). 2007.15905.

[35] Takagi, H. *et al.* Concept and realization of kitaev quantum spin liquids. *Nature Reviews Physics* **1**, 264–280 (2019). URL https://doi.org/10.1038/s42254-019-0038-2.

[36] Yang, B. *et al.* Magnetic anisotropy reversal driven by structural symmetry-breaking in monolayer α-RuCl3. *Nature Materials* **22**, 50–57 (2022). URL https://doi.org/10.1038%2Fs41563-022-01401-3.

[37] Cho, D. *et al.* Nanoscale manipulation of the mott insulating state coupled to charge order in 1t-TaS2. *Nature Communications* **7** (2016). URL https://doi.org/10.1038/ncomms10453.

[38] Qiao, S. *et al.* Mottness collapse in $1\mathrm{T}-\mathrm{tas}_{2-x}\mathrm{se}_x$ transition-metal dichalcogenide: An interplay between localized and itinerant orbitals. *Phys. Rev. X* **7**, 041054 (2017). URL https://link.aps.org/doi/10.1103/PhysRevX.7.041054.

[39] Kratochvilova, M. *et al.* The low-temperature highly correlated quantum phase in the charge-density-wave 1T-TaS_2 compound. *npj Quantum Mater.* **2**, 42 (2017). URL https://doi.org/10.1038/s41535-017-0048-1.

[40] Vaňo, V. *et al.* Artificial heavy fermions in a van der waals heterostructure. *Nature* **599**, 582–586 (2021). URL http://dx.doi.org/10.1038/s41586-021-04021-0.

[41] Wang, Y. D. *et al.* Band insulator to mott insulator transition in 1t-TaS2. *Nature Communications* **11** (2020). URL https://doi.org/10.1038/s41467-020-18040-4.

[42] Rossnagel, K. *et al.* Spin-orbit coupling in the band structure of reconstructed $1t-\mathrm{tas}_2$. *Phys. Rev. B* **73**, 073106 (2006). URL https://link.aps.org/doi/10.1103/PhysRevB.73.073106.

[43] Pasquier, D. *et al.* Ab initio theory of magnetism in two-dimensional $1t-\mathrm{tas}_2$. *Phys. Rev. B* **105**, L081106 (2022). URL https://link.aps.org/doi/10.1103/PhysRevB.105.L081106.

[44] Iqbal, Y. *et al.* Spin liquid nature in the heisenberg $J_1 - J_2$ triangular antiferromagnet. *Phys. Rev. B* **93**, 144411 (2016). URL https://link.aps.org/doi/10.1103/PhysRevB.93.144411.

[45] Hu, S. *et al.* Dirac spin liquid on the spin-$1/2$ triangular heisenberg antiferromagnet. *Phys. Rev. Lett.* **123**, 207203 (2019). URL https://link.aps.org/doi/10.1103/PhysRevLett.123.207203.

[46] Alloul, H. *et al.* Defects in correlated metals and superconductors. *Rev. Mod. Phys.* **81**, 45–108 (2009). URL https://link.aps.org/doi/10.1103/RevModPhys.81.45.

[47] Balian, R. *et al.* Superconductivity with pairs in a relative p wave. *Phys. Rev.* **131**, 1553–1564 (1963). URL https://link.aps.org/doi/10.1103/PhysRev.131.1553.

[48] Agterberg, D. F. Impurities and orbital-dependent superconductivity in $\mathrm{sr}_2\mathrm{ruo}_4$. *Phys. Rev. B* **60**, R749–R752 (1999). URL https://link.aps.org/doi/10.1103/PhysRevB.60.R749.

[49] Maki, K. *et al.* Impurity bound states and symmetry of the superconducting order parameter in $\mathrm{sr}_2\mathrm{ruo}_4$. *Phys. Rev. B* **62**, R11969–R11972 (2000). URL https://link.aps.org/doi/10.1103/PhysRevB.62.R11969.

[50] Zinkl, B. *et al.* Superconducting gap anisotropy and topological singularities due to lattice translational symmetry and their thermodynamic signatures. *Phys. Rev. B* **100**, 014519 (2019). URL https://link.aps.org/doi/10.1103/PhysRevB.100.014519.

[51] Anderson, P. Theory of dirty superconductors. *Journal of Physics and Chemistry of Solids* **11**, 26–30 (1959). URL https://doi.org/10.1016/0022-3697(59)90036-8.

[52] Balatsky, A. V. *et al.* Impurity-induced states in conventional and unconventional superconductors. *Rev. Mod. Phys.* **78**, 373–433 (2006). URL https://link.aps.org/doi/10.1103/RevModPhys.78.373.

[53] Shiba, H. Classical spins in superconductors. *Progress of Theoretical Physics* **40**, 435–451 (1968). URL https://doi.org/10.1143/ptp.40.435.

[54] Rusinov, A. I. Superconductivity near a Paramagnetic Impurity. *Soviet Journal of Experimental and Theoretical Physics Letters* **9**, 85 (1969).

[55] Sprunger, P. T. *et al.* Giant friedel oscillations on the beryllium(0001) surface. *Science* **275**, 1764–1767 (1997). URL https://doi.org/10.1126/science.275.5307.1764.

[56] Petersen, L. *et al.* Direct imaging of the two-dimensional fermi contour: Fourier-transform stm. *Phys. Rev. B* **57**, R6858–R6861 (1998). URL https://link.aps.org/doi/10.1103/PhysRevB.57.R6858.

[57] Weismann, A. *et al.* Seeing the fermi surface in real space by nanoscale electron focusing. *Science* **323**, 1190–1193 (2009). URL https://doi.org/10.1126/science.1168738.

[58] Duplock, E. J. *et al.* Hallmark of perfect graphene. *Phys. Rev. Lett.* **92**, 225502 (2004). URL https://link.aps.org/doi/10.1103/PhysRevLett.92.225502.

[59] Yazyev, O. V. Emergence of magnetism in graphene materials and nanostructures. *Reports on Progress in Physics* **73**, 056501 (2010). URL https://doi.org/10.1088/0034-4885/73/5/056501.

[60] Yazyev, O. V. *et al.* Defect-induced magnetism in graphene. *Phys. Rev. B* **75**, 125408 (2007). URL https://link.aps.org/doi/10.1103/PhysRevB.75.125408.

[61] Palacios, J. J. *et al.* Vacancy-induced magnetism in graphene and graphene ribbons. *Phys. Rev. B* **77**, 195428 (2008). URL https://link.aps.org/doi/10.1103/PhysRevB.77.195428.

[62] Lehtinen, P. O. *et al.* Irradiation-induced magnetism in graphite: A density functional study. *Phys. Rev. Lett.* **93**, 187202 (2004). URL https://link.aps.org/doi/10.1103/PhysRevLett.93.187202.

[63] Pereira, V. M. *et al.* Disorder induced localized states in graphene. *Phys. Rev. Lett.* **96**, 036801 (2006). URL https://link.aps.org/doi/10.1103/PhysRevLett.96.036801.

[64] Lopez-Bezanilla, A. *et al.* Defect-induced magnetism and yu-shiba-rusinov states in twisted bilayer graphene. *Phys. Rev. Materials* **3**, 084003 (2019). URL https://link.aps.org/doi/10.1103/PhysRevMaterials.3.084003.

[65] Boukhvalov, D. W. *et al.* Hydrogen on graphene: Electronic structure, total energy, structural distortions and magnetism from first-principles calculations. *Phys. Rev. B* **77**, 035427 (2008). URL https://link.aps.org/doi/10.1103/PhysRevB.77.035427.

[66] García-Martínez, N. A. *et al.* Anomalous magnetism in hydrogenated graphene. *Phys. Rev. B* **96**, 024403 (2017). URL https://link.aps.org/doi/10.1103/PhysRevB.96.024403.

[67] Choi, D.-J. *et al.* Colloquium: Atomic spin chains on surfaces. *Rev. Mod. Phys.* **91**, 041001 (2019). URL https://link.aps.org/doi/10.1103/RevModPhys.91.041001.

[68] Hirjibehedin, C. F. *et al.* Large magnetic anisotropy of a single atomic spin embedded in a surface molecular network. *Science* **317**, 1199–1203 (2007). URL https://doi.org/10.1126/science.1146110.

[69] Otte, A. F. *et al.* The role of magnetic anisotropy in the kondo effect. *Nature Physics* **4**, 847–850 (2008). URL https://doi.org/10.1038/nphys1072.

[70] Loth, S. *et al.* Controlling the state of quantum spins with electric currents. *Nature Physics* **6**, 340–344 (2010). URL https://doi.org/10.1038/nphys1616.

[71] Loth, S. *et al.* Measurement of fast electron spin relaxation times with atomic resolution. *Science* **329**, 1628–1630 (2010). URL https://doi.org/10.1126/science.1191688.

[72] Otte, A. F. *et al.* Spin excitations of a kondo-screened atom coupled to a second magnetic atom. *Phys. Rev. Lett.* **103**, 107203 (2009). URL https://link.aps.org/doi/10.1103/PhysRevLett.103.107203.

[73] Loth, S. *et al.* Bistability in atomic-scale antiferromagnets. *Science* **335**, 196–199 (2012). URL https://doi.org/10.1126/science.1214131.

[74] Hirjibehedin, C. F. *et al.* Spin coupling in engineered atomic structures. *Science* **312**, 1021–1024 (2006). URL https://doi.org/10.1126/science.1125398.

[75] Liebhaber, E. *et al.* Yu–shiba–rusinov states in the charge-density modulated superconductor NbSe2. *Nano Letters* **20**, 339–344 (2019). URL https://doi.org/10.1021/acs.nanolett.9b03988.

[76] Farinacci, L. *et al.* Tuning the coupling of an individual magnetic impurity to a superconductor: Quantum phase transition and transport. *Phys. Rev. Lett.* **121**, 196803 (2018). URL https://link.aps.org/doi/10.1103/PhysRevLett.121.196803.

[77] Kezilebieke, S. *et al.* Observation of coexistence of yu-shiba-rusinov states and spin-flip excitations. *Nano Letters* **19**, 4614–4619 (2019). URL https://doi.org/10.1021/acs.nanolett.9b01583.

[78] Gross, L. *et al.* Measuring the charge state of an adatom with noncontact atomic force microscopy. *Science* **324**, 1428–1431 (2009). URL https://doi.org/10.1126/science.1172273.

[79] Drost, R. *et al.* Topological states in engineered atomic lattices. *Nature Physics* **13**, 668–671 (2017). URL https://doi.org/10.1038/nphys4080.

[80] Heinrich, A. J. *et al.* Single-atom spin-flip spectroscopy. *Science* **306**, 466–469 (2004). URL https://doi.org/10.1126/science.1101077.

[81] Ternes, M. *et al.* The force needed to move an atom on a surface. *Science* **319**, 1066–1069 (2008). URL https://doi.org/10.1126/science.1150288.

[82] Yang, K. *et al.* Engineering the eigenstates of coupled spin-$1/2$ atoms on a surface. *Phys. Rev. Lett.* **119**, 227206 (2017). URL https://link.aps.org/doi/10.1103/PhysRevLett.119.227206.

[83] Kalff, F. E. *et al.* A kilobyte rewritable atomic memory. *Nature Nanotechnology* **11**, 926–929 (2016). URL https://doi.org/10.1038/nnano.2016.131.

[84] Chen, G. *et al.* Impurity-induced resonant spinon zero modes in dirac quantum spin liquids. *Phys. Rev. Res.* **2**, 033466 (2020). URL https://link.aps.org/doi/10.1103/PhysRevResearch.2.033466.

[85] Spinelli, A. *et al.* Imaging of spin waves in atomically designed nanomagnets. *Nature Materials* **13**, 782–785 (2014). URL https://doi.org/10.1038/nmat4018.

[86] Fernández-Rossier, J. Theory of single-spin inelastic tunneling spectroscopy. *Phys. Rev. Lett.* **102**, 256802 (2009). URL https://link.aps.org/doi/10.1103/PhysRevLett.102.256802.

[87] Spinelli, A. *et al.* Imaging of spin waves in atomically designed nanomagnets. *Nature Materials* **13**, 782–785 (2014). URL https://doi.org/10.1038/nmat4018.

[88] Suárez Morell, E. *et al.* Flat bands in slightly twisted bilayer graphene: Tight-binding calculations. *Phys. Rev. B* **82**, 121407 (2010). URL https://link.aps.org/doi/10.1103/PhysRevB.82.121407.

[89] Bistritzer, R. *et al.* Moire bands in twisted double-layer graphene. *Proceedings of the National Academy of Sciences* **108**, 12233–12237 (2011). URL https://doi.org/10.1073/pnas.1108174108.

[90] Lu, X. *et al.* Superconductors, orbital magnets and correlated states in magic-angle bilayer graphene. *Nature* **574**, 653–657 (2019). URL https://doi.org/10.1038/s41586-019-1695-0.

[91] Yankowitz, M. *et al.* Tuning superconductivity in twisted bilayer graphene. *Science* **363**, 1059–1064 (2019). URL https://doi.org/10.1126/science.aav1910.

[92] Cao, Y. *et al.* Strange metal in magic-angle graphene with near planckian dissipation. *Phys. Rev. Lett.* **124**, 076801 (2020). URL https://link.aps.org/doi/10.1103/PhysRevLett.124.076801.

[93] Cao, Y. *et al.* Tunable correlated states and spin-polarized phases in twisted bilayer–bilayer graphene. *Nature* **583**, 215–220 (2020). URL https://doi.org/10.1038/s41586-020-2260-6.

[94] Wolf, T. M. R. *et al.* Spontaneous valley spirals in magnetically encapsulated twisted bilayer graphene. *Phys. Rev. Lett.* **126**, 056803 (2021). URL https://link.aps.org/doi/10.1103/PhysRevLett.126.056803.

[95] Wolf, T. M. R. *et al.* Electrically tunable flat bands and magnetism in twisted bilayer graphene. *Phys. Rev. Lett.* **123**, 096802 (2019). URL https://link.aps.org/doi/10.1103/PhysRevLett.123.096802.

[96] Koshino, M. Band structure and topological properties of twisted double bilayer graphene. *Phys. Rev. B* **99**, 235406 (2019). URL https://link.aps.org/doi/10.1103/PhysRevB.99.235406.

[97] Liu, Z. *et al.* Gate-tunable fractional chern insulators in twisted double bilayer graphene. *Phys. Rev. Lett.* **126**, 026801 (2021). URL https://link.aps.org/doi/10.1103/PhysRevLett.126.026801.

[98] Abouelkomsan, A. *et al.* Particle-hole duality, emergent fermi liquids, and fractional chern insulators in moiré flatbands. *Phys. Rev. Lett.* **124**, 106803 (2020). URL https://link.aps.org/doi/10.1103/PhysRevLett.124.106803.

[99] Serlin, M. *et al.* Intrinsic quantized anomalous hall effect in a moiré heterostructure. *Science* **367**, 900–903 (2019). URL https://doi.org/10.1126/science.aay5533.

[100] Zhang, Y.-H. *et al.* Quantum hall spin liquids and their possible realization in moiré systems. *Phys. Rev. B* **102**, 115127 (2020). URL https://link.aps.org/doi/10.1103/PhysRevB.102.115127.

[101] Can, O. *et al.* High-temperature topological superconductivity in twisted double-layer copper oxides. *Nature Physics* (2021). URL https://doi.org/10.1038/s41567-020-01142-7.

[102] Hejazi, K. *et al.* Noncollinear phases in moiré magnets. *Proceedings of the National Academy of Sciences* **117**, 10721–10726 (2020). URL https://doi.org/10.1073/pnas.2000347117.

[103] May-Mann, J. *et al.* Twisted kitaev bilayers and the moiré ising model. *Phys. Rev. B* **101**, 245126 (2020). URL https://link.aps.org/doi/10.1103/PhysRevB.101.245126.

[104] Zhu, X. *et al.* Magnon bands in twisted bilayer honeycomb quantum magnets. *arXiv e-prints* arXiv:2008.11640 (2020). 2008.11640.

[105] Sboychakov, A. O. *et al.* Electronic spectrum of twisted bilayer graphene. *Phys. Rev. B* **92**, 075402 (2015). URL https://link.aps.org/doi/10.1103/PhysRevB.92.075402.

[106] Gonzalez-Arraga, L. A. *et al.* Electrically controllable magnetism in twisted bilayer graphene. *Phys. Rev. Lett.* **119**, 107201 (2017). URL https://link.aps.org/doi/10.1103/PhysRevLett.119.107201.

[107] Su, Y. *et al.* Pairing symmetry and spontaneous vortex-antivortex lattice in superconducting twisted-bilayer graphene: Bogoliubov-de gennes approach. *Phys. Rev. B* **98**, 195101 (2018). URL https://link.aps.org/doi/10.1103/PhysRevB.98.195101.

[108] Julku, A. *et al.* Superfluid weight and berezinskii-kosterlitz-thouless transition temperature of twisted bilayer graphene. *Phys. Rev. B* **101**, 060505 (2020). URL https://link.aps.org/doi/10.1103/PhysRevB.101.060505.

[109] Castro Neto, A. H. *et al.* The electronic properties of graphene. *Rev. Mod. Phys.* **81**, 109–162 (2009). URL https://link.aps.org/doi/10.1103/RevModPhys.81.109.

[110] San-Jose, P. *et al.* Non-abelian gauge potentials in graphene bilayers. *Phys. Rev. Lett.* **108**, 216802 (2012). URL https://link.aps.org/doi/10.1103/PhysRevLett.108.216802.

[111] Colomés, E. *et al.* Antichiral edge states in a modified haldane nanoribbon. *Phys. Rev. Lett.* **120**, 086603 (2018). URL https://link.aps.org/doi/10.1103/PhysRevLett.120.086603.

[112] Soriano, D. *et al.* Exchange-bias controlled correlations in magnetically encapsulated twisted van der waals dichalcogenides. *Journal of Physics D: Applied Physics* **53**, 474001 (2020). URL https://doi.org/10.1088/1361-6463/abaa15.

[113] Ramires, A. *et al.* Impurity-induced triple point fermions in twisted bilayer graphene. *Phys. Rev. B* **99**, 245118 (2019). URL https://link.aps.org/doi/10.1103/PhysRevB.99.245118.

[114] Lopez-Bezanilla, A. *et al.* Electrical band flattening, valley flux, and superconductivity in twisted trilayer graphene. *Phys. Rev. Research* **2**, 033357 (2020). URL https://link.aps.org/doi/10.1103/PhysRevResearch.2.033357.

[115] Liu, M.-H. *et al.* Scalable tight-binding model for graphene. *Phys. Rev. Lett.* **114**, 036601 (2015). URL https://link.aps.org/doi/10.1103/PhysRevLett.114.036601.

[116] Ran, Y. *et al.* Projected-wave-function study of the spin-$1/2$ heisenberg model on the kagomé lattice. *Phys. Rev. Lett.* **98**, 117205 (2007). URL https://link.aps.org/doi/10.1103/PhysRevLett.98.117205.

[117] Ahn, J. *et al.* Failure of nielsen-ninomiya theorem and fragile topology in two-dimensional systems with space-time inversion symmetry: Application to twisted bilayer graphene at magic angle. *Phys. Rev. X* **9**, 021013 (2019). URL https://link.aps.org/doi/10.1103/PhysRevX.9.021013.

[118] Po, H. C. *et al.* Origin of mott insulating behavior and superconductivity in twisted bilayer graphene. *Phys. Rev. X* **8**, 031089 (2018). URL https://link.aps.org/doi/10.1103/PhysRevX.8.031089.

[119] Wu, Q. *et al.* Landau levels as a probe for band topology in graphene moiré superlattices. *Phys. Rev. Lett.* **126**, 056401 (2021). URL https://link.aps.org/doi/10.1103/PhysRevLett.126.056401.

[120] Liu, J. *et al.* Quantum valley hall effect, orbital magnetism, and anomalous hall effect in twisted multilayer graphene systems. *Phys. Rev. X* **9**, 031021 (2019). URL https://link.aps.org/doi/10.1103/PhysRevX.9.031021.

[121] Chebrolu, N. R. *et al.* Flat bands in twisted double bilayer graphene. *Phys. Rev. B* **99**, 235417 (2019). URL https://link.aps.org/doi/10.1103/PhysRevB.99.235417.

[122] Prada, E. *et al.* Band topology and the quantum spin hall effect in bilayer graphene. *Solid State Communications* **151**, 1075–1083 (2011). URL https://doi.org/10.1016/j.ssc.2011.05.016.

[123] Zhang, F. *et al.* Valley chern numbers and boundary modes in gapped bilayer graphene. *Proceedings of the National Academy of Sciences* **110**, 10546–10551 (2013). URL https://doi.org/10.1073/pnas.1308853110.

[124] Wright, A. R. *et al.* Robust one-dimensional wires in lattice mismatched bilayer graphene. *Applied Physics Letters* **98**, 251902 (2011). URL https://doi.org/10.1063/1.3601851.

[125] San-Jose, P. *et al.* Helical networks in twisted bilayer graphene under interlayer bias. *Phys. Rev. B* **88**, 121408 (2013). URL https://link.aps.org/doi/10.1103/PhysRevB.88.121408.

[126] Rickhaus, P. *et al.* Transport through a network of topological channels in twisted bilayer graphene. *Nano Letters* **18**, 6725–6730 (2018). URL https://doi.org/10.1021/acs.nanolett.8b02387.

[127] Morpurgo, A. F. *et al.* Intervalley scattering, long-range disorder, and effective time-reversal symmetry breaking in graphene. *Phys. Rev. Lett.* **97**, 196804 (2006). URL https://link.aps.org/doi/10.1103/PhysRevLett.97.196804.

[128] Chen, J.-H. *et al.* Defect scattering in graphene. *Phys. Rev. Lett.* **102**, 236805 (2009). URL https://link.aps.org/doi/10.1103/PhysRevLett.102.236805.

[129] Chen, G. *et al.* Tunable moire spinons in magnetically encapsulated twisted van der waals quantum spin liquids. *Phys. Rev. Res.* **3**, 033276 (2021). URL https://link.aps.org/doi/10.1103/PhysRevResearch.3.033276.

[130] Ghazaryan, D. *et al.* Magnon-assisted tunnelling in van der waals heterostructures based on CrBr3. *Nature Electronics* **1**, 344–349 (2018). URL https://doi.org/10.1038/s41928-018-0087-z.

[131] Kezilebieke, S. *et al.* Electronic and magnetic characterization of epitaxial crbr$_3$ monolayers (2020). 2009.13465.

[132] Anderson, P. W. Antiferromagnetism. theory of superexchange interaction. *Phys. Rev.* **79**, 350–356 (1950). URL https://link.aps.org/doi/10.1103/PhysRev.79.350.

[133] Cardoso, C. *et al.* Van der waals spin valves. *Phys. Rev. Lett.* **121**, 067701 (2018). URL https://link.aps.org/doi/10.1103/PhysRevLett.121.067701.

[134] Singh, S. *et al.* Strong modulation of spin currents in bilayer graphene by static and fluctuating proximity exchange fields. *Phys. Rev. Lett.* **118**, 187201 (2017). URL https://link.aps.org/doi/10.1103/PhysRevLett.118.187201.

[135] Wei, P. *et al.* Strong interfacial exchange field in the graphene/EuS heterostructure. *Nature Materials* **15**, 711–716 (2016). URL https://doi.org/10.1038/nmat4603.

[136] Wang, Z. *et al.* Proximity-induced ferromagnetism in graphene revealed by the anomalous hall effect. *Phys. Rev. Lett.* **114**, 016603 (2015). URL https://link.aps.org/doi/10.1103/PhysRevLett.114.016603.

[137] Sivadas, N. *et al.* Stacking-dependent magnetism in bilayer CrI3. *Nano Letters* **18**, 7658–7664 (2018). URL https://doi.org/10.1021/acs.nanolett.8b03321.

[138] Soriano, D. *et al.* Interplay between interlayer exchange and stacking in CrI3 bilayers. *Solid State Communications* **299**, 113662 (2019). URL https://doi.org/10.1016/j.ssc.2019.113662.

[139] Song, T. *et al.* Switching 2d magnetic states via pressure tuning of layer stacking. *Nature Materials* **18**, 1298–1302 (2019). URL https://doi.org/10.1038/s41563-019-0505-2.

[140] Li, T. *et al.* Pressure-controlled interlayer magnetism in atomically thin CrI3. *Nature Materials* **18**, 1303–1308 (2019). URL https://doi.org/10.1038/s41563-019-0506-1.

[141] Lopes dos Santos, J. M. B. *et al.* Graphene bilayer with a twist: Electronic structure. *Phys. Rev. Lett.* **99**, 256802 (2007). URL https://link.aps.org/doi/10.1103/PhysRevLett.99.256802.

[142] Richter, N. *et al.* Temperature-dependent magnetic anisotropy in the layered magnetic semiconductors $\mathrm{Cri_3}$ and $\mathrm{CrBr_3}$. *Phys. Rev. Materials* **2**, 024004 (2018). URL https://link.aps.org/doi/10.1103/PhysRevMaterials.2.024004.

[143] Klein, D. R. *et al.* Probing magnetism in 2d van der waals crystalline insulators via electron tunneling. *Science* **360**, 1218–1222 (2018). URL https://doi.org/10.1126/science.aar3617.

[144] Jena, D. *et al.* Enhancement of carrier mobility in semiconductor nanostructures by dielectric engineering. *Phys. Rev. Lett.* **98**, 136805 (2007). URL https://link.aps.org/doi/10.1103/PhysRevLett.98.136805.

[145] Rösner, M. *et al.* Wannier function approach to realistic coulomb interactions in layered materials and heterostructures. *Phys. Rev. B* **92**, 085102 (2015). URL https://link.aps.org/doi/10.1103/PhysRevB.92.085102.

[146] Raja, A. *et al.* Coulomb engineering of the bandgap and excitons in two-dimensional materials. *Nature Communications* **8** (2017). URL https://doi.org/10.1038/ncomms15251.

[147] Rösner, M. *et al.* Two-dimensional heterojunctions from nonlocal manipulations of the interactions. *Nano Letters* **16**, 2322–2327 (2016). URL https://doi.org/10.1021/acs.nanolett.5b05009.

[148] Steinhoff, A. *et al.* Exciton fission in monolayer transition metal dichalcogenide semiconductors. *Nature Communications* **8**, 1166 (2017). URL https://www.nature.com/articles/s41467-017-01298-6.

[149] Utama, M. I. B. *et al.* A dielectric-defined lateral heterojunction in a monolayer semiconductor. *Nature Electronics* **2**, 60–65 (2019). URL https://doi.org/10.1038/s41928-019-0207-4.

[150] Steinke, C. *et al.* Coulomb-engineered heterojunctions and dynamical screening in transition metal dichalcogenide monolayers. *Phys. Rev. B* **102**, 115111 (2020). URL https://link.aps.org/doi/10.1103/PhysRevB.102.115111.

[151] Waldecker, L. *et al.* Rigid band shifts in two-dimensional semiconductors through external dielectric screening. *Phys. Rev. Lett.* **123**, 206403 (2019). URL https://link.aps.org/doi/10.1103/PhysRevLett.123.206403.

[152] van Loon, E. G. C. P. *et al.* Coulomb engineering of two-dimensional mott materials (2020). 2001.01735.

[153] Steinke, C. *et al.* Noninvasive control of excitons in two-dimensional materials. *Phys. Rev. B* **96**, 045431 (2017). URL https://link.aps.org/doi/10.1103/PhysRevB.96.045431.

[154] da Jornada, F. H. *et al.* Universal slow plasmons and giant field enhancement in atomically thin quasi-two-dimensional metals. *Nature Communications* **11**, 1013 (2020). URL https://www.nature.com/articles/s41467-020-14826-8.

[155] Jiang, Z. *et al.* Plasmonic waveguides from coulomb-engineered two-dimensional metals. *2D Materials* **8**, 035037 (2021). URL https://doi.org/10.1088/2053-1583/abfedd.

[156] Rösner, M. *et al.* Inducing a many-body topological state of matter through coulomb-engineered local interactions. *Phys. Rev. Research* **3**, 013265 (2021). URL https://link.aps.org/doi/10.1103/PhysRevResearch.3.013265.

[157] Ohno, K. Some remarks on the pariser-parr-pople method. *Theoretica chimica acta* **2**, 219–227 (1964). URL https://doi.org/10.1007/bf00528281.

[158] Keldysh, L. V. Coulomb interaction in thin semiconductor and semimetal films. *Soviet Journal of Experimental and Theoretical Physics Letters* **29**, 658 (1979).

[159] in 't Veld, Y. *et al.* Bandwidth renormalization due to the intersite coulomb interaction. *Journal of Physics: Condensed Matter* **31**, 465603 (2019). URL https://doi.org/10.1088/1361-648x/ab36fe.

[160] Ayral, T. *et al.* Influence of fock exchange in combined many-body perturbation and dynamical mean field theory. *Phys. Rev. B* **95**, 245130 (2017). URL https://link.aps.org/doi/10.1103/PhysRevB.95.245130.

[161] Kamil, E. *et al.* Electronic structure of single layer 1t-NbSe2: interplay of lattice distortions, non-local exchange, and mott–hubbard correlations. *Journal of Physics: Condensed Matter* **30**, 325601 (2018). URL https://doi.org/10.1088/1361-648x/aad215.

[162] Pizarro, J. M. *et al.* Deconfinement of mott localized electrons into topological and spin–orbit-coupled dirac fermions. *npj Quantum Materials* **5** (2020). URL https://doi.org/10.1038/s41535-020-00277-3.

[163] Giampaolo, S. M. *et al.* Characterizing and quantifying frustration in quantum many-body systems. *Phys. Rev. Lett.* **107**, 260602 (2011). URL https://link.aps.org/doi/10.1103/PhysRevLett.107.260602.

[164] Egger, R. *et al.* Emerging dirac and majorana fermions for carbon nanotubes with proximity-induced pairing and spiral magnetic field. *Physical Review B* **85** (2012). URL https://doi.org/10.1103/physrevb.85.235462.

[165] Chen, G. *et al.* Designing spin-textured flat bands in twisted graphene multilayers via helimagnet encapsulation. *2D Materials* **9**, 024002 (2022). URL https://dx.doi.org/10.1088/2053-1583/ac4af8.

[166] Chen, G. *et al.* Controlling magnetic frustration in 1t-tas2 via coulomb engineered long-range interactions. *Journal of Physics: Condensed Matter* **34**, 485805 (2022). URL https://dx.doi.org/10.1088/1361-648X/ac9812.

[167] Mazurenko, V. V. *et al.* Role of direct exchange and dzyaloshinskii-moriya interactions in magnetic properties of graphene derivatives: c_2F and c_2H. *Phys. Rev. B* **94**, 214411 (2016). URL https://link.aps.org/doi/10.1103/PhysRevB.94.214411.

[168] Soriano, D. *et al.* Environmental screening and ligand-field effects to magnetism in CrI3 monolayer. *npj Computational Materials* **7** (2021). URL https://doi.org/10.1038/s41524-021-00631-4.

[169] Lado, J. L. *et al.* Designer quantum matter in van der waals heterostructures (2021). URL https://arxiv.org/abs/2102.11779.

[170] Alicea, J. *et al.* Non-abelian statistics and topological quantum information processing in 1d wire networks. *Nature Physics* **7**, 412–417 (2011). URL https://doi.org/10.1038/nphys1915.

[171] Aasen, D. *et al.* Milestones toward majorana-based quantum computing. *Phys. Rev. X* **6**, 031016 (2016). URL https://link.aps.org/doi/10.1103/PhysRevX.6.031016.

[172] Stewart, G. R. Superconductivity in iron compounds. *Rev. Mod. Phys.* **83**, 1589–1652 (2011). URL https://link.aps.org/doi/10.1103/RevModPhys.83.1589.

[173] Allan, M. P. *et al.* Imaging Cooper pairing of heavy fermions in $CeCoIn_5$. *Nat. Phys.* **9**, 468–473 (2013). URL https://doi.org/10.1038/nphys2671.

[174] Zhou, B. B. *et al.* Visualizing nodal heavy fermion superconductivity in $CeCoIn_5$. *Nat. Phys.* **9**, 474–479 (2013). URL https://doi.org/10.1038/nphys2672.

[175] Stewart, G. R. Unconventional superconductivity. *Adv. Phys.* **66**, 75–196 (2017). URL https://doi.org/10.1080/00018732.2017.1331615.

[176] Jiao, L. *et al.* Chiral superconductivity in heavy-fermion metal UTe_2. *Nature* **579**, 523–527 (2020). URL https://doi.org/10.1038/s41586-020-2122-2.

[177] Joynt, R. *et al.* The superconducting phases of UPt_3. *Rev. Mod. Phys.* **74**, 235–294 (2002). URL https://link.aps.org/doi/10.1103/RevModPhys.74.235.

[178] Schemm, E. R. *et al.* Observation of broken time-reversal symmetry in the heavy-fermion superconductor UPt_3. *Science* **345**, 190–193 (2014). URL https://doi.org/10.1126/science.1248552.

[179] Avers, K. E. *et al.* Broken time-reversal symmetry in the topological superconductor UPt_3. *Nat. Phys.* **16**, 531–535 (2020). URL https://doi.org/10.1038/s41567-020-0822-z.

[180] Nadj-Perge, S. *et al.* Observation of Majorana fermions in ferromagnetic atomic chains on a superconductor. *Science* **346**, 602–607 (2014). URL https://doi.org/10.1126/science.1259327.

[181] Kezilebieke, S. *et al.* Topological superconductivity in a van der Waals heterostructure. *Nature* **588**, 424–428 (2020). URL http://dx.doi.org/10.1038/s41586-020-2989-y.

[182] Nayak, A. K. *et al.* Evidence of topological boundary modes with topological nodal-point superconductivity. *Nature Physics* **17**, 1413–1419 (2021). URL https://doi.org/10.1038/s41567-021-01376-z.

[183] Kezilebieke, S. *et al.* Moiré-enabled topological superconductivity. *Nano Letters* **22**, 328–333 (2022). URL https://doi.org/10.1021/acs.nanolett.1c03856. PMID: 34978831, https://doi.org/10.1021/acs.nanolett.1c03856.

[184] Kitaev, A. Y. Unpaired majorana fermions in quantum wires. *Physics-Uspekhi* **44**, 131 (2001). URL https://dx.doi.org/10.1070/1063-7869/44/10S/S29.

[185] Alicea, J. New directions in the pursuit of majorana fermions in solid state systems. *Reports on Progress in Physics* **75**, 076501 (2012). URL https://dx.doi.org/10.1088/0034-4885/75/7/076501.

[186] Song, Q. *et al.* Evidence for a single-layer van der waals multiferroic. *Nature* **602**, 601–605 (2022). URL https://doi.org/10.1038/s41586-021-04337-x.

[187] Stewart, G. R. Heavy-fermion systems. *Rev. Mod. Phys.* **56**, 755–787 (1984). URL https://link.aps.org/doi/10.1103/RevModPhys.56.755.

[188] Yazdani, A. *et al.* Spectroscopic imaging of strongly correlated electronic states. *Annu. Rev. Condens. Matter Phys.* **7**, 11–33 (2016). URL https://doi.org/10.1146/annurev-conmatphys-031214-014529.

[189] Dzero, M. *et al.* Topological Kondo insulators. *Annu. Rev. Condens. Matter Phys.* **7**, 249–280 (2016). URL https://doi.org/10.1146/annurev-conmatphys-031214-014749.

[190] Wirth, S. *et al.* Exploring heavy fermions from macroscopic to microscopic length scales. *Nat. Rev. Mater.* **1**, 16051 (2016). URL https://doi.org/10.1038/natrevmats.2016.51.

[191] Pfleiderer, C. *et al.* Partial order in the non-Fermi-liquid phase of MnSi. *Nature* **427**, 227–231 (2004). URL https://doi.org/10.1038/nature02232.

[192] Stewart, G. R. Non-Fermi-liquid behavior in d- and f-electron metals. *Rev. Mod. Phys.* **73**, 797–855 (2001). URL https://link.aps.org/doi/10.1103/RevModPhys.73.797.

[193] Löhneysen, H. v. *et al.* Fermi-liquid instabilities at magnetic quantum phase transitions. *Rev. Mod. Phys.* **79**, 1015–1075 (2007). URL https://link.aps.org/doi/10.1103/RevModPhys.79.1015.

[194] Gegenwart, P. *et al.* Quantum criticality in heavy-fermion metals. *Nat. Phys.* **4**, 186–197 (2008). URL https://doi.org/10.1038/nphys892.

[195] Aynajian, P. *et al.* Visualizing heavy fermions emerging in a quantum critical Kondo lattice. *Nature* **486**, 201–206 (2012). URL https://doi.org/10.1038/nature11204.

[196] Ramires, A. *et al.* Emulating heavy fermions in twisted trilayer graphene. *Phys. Rev. Lett.* **127**, 026401 (2021). URL https://link.aps.org/doi/10.1103/PhysRevLett.127.026401.

[197] Coleman, P. Heavy fermions and the kondo lattice: a 21st century perspective (2015). URL https://arxiv.org/abs/1509.05769.

[198] Fumega, A. O. *et al.* Microscopic origin of multiferroic order in monolayer nii2. *2D Materials* **9**, 025010 (2022). URL https://dx.doi.org/10.1088/2053-1583/ac4e9d.

[199] Sandratskii, L. M. Symmetry analysis of electronic states for crystals with spiral magnetic order. i. general properties. *Journal of Physics: Condensed Matter* **3**, 8565–8585 (1991). URL https://doi.org/10.1088/0953-8984/3/44/004.

[200] Braunecker, B. *et al.* Spin-selective peierls transition in interacting one-dimensional conductors with spin-orbit interaction. *Physical Review B* **82** (2010). URL https://doi.org/10.1103/physrevb.82.045127.

[201] Dean, C. R. *et al.* Boron nitride substrates for high-quality graphene electronics. *Nature Nanotechnology* **5**, 722–726 (2010). URL https://doi.org/10.1038/nnano.2010.172.

[202] Wallbank, J. R. *et al.* Moiré superlattice effects in graphene/boron-nitride van der waals heterostructures. *Annalen der Physik* **527**, 359–376 (2015). URL https://doi.org/10.1002/andp.201400204.

[203] Island, J. O. *et al.* Spin–orbit-driven band inversion in bilayer graphene by the van der waals proximity effect. *Nature* **571**, 85–89 (2019). URL https://doi.org/10.1038/s41586-019-1304-2.

[204] Wang, D. *et al.* Quantum hall effect measurement of spin–orbit coupling strengths in ultraclean bilayer graphene/WSe2 heterostructures. *Nano Letters* **19**, 7028–7034 (2019). URL https://doi.org/10.1021/acs.nanolett.9b02445.

[205] Klein, D. R. *et al.* Probing magnetism in 2d van der waals crystalline insulators via electron tunneling. *Science* **360**, 1218–1222 (2018). URL https://doi.org/10.1126/science.aar3617.

[206] Kim, K. *et al.* van der waals heterostructures with high accuracy rotational alignment. *Nano Letters* **16**, 1989–1995 (2016). URL https://doi.org/10.1021/acs.nanolett.5b05263.

[207] Ribeiro-Palau, R. *et al.* Twistable electronics with dynamically rotatable heterostructures. *Science* **361**, 690–693 (2018). URL https://doi.org/10.1126/science.aat6981.

[208] Fischer, M. H. *et al.* Superconductivity without inversion and time-reversal symmetries. *Phys. Rev. Lett.* **121**, 157003 (2018). URL https://link.aps.org/doi/10.1103/PhysRevLett.121.157003.

[209] Chen, J. *et al.* Matrix product study of spin fractionalization in the 1d kondo insulator (2023). URL https://arxiv.org/abs/2302.09701.

[210] Coleman, P. New approach to the mixed-valence problem. *Phys. Rev. B* **29**, 3035–3044 (1984). URL https://link.aps.org/doi/10.1103/PhysRevB.29.3035.

[211] Read, N. *et al.* Stability of the kondo lattice in the large-n limit. *Phys. Rev. B* **30**, 3841–3844 (1984). URL https://link.aps.org/doi/10.1103/PhysRevB.30.3841.

[212] Auerbach, A. *et al.* Kondo bosons and the kondo lattice: Microscopic basis for the heavy fermi liquid. *Phys. Rev. Lett.* **57**, 877–880 (1986). URL https://link.aps.org/doi/10.1103/PhysRevLett.57.877.

[213] Millis, A. J. *et al.* Large-orbital-degeneracy expansion for the lattice anderson model. *Phys. Rev. B* **35**, 3394–3414 (1987). URL https://link.aps.org/doi/10.1103/PhysRevB.35.3394.

[214] de la Barrera, S. C. *et al.* Tuning Ising superconductivity with layer and spin–orbit coupling in two-dimensional transition-metal dichalcogenides. *Nature Communications* **9** (2018). URL https://doi.org/10.1038/s41467-018-03888-4.

[215] Fano, U. Effects of configuration interaction on intensities and phase shifts. *Phys. Rev.* **124**, 1866–1878 (1961). URL https://link.aps.org/doi/10.1103/PhysRev.124.1866.

[216] Hyart, T. *et al.* Non-hermitian many-body topological excitations in interacting quantum dots. *Phys. Rev. Research* **4**, L012006 (2022). URL https://link.aps.org/doi/10.1103/PhysRevResearch.4.L012006.

[217] Terada, Y. *et al.* Real-space imaging of transient carrier dynamics by nanoscale pump–probe microscopy. *Nature Photonics* **4**, 869–874 (2010). URL https://doi.org/10.1038/nphoton.2010.235.

[218] Cocker, T. L. *et al.* Tracking the ultrafast motion of a single molecule by femtosecond orbital imaging. *Nature* **539**, 263–267 (2016). URL https://doi.org/10.1038/nature19816.

[219] Garg, M. *et al.* Real-space subfemtosecond imaging of quantum electronic coherences in molecules. *Nature Photonics* **16**, 196–202 (2021). URL https://doi.org/10.1038/s41566-021-00929-1.

[220] Veldman, L. M. *et al.* Free coherent evolution of a coupled atomic spin system initialized by electron scattering. *Science* **372**, 964–968 (2021). URL https://www.science.org/doi/abs/10.1126/science.abg8223. https://www.science.org/doi/pdf/10.1126/science.abg8223.

[221] Diehl, S. *et al.* Quantum states and phases in driven open quantum systems with cold atoms. *Nature Physics* **4**, 878–883 (2008). URL https://doi.org/10.1038/nphys1073.

[222] Kraus, B. *et al.* Preparation of entangled states by quantum markov processes. *Phys. Rev. A* **78**, 042307 (2008). URL https://link.aps.org/doi/10.1103/PhysRevA.78.042307.

[223] Preskill, J. Lecture notes for ph219/cs219: Quantum information chapter 3 (2018). URL http://theory.caltech.edu/~preskill/ph219/chap3_15.pdf.

[224] Breuer, H. *et al.* *The Theory of Open Quantum Systems* (Oxford University Press, 2002). URL https://books.google.fi/books?id=0Yx5VzaMYm8C.

[225] Lindblad, G. On the generators of quantum dynamical semigroups. *Communications in Mathematical Physics* **48**, 119–130 (1976). URL https://doi.org/10.1007/bf01608499.

[226] Gorini, V. *et al.* Completely positive dynamical semigroups of n-level systems. *Journal of Mathematical Physics* **17**, 821–825 (1976). URL https://aip.scitation.org/doi/abs/10.1063/1.522979. https://aip.scitation.org/doi/pdf/10.1063/1.522979.

[227] Li, Y. *et al.* Quantum zeno effect and the many-body entanglement transition. *Phys. Rev. B* **98**, 205136 (2018). URL https://link.aps.org/doi/10.1103/PhysRevB.98.205136.

[228] Naghiloo, M. *et al.* Quantum state tomography across the exceptional point in a single dissipative qubit. *Nature Physics* **15**, 1232–1236 (2019). URL https://doi.org/10.1038/s41567-019-0652-z.

[229] Skinner, B. *et al.* Measurement-induced phase transitions in the dynamics of entanglement. *Phys. Rev. X* **9**, 031009 (2019). URL https://link.aps.org/doi/10.1103/PhysRevX.9.031009.

[230] Bender, C. M. *et al.* Real spectra in non-hermitian hamiltonians having pt symmetry. *Phys. Rev. Lett.* **80**, 5243–5246 (1998). URL https://link.aps.org/doi/10.1103/PhysRevLett.80.5243.

[231] Bender, C. M. Making sense of non-hermitian hamiltonians. *Reports on Progress in Physics* **70**, 947–1018 (2007). URL https://doi.org/10.1088/0034-4885/70/6/r03.

[232] El-Ganainy, R. *et al.* Non-hermitian physics and pt symmetry. *Nature Physics* **14**, 11 (2018). URL https://www.nature.com/articles/nphys4323.

[233] Kawabata, K. *et al.* Symmetry and topology in non-hermitian physics. *Phys. Rev. X* **9**, 041015 (2019). URL https://link.aps.org/doi/10.1103/PhysRevX.9.041015.

[234] Gong, Z. *et al.* Topological phases of non-hermitian systems. *Phys. Rev. X* **8**, 031079 (2018). URL https://link.aps.org/doi/10.1103/PhysRevX.8.031079.

[235] Bernard, D. *et al.* *A Classification of Non-Hermitian Random Matrices* (Springer Netherlands, 2002).

[236] Yao, S. *et al.* Edge states and topological invariants of non-hermitian systems. *Phys. Rev. Lett.* **121**, 086803 (2018). URL https://link.aps.org/doi/10.1103/PhysRevLett.121.086803.

[237] Yao, S. *et al.* Non-hermitian chern bands. *Phys. Rev. Lett.* **121**, 136802 (2018). URL https://link.aps.org/doi/10.1103/PhysRevLett.121.136802.

[238] Lee, T. E. Anomalous edge state in a non-hermitian lattice. *Phys. Rev. Lett.* **116**, 133903 (2016). URL https://link.aps.org/doi/10.1103/PhysRevLett.116.133903.

[239] Kunst, F. K. *et al.* Biorthogonal bulk-boundary correspondence in non-hermitian systems. *Phys. Rev. Lett.* **121**, 026808 (2018). URL https://link.aps.org/doi/10.1103/PhysRevLett.121.026808.

[240] Klitzing, K. v. *et al.* New method for high-accuracy determination of the fine-structure constant based on quantized hall resistance. *Phys. Rev. Lett.* **45**, 494–497 (1980). URL https://link.aps.org/doi/10.1103/PhysRevLett.45.494.

[241] Thouless, D. J. *et al.* Quantized hall conductance in a two-dimensional periodic potential. *Phys. Rev. Lett.* **49**, 405–408 (1982). URL https://link.aps.org/doi/10.1103/PhysRevLett.49.405.

[242] Chiu, C.-K. *et al.* Classification of topological quantum matter with symmetries. *Rev. Mod. Phys.* **88**, 035005 (2016). URL https://link.aps.org/doi/10.1103/RevModPhys.88.035005.

[243] Haldane, F. D. M. Model for a quantum hall effect without landau levels: Condensed-matter realization of the "parity anomaly". *Phys. Rev. Lett.* **61**, 2015–2018 (1988). URL https://link.aps.org/doi/10.1103/PhysRevLett.61.2015.

[244] Kane, C. L. *et al.* Quantum spin Hall effect in graphene. *Phys. Rev. Lett.* **95**, 226801 (2005). URL https://link.aps.org/doi/10.1103/PhysRevLett.95.226801.

[245] Bernevig, B. A. *et al.* Quantum spin hall effect. *Phys. Rev. Lett.* **96**, 106802 (2006). URL https://link.aps.org/doi/10.1103/PhysRevLett.96.106802.

[246] Kane, C. L. *et al.* Z_2 topological order and the quantum spin hall effect. *Phys. Rev. Lett.* **95**, 146802 (2005). URL https://link.aps.org/doi/10.1103/PhysRevLett.95.146802.

[247] Wang, Z. *et al.* Topological order parameters for interacting topological insulators. *Phys. Rev. Lett.* **105**, 256803 (2010). URL https://link.aps.org/doi/10.1103/PhysRevLett.105.256803.

[248] Chen, K.-T. *et al.* Unified formalism for calculating polarization, magnetization, and more in a periodic insulator. *Phys. Rev. B* **84**, 205137 (2011). URL https://link.aps.org/doi/10.1103/PhysRevB.84.205137.

[249] Lado, J. L. *et al.* Topological spin excitations in harper-heisenberg spin chains. *Phys. Rev. Research* **1**, 033009 (2019). URL https://link.aps.org/doi/10.1103/PhysRevResearch.1.033009.

[250] Zhou, H. *et al.* Periodic table for topological bands with non-hermitian symmetries. *Phys. Rev. B* **99**, 235112 (2019). URL https://link.aps.org/doi/10.1103/PhysRevB.99.235112.

[251] Lee, C. H. *et al.* Anatomy of skin modes and topology in non-hermitian systems. *Phys. Rev. B* **99**, 201103 (2019). URL https://link.aps.org/doi/10.1103/PhysRevB.99.201103.

[252] Yokomizo, K. *et al.* Non-bloch band theory of non-hermitian systems. *Phys. Rev. Lett.* **123**, 066404 (2019). URL https://link.aps.org/doi/10.1103/PhysRevLett.123.066404.

[253] Okuma, N. *et al.* Topological origin of non-hermitian skin effects. *Phys. Rev. Lett.* **124**, 086801 (2020). URL https://link.aps.org/doi/10.1103/PhysRevLett.124.086801.

[254] Zhang, K. *et al.* Correspondence between winding numbers and skin modes in non-hermitian systems. *Phys. Rev. Lett.* **125**, 126402 (2020). URL https://link.aps.org/doi/10.1103/PhysRevLett.125.126402.

[255] Takata, K. *et al.* Photonic topological insulating phase induced solely by gain and loss. *Phys. Rev. Lett.* **121**, 213902 (2018). URL https://link.aps.org/doi/10.1103/PhysRevLett.121.213902.

[256] Brzezicki, W. *et al.* Hidden chern number in one-dimensional non-hermitian chiral-symmetric systems. *Phys. Rev. B* **100**, 161105 (2019). URL https://link.aps.org/doi/10.1103/PhysRevB.100.161105.

[257] Kawabata, K. *et al.* Symmetry and topology in non-hermitian physics. *Phys. Rev. X* **9**, 041015 (2019). URL https://link.aps.org/doi/10.1103/PhysRevX.9.041015.

[258] Chen, G. *et al.* Topological spin excitations in non-hermitian spin chains with a generalized kernel polynomial algorithm. *Phys. Rev. Lett.* **130**, 100401 (2023). URL https://link.aps.org/doi/10.1103/PhysRevLett.130.100401.

[259] Hatano, N. *et al.* Localization transitions in non-hermitian quantum mechanics. *Phys. Rev. Lett.* **77**, 570–573 (1996). URL https://link.aps.org/doi/10.1103/PhysRevLett.77.570.

[260] Stewart, G. W. A krylov–schur algorithm for large eigenproblems. *SIAM Journal on Matrix Analysis and Applications* **23**, 601–614 (2002). URL https://doi.org/10.1137/S0895479800371529.

[261] Shibata, N. *et al.* Dissipative spin chain as a non-hermitian kitaev ladder. *Phys. Rev. B* **99**, 174303 (2019). URL https://link.aps.org/doi/10.1103/PhysRevB.99.174303.

[262] Jacob, D. *et al.* Orbital selective and tunable kondo effect of magnetic adatoms on graphene: Correlated electronic structure calculations. *Phys. Rev. B* **82**, 085423 (2010). URL https://link.aps.org/doi/10.1103/PhysRevB.82.085423.

[263] Lado, J. L. *et al.* Unconventional yu–shiba–rusinov states in hydrogenated graphene. *2D Materials* **3**, 025001 (2016).

[264] Weiße, A. *et al.* The kernel polynomial method. *Rev. Mod. Phys.* **78**, 275–306 (2006). URL https://link.aps.org/doi/10.1103/RevModPhys.78.275.

[265] Hatano, N. *et al.* Chebyshev-polynomial expansion of the localization length of hermitian and non-hermitian random chains. *Phys. Rev. E* **94**, 063305 (2016). URL https://link.aps.org/doi/10.1103/PhysRevE.94.063305.

[266] Feinberg, J. *et al.* Non-hermitian random matrix theory: Method of hermitian reduction. *Nuclear Physics B* **504**, 579–608 (1997). URL https://www.sciencedirect.com/science/article/pii/S0550321397005026.

[267] Dawson, H. G. On the numerical value of $\int_0^h \exp(x^2)dx$. *Proceedings of the London Mathematical Society* **s1-29**, 519–522 (1897). URL https://londmathsoc.onlinelibrary.wiley.com/doi/abs/10.1112/plms/s1-29.1.519.

[268] Belsley, D. *et al. Regression Diagnostics: Identifying Influential Data and Sources of Collinearity*. Wiley Series in Probability and Statistics (Wiley, 2005).

[269] Herviou, L. *et al.* Defining a bulk-edge correspondence for non-hermitian hamiltonians via singular-value decomposition. *Phys. Rev. A* **99**, 052118 (2019). URL https://link.aps.org/doi/10.1103/PhysRevA.99.052118.

[270] Okuma, N. *et al.* Hermitian zero modes protected by nonnormality: Application of pseudospectra. *Phys. Rev. B* **102**, 014203 (2020). URL https://link.aps.org/doi/10.1103/PhysRevB.102.014203.

Aalto-DT 84/2023

ISBN 978-952-64-1298-6 (printed)
ISBN 978-952-64-1299-3 (pdf)
ISSN 1799-4934 (printed)
ISSN 1799-4942 (pdf)

Aalto University
School of Science
Department of Applied Physics
www.aalto.fi

BUSINESS + ECONOMY

ART + DESIGN + ARCHITECTURE

SCIENCE + TECHNOLOGY

CROSSOVER

DOCTORAL THESES